Investigation of Spintronic Materials Systems:
Deposition and Characterization

Thesis by

Neal C. Oldham

In Partial Fulfillment of the Requirements

for the Degree of

Doctor of Philosophy

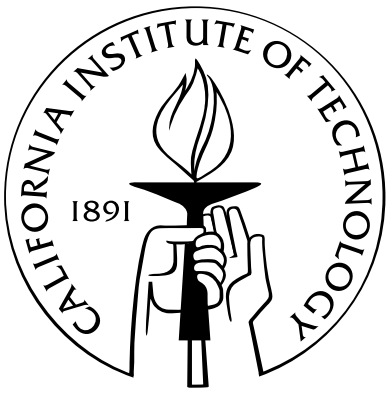

California Institute of Technology

Pasadena, California

2004

(Submitted May 27, 2004)

Acknowledgements

All I can hope to do here is give some small fraction of the appreciation due those who have helped carry this burden down the path for five years. I would first like to thank Tom McGill for being the ringleader of this circus, assembling under one tent a group whose like I can only hope in vain to work with again. He provided the means and environment to make this work happen and gave much more than he asked.

Thanks to all the members of the SSDP group. Tim Harris kept the locomotive on track and gave moral support at times when it was sorely needed. Gerry Picus provided a lot of encouragement and was a great voice of reason. Bob Beach was one of the first to welcome me and is one of the best guys you can have to help you get started (or keep going). Xavier Cartoixà Solar cheerfully rode herd on us as only the sole theorist in a group of wrenchmonkeys can and showed us the power of multiple windows. Rob Strittmatter was very helpful on both the growth and device sides, and I hate to imagine the lab without him. Justin Brooke, postdoc extraordinaire, brought creativity and enthusiasm to the group and was the catalyst for much of this work. You are missed. Stephan Ichiriu, Master of Optics and Computers and Much Else, has been a great peer and a great help. I wish you the best in your future career. Cory Hill, worked closely and tirelessly with me from the beginning until now and his skill and importance in completing this work cannot be overestimated. He was helpful and dedicated above and beyond any obligation of mere employment. Ed Preisler's energy, discipline, patience, spirit, and willingness to try new things were invaluable. I learned more than I can say from them. May the 49ers win five (more) Super Bowls.

I would like to thank our collaborators in no particular order: Darryl Smith, Jenna

Zinck, Joel Schulman, David Ting, Andy Hunter, and David Chow. You provided many good ideas, demonstrated some excellent science, and were a joy to associate with. Thanks to Mike Longerbone for all of the UHV help and making venting a learning experience. My appreciation also goes to Lake Shore Cryotronics and Brad Dodrill in particular for their help and collaboration. Of the dozens of vendors I had to contend with during the completion of this work, you win the "Best Vendor" award, hands down.

I would like to thank Carol Garland for putting up with me so many times. I would also like to thank her for being a great talent and a fantastic role model.

Many thanks to my dear friends at Caltech. Meg, Micol, Charlene, Matt, Geoff, Tim, and Ted more than made this place bearable. You've made it a fantastic place to be. Thanks also to the friends from Martin and UTK who've kept in touch. (You know who you are.)

I am thankful beyond words to my mother and father for being themselves and making sacrifice after sacrifice so I could go further in life. Thanks also to my uncle and aunt for their vast support as well. Now maybe y'all can finally retire.

Finally I would like to thank my future wife for her love and devotion through some very difficult times and over great distances. Ushma, I am looking forward to being together soon for a very long time to come.

Abstract

Continuing initiatives to deploy radical new computing schemes impel the study of new materials systems appropriate for realization of these schemes. One contemporary idea for a basis for new computing architectures is spintronics, the manipulation of electron or nuclear spin for the construction of physical quantum logic and other devices. In this work basic materials development for spintronics will be discussed. The growth and characterization of materials systems proposed as means of injecting spin-polarized electron populations into nonmagnetic semiconductors is examined. Specific materials systems analyzed include magnetite (Fe_3O_4), cobalt-chromium alloys, and gallia (Ga_2O_3). Deposition of these materials in thin film form with a suite of techniques including pulsed laser deposition (PLD) and electron-beam evaporation (EBE) is analyzed. Particular attention is given to the chemistry and magnetic properties of these films. Magnetic thin films of magnetite are observed upon silicon, gallium arsenide, and magnesium oxide; the epitaxy of magnetite upon indium arsenide is addressed. Additionally out-of-plane magnetization of Co-Cr alloys is demonstrated and several metallurgical issues with their deposition are discussed. Finally aspects of EBE deposition of gallia for ultrathin tunnel barriers are discussed.

Contents

List of Figures

List of Tables

Chapter 1

Introduction

1.1 Thesis Overview

The following work details an investigation into several materials systems with a focus on their applicability for solid-state electronic devices exploiting electron spin. It primarily addresses materials growth and properties such as chemistry, crystal structure, and magnetization, but also describes electrical and optical characterization. Materials systems examined include epitaxial films of magnetite (Fe_3O_4), alloys of cobalt and chromium (Co-Cr) for perpendicularly magnetizing thin films, and gallium oxide (Ga_2O_3 amorphous ultrathin films.

1.2 Limitations of Existing Solid-State Electronic Technology

The invention of the point-contact transistor in 1947 by J. Bardeen and W.H. Brattain [1] initiated the era of solid-state electronics. With the introduction of the metal-oxide-semiconductor field-effect transistor (MOSFET) in the 1960s [2], electronic devices grew exponentially in technological and economic importance. The famous prediction by Intel co-founder Gordon Moore that transistors would double in density every eighteen months entered popular culture as "Moore's Law" and held true for decades beyond Moore's original vision.

It is important to understand several aspects of FET devices for this discussion. The ubiquity of the FET is a direct result of its ability to switch current on and off with small applied voltages. Figure 1.1 illustrates a common class of MOSFET, the normally off enhancement-mode MOSFET.

The main components are the source, gate, and drain terminals. The substrate or back bias is usually a ground or reference voltage in most academic treatments, though it can be exploited in some applications [3]. The source is also usually grounded [4]. Bias, V_{DS}, is applied to the drain such that current flows between the source and drain, denoted by I_{DS}. I_{DS} is also a function of the bias on the gate (V_{GS}). Once V_{GS} reaches the threshold voltage (V_T), the region between the source and drain will invert. The basic equation of MOSFET operation is

$$I_{DS} = \begin{cases} \frac{W_{\text{eff}}\mu_{\text{eff}}C_{ox}}{L_{\text{eff}}}(V_{GS} - V_T - \frac{1}{2}V_{DS})V_{DS} & V_{GS} \geq V_T \\ I_{D1}(\exp\frac{q(V_{GS}-V_T)}{nk_BT})(1 - \exp\frac{-qV_{DS}}{k_BT}) & V_{GS} < V_T \end{cases} \tag{1.1}$$

where L_{eff} is the effective channel length, μ_{eff} is the effective mobility of majority carriers in the channel, W_{eff} denotes the effective device width, C_{ox} signifies the capacitance of the oxide film itself, and I_{D1} is a proportionality constant with the dimension of current. n is given by

$$n = 1 + \frac{C_b + C_{it}}{C_{ox}} \tag{1.2}$$

where C_b is the bulk capacitance of the substrate and C_{it} is the capacitance of the interfacial trap states between the oxide layer and the channel [5]. (All capacitances in this discussion are normalized by device area.)

Miniaturizing the MOSFET device has been key to improving performance from digital microelectronics. Not only does higher density allow more logic operations per unit area, but shorter gate lengths also allow carriers to spend less time in the channel, *i.e.*, operate faster. Scaling of devices to smaller lithographically defined sizes unfortunately introduces numerous technical and scientific challenges as a result of several undesirable phenomena which manifest. These include the onset of short-

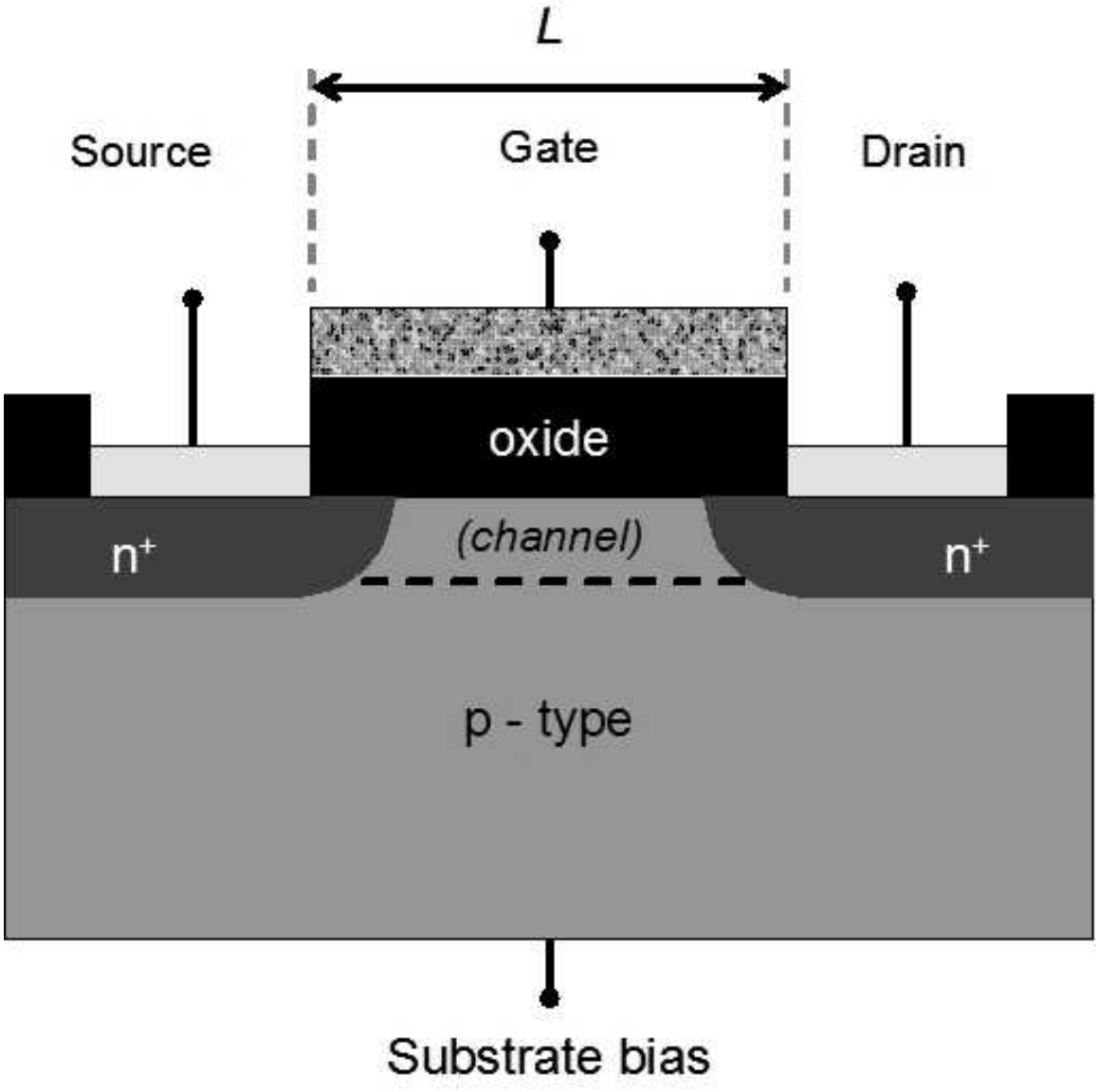

Figure 1.1: A schematic illustration of an enhancement-mode (normally off) n-channel MOSFET.

channel effects such as a failure of the $I_{DS} - V_{DS}$ curve to saturate, significant I_{DS} at $V_{GS} = 0$, and a dependence of I_{DS} upon V_{DS} in the subthreshold region.

One condition for long-channel behavior for an enhancement-mode MOSFET is that the device must not be fully depleted at $V_{GS} = 0$ ("off" condition). If the depletion depths on the source and drain sides of the channel meet, then the device will not turn off. The minimum length to maintain long-channel subthreshold behavior for a given device was measured by Brews *et al.* in a seminal paper [6] and at $V_{DS} = 0$ they found

$$L_{min} \propto (x_j t_{ox} W_D)^{1/3} \tag{1.3}$$

x_j is the junction depth (*i.e.*, the depth of the n-type regions of the source and drain), t_{ox} signifies the gate oxide thickness, and W_D is the depletion depth into the channel associated with the drain. The size of the latter decreases as the acceptor concentration N_A increases. The necessary doping level scales linearly as the lithographic channel length decreases [7, 8].

Another effect of the increased doping level in the substrate is that the bulk charge increases, which without an accompanying increase in C_{ox} will result in higher electric fields for operation and thus higher power requirements.

A rigorous examination of the effect on V_T of three-dimensional scaling of the channel is given by DeMassa and Chien [9] who demonstrated that while a decrease in channel width *increases* V_T, a decrease in channel length decreases it. However, scaling of channel length has decreased to the point that decreasing V_T is unavoidable. Figure 10 of Ref. [9] demonstrates the rapid drop in V_T at small channel length.

The oxide capacitance also plays a major role in another important performance parameter, the subthreshold swing S, which determines the gate voltage excursion to go from an "off" to an "on" state [8]. The subthreshold swing is defined as

$$S = \frac{2.303 n k_B T}{q}, \tag{1.4}$$

where k_B is Boltzmann's constant, T signifies temperature, and q is the charge on

one electron.

The standard approach to increasing C_{ox} has been to thin the oxide, since $C_{ox} = \epsilon_{ox}/t_{ox}$, ϵ_{ox} being the permittivity of the oxide. The permittivity is usually expressed as $\kappa = \epsilon_{ox}/\epsilon_0$, where ϵ_0 is the permittivity of vacuum. SiO_2 ($\kappa = 3.9$) has been the insulator of choice for commercial Si-based FETs because of the ease of processing and the excellent electrical properties of the Si/SiO_2 interface. To achieve the target of 45-nm feature sizes by 2010 [10] the use of new gate materials will be unavoidable. The gate dielectric simply must be made thicker again in order to reduce leakage currents. An overview of the selection of alternative gate dielectrics is given by Schlom and Haeni. Based on thermochemical stability in contact with silicon at real processing conditions, only a handful of oxides may be useful. The leading candidates appear to be ZrO_2 and HfO_2, for which $\kappa \sim 23$ [11].

1.3 Electron Spin-Manipulating Devices for Novel Logic and Memory Applications

Novel approaches to overcome the aforementioned difficulties associated with scaling in the dominant MOSFET technology have proliferated in recent decades. Spin manipulation for memory storage has attracted much interest, as have sensitive magnetic field detectors. Concurrently, interest in the experimental implementation of quantum computing proliferated.

1.3.1 Origin of Solid-State Spin Manipulation Devices

The origin of spin-manipulating electronic devices lies in the discovery in 1970 by Meservey and Tedrow of spin-polarized tunneling in a superconductor/insulator/superconductor structure by observing spin polarization in the tunneling conductance as a function of applied bias in various applied magnetic fields [12]. Jullière performed similar work using a ferromagnet (FM)/insulator (I)/FM structure and showed that the conduction

electrons in ferromagnetic metals are partly spin-polarized and that tunneling across the insulator preserves this polarization [13]. Jullière derived that the junction magnetoresistance (JMR) is

$$\text{JMR} = \frac{R_A - R_P}{R_A} = \frac{\Delta R}{R} = \frac{2P_1P_2}{1 + P_1P_2} \tag{1.5}$$

where R_A is the junction resistance when the two ferromagnets' moments are antiparallel, R_P when the two ferromagnets' moments are parallel, and P_1 and P_2 are the spin polarizations of the two ferromagnets. The polarization is defined as

$$P = \frac{n_\uparrow - n_\downarrow}{n_\uparrow + n_\downarrow} \tag{1.6}$$

where $n_\uparrow$ and $n_\downarrow$ represent the spin-up and spin-down electron density, respectively.

Technological implementations of spin-polarized tunneling for logic and memory devices were devised in the years following this work of Meservey, Tedrow, Jullière, and others. One of the most basic ideas is the concept of the spin valve, which consists of a soft ferromagnetic layer, a conductive paramagnet spacer, and a hard magnetic layer whose magnetization vector $\vec{M}_{\text{hard}}$ is pinned in place by coupling to an antiferromagnetic layer [14]. The magnetization of the soft layer $\vec{M}_{\text{soft}}$ is switched either deliberately or by ambient effect. When current flows from the soft layer to the paramagnet, it flows mostly from one spin orientation's subband. (This is contrast to the FM/I/FM structure mentioned earlier where the transport is due to quantum mechanical tunneling.) The relative orientation of $\vec{M}_{\text{hard}}$ and $\vec{M}_{\text{soft}}$ determines if the spin polarization effect on current is additive or subtractive and thus creates the magnetoresistance difference between parallel and antiparallel states. This type of device is usually used commercially to exploit this giant magnetoresistance effect for magnetic field sensing.

Sophisticated ideas for exploiting magnetoresistance effects include magnetic random-access memory (MRAM) and the bipolar spin switch. O'Handley actually credits the first conception of MRAM to Schwee in the early 1970s [14, 15] but the concept gained little notoriety until after a series of refinements following the discov-

ery of giant magnetoresistance (GMR) in 1988 [16]. Figure 1.2a shows a cartoon of an MRAM element. At its core is a structure very similar to the spin valve described above. The "word" line orients the soft layer by means of the electromagnetic field that results from a pulse of current through the line. The resistance of the stack is measured through the "sense" line. The resistance for the parallel and antiparallel configurations is known and correlates to "0" and "1" bit values. Contemporary commercial MRAM prototypes use a TMR scheme where the spacer is a thin ($\sim$ 13 Å) layer of an oxide, usually alumina. Because MRAM is by nature a nonvolatile memory, commercial interest is considerable. Areal density as well as bit isolation and other issues have delayed deployment of MRAM, however.

Another landmark device was the bipolar spin switch developed by Johnson. Fig. 1.2b illustrates the device schematically. Current flows through the base ferromagnet layer F1 and the paramagnetic layer (in Johnson's scheme, Au) when a switch is closed. A so-called "spin bottleneck" effect occurs in the paramagnet. The spin of the current enhances the spin polarization in layer F2, and the net effect is a voltage gain. The remarkable aspect of this result was that gain was inversely proportional to device size [17]. However the device has no power gain as shown; also, all interfaces are ohmic and the bias differences measured are small [18].

The most influential proposal was that of Datta and Das [19]. Instead of the metal and superconductor junctions which had been to date the focus of the device community, they chose a semiconductor substrate for their *gedanken* device, which is shown in Fig. 1.2c. The device was intended to modulate the spin of current in the two-dimensional electron gas (2DEG) [20] between two ferromagnetic contacts in a manner analogous to a material which, upon application of an electrical bias, manipulates the phase of light passing between a polarizer and analzyer (the electro-optic effect). The change in spin would be controlled by a gate in the same manner as a FET. The practicality of the scheme is dependent upon a difference in energy between spin states in the 2DEG. This difference arises from the Rashba spin-orbit coupling term in the Hamiltonian which becomes nonzero due to the application of the electrical field from the gate perpendicular to current flow [21]:

$$\hat{\mathcal{H}}_{\text{Rashba}} = i\alpha\mathcal{E}_y(\hat{\sigma}_z\frac{\partial}{\partial x} - \hat{\sigma}_x\frac{\partial}{\partial z}) \tag{1.7}$$

$\hat{\sigma}_{z,x}$ are the Pauli spin matrices, $\mathcal{E}_y$ represents the scalar perpendicular electric field, and α is the Rashba coefficient signifying the strength of this spin-orbit coupling. Subsequently theoretical and experimental obstacles have caused the implementation of the Datta-Das spin transistor scheme to elude workers to the present. Nonetheless, this concept gave rise to concentrated efforts in electron spin-based semiconductor device research and provided the impetus for the work presented in this document.

Recently experiments have been performed in which nuclear spins were manipulated as well as electron spins. These will be discussed below.

1.3.2 Quantum Computing

The idea of quantum computing owes its existence to several famous papers [22, 23, 24] which established the concept of entanglement, the ability to establish nonlocal correlations between two classically uncorrelated states. The applications are very powerful. Shor announced his algorithm for factorization and the discrete logarithm problem using quantum mechanics in 1994 in a landmark work [25] and, in 1997, Grover published his algorithm for database searching which reduced the number of reads from the classical result of $N/2$ to $\sqrt{N}$ [26]. The former had great promise for the field of cryptanalysis, and quantum computational solutions which are exponentially more efficient than those implemented on a classical computer were proposed for other problems as well [27]. All rely upon constructing a "qubit," an "element with a two-dimensional Hilbert space, capable of existing in a superposition of Boolean states and of being entangled with the states of other qubits" [28]. Quantum logic operations, like classical ones, are performed with constructs labeled gates. The operations of gates are represented as unitary operators ($\hat{U}^\dagger = \hat{U}^{-1}$).

Deutsch demonstrated that the Toffoli three-qubit gate was an adequate universal gate (*i.e.*, capable of implementing all unitary operations on arbitrary numbers of bits) for the building of quantum computational networks [29]. (Some two-qubit

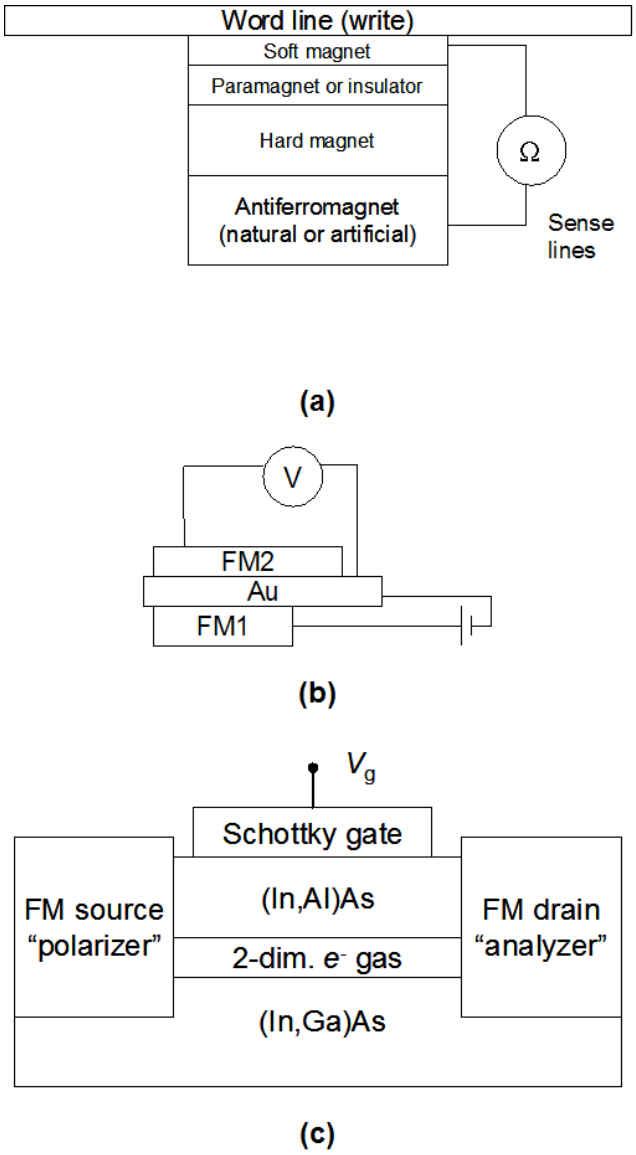

Figure 1.2: Some schemes for practical spin devices. (a) Generalized schematic of MRAM memory element. (b) Bipolar spin-valve device for voltage gain. From [17]. (c) Datta-Das transistor showing some elements of the electro-optic modular analogy. From [19].

universal gates exist but are not thermodynamically or logically reversible [28].) The problem of decoherence was addressed by Shor [30] among others. This theoretical work built a framework in which the goal of building quantum computers seemed practical, compelling workers to search for ways to physically implement them.

Physical implementation of qubits has proven more elusive than theoretical frameworlks. Many schemes have been advanced. Perhaps the most outstanding of the results to date remains Chuang *et al.*'s use of nuclear spins in radiolabeled chloroform as qubits with nuclear magnetic resonance (NMR) used to read and write information [31]. Unfortunately this method has dubious scalability to larger numbers of qubits.

One technique which was shown to be viable for the storage of one qubit was a high-Q resonance cavity using the quantum electrodynamics of a single two-level atom [32]. ($Q \equiv \Delta f/f$, where f is the resonant frequency of the cavity and Δf is the FWHM of the resonant frequency peak.) The availability of high-Q cavities limits the practicality of this technique though recent advances [33] may allow it to evolve. Another concept that has been explored is using trapped ions as qubits. In this scheme lasers or electric fields confine ions in nanofabricated solid-state wells [34]. Scaling and decoherence remain technical difficulties with this technique.

The approach to spin-based computing which has impelled the experimental work in this thesis is that of *spintronics*, an umbrella term for spin manipulation in solid-state devices. DiVincenzo and Loss proposed quantum gates consisting of neighboring quantum dots with unpaired electron spins. These are controlled by biasing tunnel barriers between the dots. Entanglement occurs due to the Hesienberg exchange between the spins when the electrostatic potential between the dots is low. Other dots serve as spin valves or positive-operator-valued paramagnets for reading the qubit [35]. This concept continues to be refined [36] and may serve as a basis for solid-state qubits. Quantum wire structures are also proposed which can read spins as single classical bits [37]. These are fabricated inside a nanoporous alumina film and are sensitive enough to see single spins at liquid nitrogen temperatures, although they are not truly reading superpositions of "up" and "down" quantum states.

Many of these proposals rely upon technologies which are relatively new. It is hoped to implement quantum computing with semiconductor FET structures similar to the Datta-Das transistor in order to build upon mature technologies such as photolithography. The ability to build qubits with FET-like devices should accelerate deployment of semiconductor spin electronics. These proposals are usually described as "spin transistors." Structures suggestive of the complementary MOS (CMOS) inverter are envisioned where the terminals of the devices are connected, allowing the construction of a quantum gate where each transistor behaves as a qubit and quantum states from different transistors entangle. Other concepts trap an electron under the gate and perform quantum logic operations on its spin; these are referred to as "spin resonance transistors" [38].

To implement this structure three obstacles must be overcome. The first is the injection of spin from the spin source into the channel such that the current in the device is spin-polarized. The second is extending the short lifetime of polarization in the channel. The last is the detection and measurement of spin at the spin drain. Some advances have been made but many more challenges must be addressed before this technology may be demonstrated.

1.4 Practical Obstacles to Spintronic Semiconductor Device Deployment

This section focuses on the theoretical and experimental barriers to semiconductor spintronics. Fourteen years after the debut of the Datta-Das transistor concept the field remains very dynamic.

1.4.1 Spin Injection into Semiconductor Materials

Spin injection, as discussed here, is defined as the translation of the magnetic spin polariziation of an energy input into a *segregation* of carrier populations by spin orientation inside the semiconductor material. Typically the source is a ferromagnet

deposited on the semiconductor, but alternate approaches and modifications exist. Inducing a material which is naturally a diamagnet to demonstrate magnetic behavior is no trivial task and the experimental and theoretical histories contain many abortive efforts.

Workers have devised means of utilizing the Rashba effect (Eq. 1.7) to perform spin polarization without magnetic fields. Electric field manipulation is used to create spin-polarized populations in the InAs/GaSb/AlSb materials system [39, 40, 41]. While these devices hold considerable promise, significant challenges in processing and measurement remain to be addressed. Our work focuses upon injection from a magnet into a semiconductor, however, and this will be the thrust of the following discussion.

The first attempt to demonstrate spin injection in a FM/semiconductor (SC) structure was Monzon and Roukes's measurement in the Ni-Fe/InAs/Ni-Fe system. They deduced that local Hall effects made it very difficult to perform traditional magnetoresistance measurements [42]. The magnetoresistance of their structures vanished for certain geometries. This was attributed to the possibility that the injection was ballistic (*i.e.*, involving electrons with considerably more energy than the conduction band edge) [43].

Attempts followed to model the population dynamics of polarization in semiconductors. Schmidt *et al.* considered the problem from a diffusion approach, phrasing spin-polarization of the conduction electrons in the semiconductor in terms of the electrochemical potentials $\mu_{\uparrow,\downarrow}$ of the semiconductor spin populations in a FM/SC/FM structure and the series resistance of the system. Their model predicted that

$$\frac{R_A - R_P}{R_P} = \frac{P^2}{P^2 - 1} \tag{1.8}$$

where P is the polarization of the FM layer [44] and R_A, R_P are defined in Eq. 1.5. The difference in conductivity between the ferromagnet and semiconductor was predicted to have a large impact on spin injection. Thus in the case of direct injection from a ferromagnetic metal into a semiconductor the polarization (Eq. 1.6) must be

nearly 100%. The polarization of metallic ferromagnets is typically $< 60\%$. Some permendurs (*e.g*, $Co_{84}Fe_{16}$) have a spin polarization of 55% [13] but these are among the highest in commonly used metallic alloys.

Experimentally new schemes evolved to detect spin injection in light of the challenges with magnetoresistance measurements. The most successful of these was the conversion of polarized current into circularly polarized electroluminescence with a quantum well, since it is known that the polarization of the luminescence depends upon which valence subbands are involved in recombination [45]. Practically speaking the emitted light is elliptically polarized and the circular polarization is extracted via the Stokes formalism to measure the polarization of the current. While optical detection is limited to direct-gap semiconductors, such as III-V compounds, it provided insight into the nature of the FM/SC contact. Fiederling *et al.* overcame the issue of conductivity mismatch by using a dilute magnetic semiconductor ($Be_xMg_yZn_{1-x-y}Se$) in lieu of a metallic ferromagnet. This was epitaxially grown upon an n-$Al_xGa_{1-x}As$/GaAs/p-$Al_xGa_{1-x}As$ quantum well, used as the spin detection structure. An applied magnetic field was applied to create Zeeman splitting in the II-Se structure and enhance spin alignment. The spin polarization was 90% at liquid helium temperatures [46].

Another significant optical detection experiment was performed by Hanbicki *et al.* [47]. This used the structure shown in Fig. 1.3. Elemental Fe was used as the ferromagnetic contact. In place of a foreign insulating material the tunneling barrier was formed by very heavily doping the semiconductor in a very thin region ("δ-doping") with donors such that a triangular barrier was formed. The spin injection efficiency was 30% at room temperature.

The importance of such tunnel barriers was theoretically predicted by Smith and Silver [48] and Rashba [49]. Smith and Silver, using a diffusive model similar to that of Ref. [44], predicted that if some form of tunneling barrier with spin-dependent conductivity was present between the FM and SC layers, the polarization of the current in the semiconductor would be enhanced. Spin-dependent conductance can arise because the tunnel barrier is itself magnetic or because the senses of the Fermi

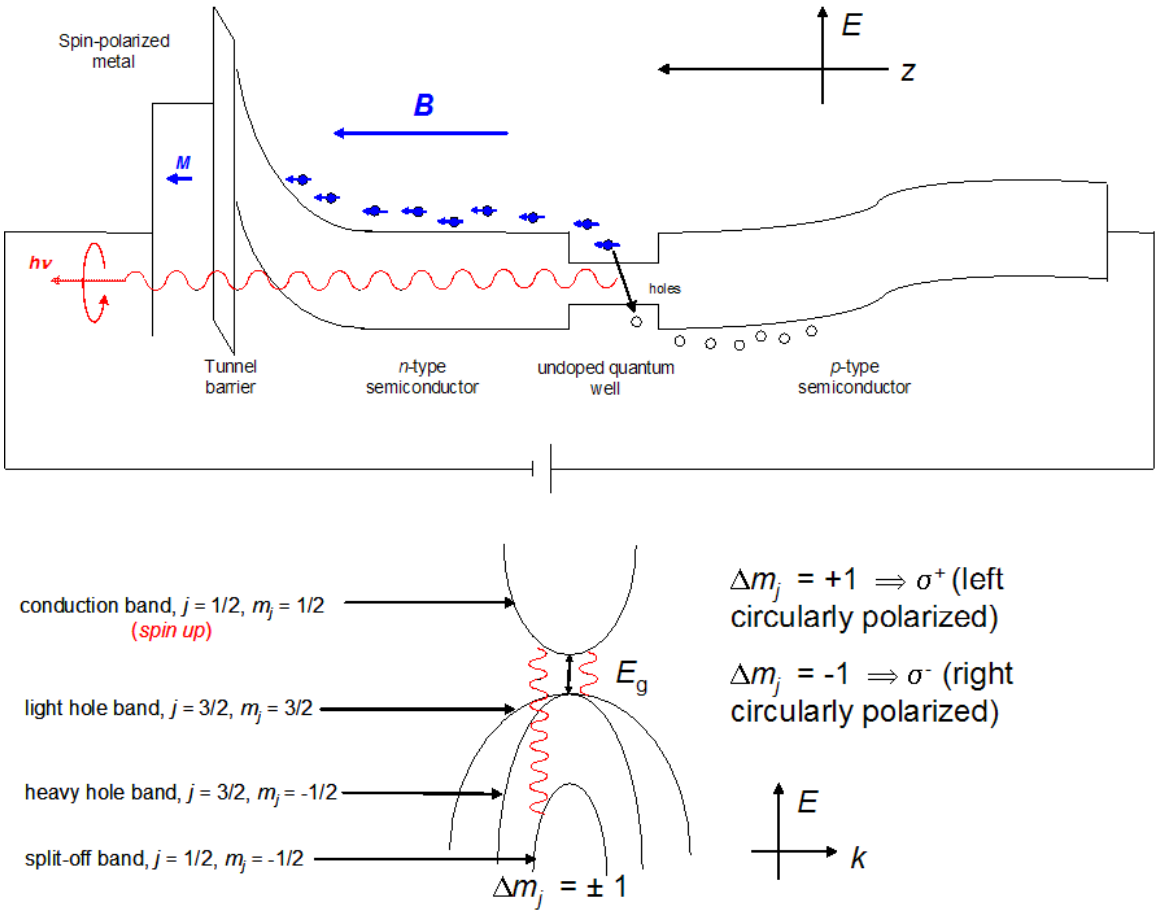

Figure 1.3: Schematic of optical detection of spin injection in FM/SC structures. *Top:* Band structure of quantum well spin injector. The growth direction is denoted by z. Reverse bias and an external magnetic field are applied. The tunnel barrier allows efficient spin injection. *Bottom:* Energy band diagram showing radiative recombination processes in quantum well when conduction electrons are spin-polarized. Quantum selection rules allow only transitions for which $\Delta m_j = \pm 1$.

wavevectors for the spin-up and spin-down states from the FM contact are different. The latter is owed to the asymmetry of the density of spin-up and spin-down states in a ferromagnet, causing a difference in the transmission coefficient and thus the effective conductivity.

Specifically, Smith and Silver's diffusive model predicts

$$\alpha_{\mathrm{SC}} = \frac{(R_{\mathrm{FM}}G_{\downarrow} + \frac{1}{\alpha_{\mathrm{FM}}})\alpha_{\mathrm{FM}}}{(R_{\mathrm{FM}}G_{\downarrow} + \frac{G_{\downarrow}}{G_{\uparrow}} + 1)} + \left(\frac{G_{\downarrow}}{R_{\mathrm{FM}}G_{\downarrow} + \frac{G_{\downarrow}}{G_{\uparrow}} + 1} + \frac{1}{R_{\mathrm{SC}}}\right)\frac{\mu_{\uparrow} - \mu_{\downarrow}}{qj} \tag{1.9}$$

where, for component i, $\alpha_i = (P_i + 1)/2$, j is the total current density, $\mu_{\uparrow,\downarrow}$ is the electrochemical potential of the appropriate spin type inside the semiconductor and has units of energy, $G_{\uparrow,\downarrow}$ is the conductivity of electrons of the associated spin at the interface and has units of conductance per unit length, and R_i is given by

$$R_i = \frac{L_i}{\sigma_i \alpha_i (1 - \alpha_i)} \tag{1.10}$$

σ_i being the bulk conductivity of component i, and L_i is the spin diffusion length in i. Note that since α_{SC} is contained in both the lhs and rhs of Eq. 1.9 that this must be solved numerically.

One prediction of this model is that as the interface resistance $1/(G_{\uparrow} + G_{\downarrow})$ increases, the spin polarization in the semiconductor increases also. Figure 2 of Ref. [48] shows that an increase in interface resistance of two orders of magnitude results in an improvement in P_{SC} by an order of magnitude or more. This is directly related to the improvement associated with spin-dependent tunneling.

Similar results are given by the Rashba model, refined by Jonker in terms of an effective resistor model [50] with two parallel FM/I/SC series: One spin-up and the other spin-down. The implications are the same; spin injection from a ferromagnet with intrinsic polarization less than 100% into a semiconductor practically requires a tunnel layer. Motsnyi *et al.* demonstrated $P_{\mathrm{SC}} = 9\%$ at 80 K with an aluminum oxide tunnel barier instead of a δ-doped layer [51].

A contrasting result is the demonstration of spin injection in Fe/p-InAs Schottky diode structures. If the iron is epitaxial and the interface is pristine, Zwierzycki *et al.* calculate from the band structures and symmetries of Fe and InAs that this arrangement should behave as a spin filter with P_{SC} between 98 and 99% [52]. They also claim that this result should be valid for other zincblende III-V compound semiconductors such as (Al,Ga)As. There exists experimental support for this approach. Yoh *et al.* claimed a maximum spin injection of 40% from epitaxial Fe(001) into p-InAs(001) at $T = 6.5$ K in an applied field of over 80 kOe [53]. However, this work makes several unverified assumptions regarding the spin polarization of unsaturated magnets as well as spin lifetimes at cryogenic temperatures. Zhu *et al.* demonstrated spin injection efficiency of 2% for Fe/GaAs at room temperature without a tunnel barrier [54].

Conductivity mismatch may be overcome by using a spin-polarizing contact with a conductivity closer to that of the semiconductor. An obvious candidate for such a contact is another semiconductor, namely a magnetic one. The most commonly used magnetic semiconductor for spin injection is (Ga,Mn)As [55, 56, 57] but others have been tested such as (Ga,Mn)N [58]. To date, demonstrations of spin injection with these materials have resulted in relatively low efficiencies ($< 10\%$) and then only at cryogenic temperatures. Another feature which may impact spin injection is polarization of *nuclear* spins. Polarized electron spin currents can interact with nuclear spins *via* the hyperfine interaction [59]. Strand *et al.*, using a strucutre similar to that of Fig. 1.3, observed a twentyfold enhancement of spin polarization above that predicted by their purely electronic model, and calculated that this was the result of dynamic nuclear polarization [60].

1.4.2 Spin Lifetime and Detection

It is clearly inadequate to merely inject spin into a material. As previously stated, the spin population must remain polarized during its transit of the device channel and a means must exist to measure that spin in order to construct spin devices.

Spin lifetimes (and thus diffusion lengths) are relatively short in III-V compound semiconductors due to numerous spin decoherence mechanisms. These include the Elliott-Yafet effect, by which conventional carrier scattering processes such as ionized-impurity and electron-phonon scattering interact with the spin-orbit coupling to cause spin flip. The photon emitted by electron-hole recombination can create another pair of spin orientation opposite from that of the original pair. This is known as the Bir-Aronov-Pikus effect. Also, in structures such as zincblende without inversion symmetry, the D'yakonov-Perel' (DP) mechanism causes spin precession (wobbling) and shortens spin lifetimes [61]. Using pump-probe photoluminescence techniques and sub-picosecond oscillators, Hall *et al.* measured longitudinal spin resonance lifetimes T_1 of 700 fs and 18 ps for InAs/GaSb (001) and (110) superlattices, respectively, at $T = 115$ K [62]. In GaAs the spin lifetime is 100 ns at 5 K and ∼0.1 ns at 300 K; for GaN at 300 K, the lifetime is ∼100 ns [63]. For silicon the spin lifetime is conservatively 10 μs [38].

Detection of spin remains an active research area. The difficulty of injecting spin and local Hall effects complicate measurements and several attempts have been made to overcome it. Electroluminescence techniques have limited utility, except perhaps in the telecommunications industry [38]. The junction magnetoresistance method, using FM/SC/FM structures, may be used, but the semiconductor thickness w_{SC} must be shorter than the spin diffusion length. Using the terminology developed above, Fert and Jaffrès [64] give this condition as

$$\frac{L_{\mathrm{SC}}}{\sigma_{\mathrm{SC}}} \ll \frac{G_\uparrow + G_\downarrow}{4 G_\uparrow G_\downarrow} \ll \frac{L_{\mathrm{SC}}^2}{\sigma_{\mathrm{SC}} w_{\mathrm{SC}}} \tag{1.11}$$

where w_{SC} is the thickness of the semiconductor layer. Additionally, the magnetoresistance structures refuted by Monzon *et al.* were defended by the original authors [65] and experiments continue measuring the spin current in 2DEG structures [66].

1.5 Summary of Results

Because the unifying theme of this thesis is the exploration of materials with potential utility for injection of spin currents into semiconductors, the work is separated into chapters on the basis of materials systems. Chapter 2 examines the structure and properties of magnetite (Fe_3O_4) thin films deposited by pulsed laser deposition. Magnetization of polycrystalline magnetite grown on silicon, gallium arsenide, and magnesium oxide is demonstrated and compared to similar work in the literature. Epitaxy of Fe_3O_4 on InAs is shown by reflection high energy electron diffraction and the surprising failure of these films to retain a permanent magnetic moment is examined in light of property predictions from the literature. Chapter 3 explores application of perpendicular magnetic anisotropy to spintronics but mainly focuses on the physical metallurgy of three different methods of depositing Co-Cr alloy films. Finally, Chapter 4 details the deposition and chemical properties of ultrathin GaO_x films for tunnel barriers.

Bibliography

[1] J. Bardeen and W. Brattain, Phys. Rev. **74**, 230 (1948).

[2] S. Sze, *Physics of Semiconductor Devices*, 2nd ed. (Wiley-Interscience, New York, 1981).

[3] D. K. Schroder, in *The Encyclopedia of Materials: Science and Technology*, edited by K. H. J. Buschow, R. W. Cahn, M. C. Flemings, B. Ilschner, E. J. Kramer, and S. Mahajan (Elsevier Science, Berlin, 2001).

[4] R. Pierret, *Semiconductor Device Fundamentals* (Addison-Wesley Publishing Company, Reading, MA, 1996), p. 612.

[5] D. Schroder, *Semiconductor Material and Device Characterization*, 2nd ed. (Wiley-Interscience, New York, 1998), p. 387.

[6] J. R. Brews, W. Fichtner, E. H. Nicollian, and S. M. Sze, IEEE Electr. Device L. **1**, 2 (1980).

[7] D. J. Frank, R. H. Dennard, E. Nowak, P. M. Solomon, Y. Taur, and H. S. P. Wong, Proc. IEEE **89**, 259 (2001).

[8] R. H. Dennard, F. H. Gaensslen, H.-N. Yu, V. L. Rideout, E. Bassous, and A. R. LeBlanc, IEEE J. Solid-St Circ. **9**, 256 (1974).

[9] T. A. DeMassa and H. S. Chien, Solid State Electron. **29**, 409 (1986).

[10] International Technology Roadmap for Semiconductors 2002 Update, http://public.itrs.net/Files/2002Update/2002Update.pdf, May 8, 2004.

[11] D. G. Sclom and J. H. Haeni, MRS Bull. **27**, 198 (2002).

[12] R. Meservey, P. M. Tedrow, and P. Fulde, Phys. Rev. Lett. **25**, 1270 (1970).

[13] J. S. Moodera, J. Nassar, and G. Mathon, Annu. Rev. Mater. Res. **29**, 381 (1999).

[14] R. C. O'Handley, *Modern Magnetic Materials: Principles and Applications*, 1st ed. (Wiley-Interscience, New York, 2000).

[15] L. J. Schwee, IEEE T. Magn. **8**, 405 (1972).

[16] M. N. Baibich, J. M. Broto, A. Fert, F. N. Vandau, F. Petroff, P. Etienne, G. Creuzet, A. Friederich, and J. Chazelas, Phys. Rev. Lett. **61**, 2472 (1988).

[17] M. Johnson, Science **260**, 320 (1993).

[18] J. F. Gregg, in *Spin Electronics*, edited by M. Ziese and M. J. Thornton (Springer-Verlag, Berlin, 2001), p. 15.

[19] S. Datta and B. Das, Appl. Phys. Lett. **56**, 665 (1990).

[20] E. F. Schubert, *Doping in III-V Semiconductors*, 1st ed. (Cambridge University Press, Cambridge, 1993), pp. 392–394.

[21] L. W. Molenkamp, G. Schmidt, and G. E. W. Bauer, Phys. Rev. B **64**, 121202 (2001).

[22] A. Einstein, B. Podolsky, and N. Rosen, Phys. Rev. **47**, 777 (1935).

[23] D. Bohm, Phys. Rev. **85**, 166 (1952).

[24] J. S. Bell, Rev. Mod. Phys. **38**, 447 (1966).

[25] P. W. Shor, in *Proceedings of the 35th Annual Symposium on Foundations of Computer Science*, edited by S. Goldwasser (IEEE Computer Society, Los Alamitos, Calif., 1994), p. 124.

[26] L. K. Grover, Phys. Rev. Lett. **79**, 325 (1997).

[27] J. P. Dowling and G. J. Milburn, Philos. T. Roy. Soc. A **361**, 1655 (2003).

[28] A. Barenco, C. H. Bennett, R. Cleve, D. P. DiVincenzo, N. Margolus, P. W. Shor, T. Sleator, J. A. Smolin, and H. Weinfurter, Phys. Rev. A **52**, 3457 (1995).

[29] D. Deutsch, Philos. T. Roy. Soc. A **425**, 73 (1989).

[30] P. W. Shor, Phys. Rev. A **52**, R2493 (1995).

[31] I. L. Chuang, L. M. K. Vandersypen, X. Zhou, D. W. Leung, and S. Lloyd, Nature **393**, 143 (1998).

[32] X. Maître, E. Hagley, G. Nogues, C. Wunderlich, P. Goy, M. Brune, J. M. Raimond, and S. Haroche, Phys. Rev. Lett **79**, 769 (1997).

[33] D. K. Armani, T. J. Kippenberg, S. M. Spillane, and K. J. Vahala, Nature **421**, 925 (2003).

[34] J. I. Cirac and P. Zoller, Nature **404**, 579 (2000).

[35] D. Loss and D. P. DiVincenzo, Phys. Rev. A **57**, 120 (1998).

[36] D. P. DiVincenzo, D. Bacon, J. Kempe, G. Burkard, and K. B. Whaley, Nature **408**, 339 (2000).

[37] S. Bandyopadhyay, Phys. Rev. B **67**, 193304 (2003).

[38] E. Yablonovitch, H. W. Jiang, H. Kosaka, H. D. Robinson, D. S. Rao, and T. Szkopek, P. IEEE **91**, 761 (2003).

[39] X. Cartoixà, D. Z. Y. Ting, E. S. Daniel, and T. C. McGill, Superlattice. Microst. **30**, 309 (2001).

[40] D. Z.-Y. Ting, X. Cartoixà, D. H. Chow, J. S. Moon, D. L. Smith, T. C. McGill, and J. N. Schulman, P. IEEE **91**, 741 (2003).

[41] K. C. Hall, W. H. Lau, K. Gündoğdu, M. E. Flatté, and T. F. Boggess, Appl. Phys. Lett. **83**, 2937 (2003).

[42] F. G. Monzon, H. X. Tang, and M. L. Roukes, Phys. Rev. Lett. **84**, 5022 (2000).

[43] F. G. Monzon and M. L. Roukes, J. Magn. Magn. Mater. **199**, 632 (1999).

[44] G. Schmidt, D. Ferrand, L. W. Molenkamp, A. T. Filip, and B. J. van Wees, Phys. Rev. B **62**, R4790 (2000).

[45] C. Weisbuch and B. Vinter, *Quantum Semiconductor Structures: Fundamentals and Applications* (Academic Press, Boston, 1991).

[46] R. Fiederling, M. Keim, G. Reuscher, W. Ossau, G. Schmidt, A. Waag, and L. W. Molenkamp, Nature **402**, 787 (1999).

[47] A. T. Hanbicki, B. T. Jonker, G. Itskos, G. Kioseoglou, and A. Petrou, Appl. Phys. Lett. **80**, 1240 (2002).

[48] D. L. Smith and R. N. Silver, Phys. Rev. B **64**, 045323 (2001).

[49] E. I. Rashba, Phys. Rev. B **62**, R16267 (2000).

[50] B. T. Jonker, S. C. Erwin, A. Petrou, and A. G. Petukhov, MRS Bull. **28**, 740 (2003).

[51] V. F. Motsnyi, J. De Boeck, J. Das, W. Van Roy, G. Borghs, E. Goovaerts, and V. I. Safarov, Appl. Phys. Lett. **81**, 265 (2002).

[52] M. Zwierzycki, K. Xia, P. J. Kelly, G. E. W. Bauer, and I. Turek, Phys. Status Solidi A **196**, 25 (2003).

[53] K. Yoh, H. Ohno, Y. Katano, K. Sueoka, K. Mukasa, and M. E. Ramsteiner, Semicond. Sci. Tech. **19**, S386 (2004).

[54] H. J. Zhu, M. Ramsteiner, H. Kostial, M. Wassermeier, H.-P. Schönherr, and K. H. Ploog, Phys. Rev. Lett. **87**, 016601 (2001).

[55] Y. Ohno, D. K. Young, B. Beschoten, F. Matsukura, H. Ohno, and D. D. Awschalom, Nature **402**, 790 (1999).

[56] M. Ramsteiner, H. Y. Hao, A. Kawaharazuka, H. J. Zhu, M. Kastner, R. Hey, L. Daweritz, H. T. Grahn, and K. H. Ploog, Phys. Rev. B **66**, 081304 (2002).

[57] N. Samarth, S. H. Chun, K. C. Ku, S. J. Potashnik, and P. Schiffer, Solid State Commun. **127**, 173 (2003).

[58] S. J. Pearton, C. R. Abernathy, G. T. Thaler, R. M. Frazier, D. P. Norton, F. Ren, Y. D. Park, J. M. Zavada, I. A. Buyanova, W. M. Chen, and A. F. Hebard, J. Phys.-Condensed Mat. **16**, R209 (2004).

[59] A. W. Overhauser, Phys. Rev. **92**, 411 (1953).

[60] J. Strand, B. D. Schultz, A. F. Isakovic, C. J. Palmstrøm, and P. A. Crowell, Phys. Rev. Lett. **91**, 036602 (2003).

[61] F. X. Bronold, A. Saxena, and D. L. Smith, arXiv:cond-mat/0402085, 3 Feb 2004.

[62] K. C. Hall, K. Gündoğdu, E. Altunkaya, W. H. Lau, M. E. Flatté, T. F. Boggess, J. J. Zinck, W. B. Barvosa-Carter, and S. L. Skeith, Phys. Rev. B **68**, 115311 (2003).

[63] S. Krishnamurthy, M. van Schilfgaarde, and N. Newman, Appl. Phys. Lett. **83**, 1761 (2003).

[64] A. Fert and H. Jaffrès, Phys. Rev. B **64**, 184420 (2001).

[65] P. R. Hammar, B. R. Bennett, M. J. Yang, and M. Johnson, Phys. Rev. Lett. **84**, 5024 (2000).

[66] R. H. Silsbee, J. Phys.-Condensed Mat. **16**, R179 (2004).

Chapter 2

Epitaxy and Characterization of Magnetite

2.1 Motivation

As was shown in Sec. 1.4.1, if electric spin injection is performed with a contact which is 100% spin polarized (*i.e.*, if every mobile electron in the contact material has the same electron spin orientation) then the injection should be nearly 100% efficient. Elemental ferromagnets and alloys of elemental ferromagnets such as permalloys and permendurs do not have 100% spin-polarized conduction electrons. The density of states of both spin types is sizeable at the Fermi surface.

In 1983, de Groot *et al.* predicted the existence of "half-metals" [1]. They predicted that the majority-spin electrons were metallic, whereas the minority-spin electrons should be semiconducting.

Since this prediction half-metals have been examined both experimentally and theoretically and a classification scheme has emerged. This is illustrated in Fig. 2.1. Elements such as Co and Fe cannot be half-metals, for example, because the Fermi level includes $4s$ electrons which obviously have no net spin [2].

Type I half-metals have only one spin type at the Fermi level. Examples are CrO_2 (I_A, < 5 d electrons) and Sr_2FeMoO_6 (I_B, > 5 d electrons). Their electrons at the Fermi level are itinerant. Type II half-metals find their Fermi level in a mostly unfilled band. The carriers at that level, which are all of one spin type, are localized.

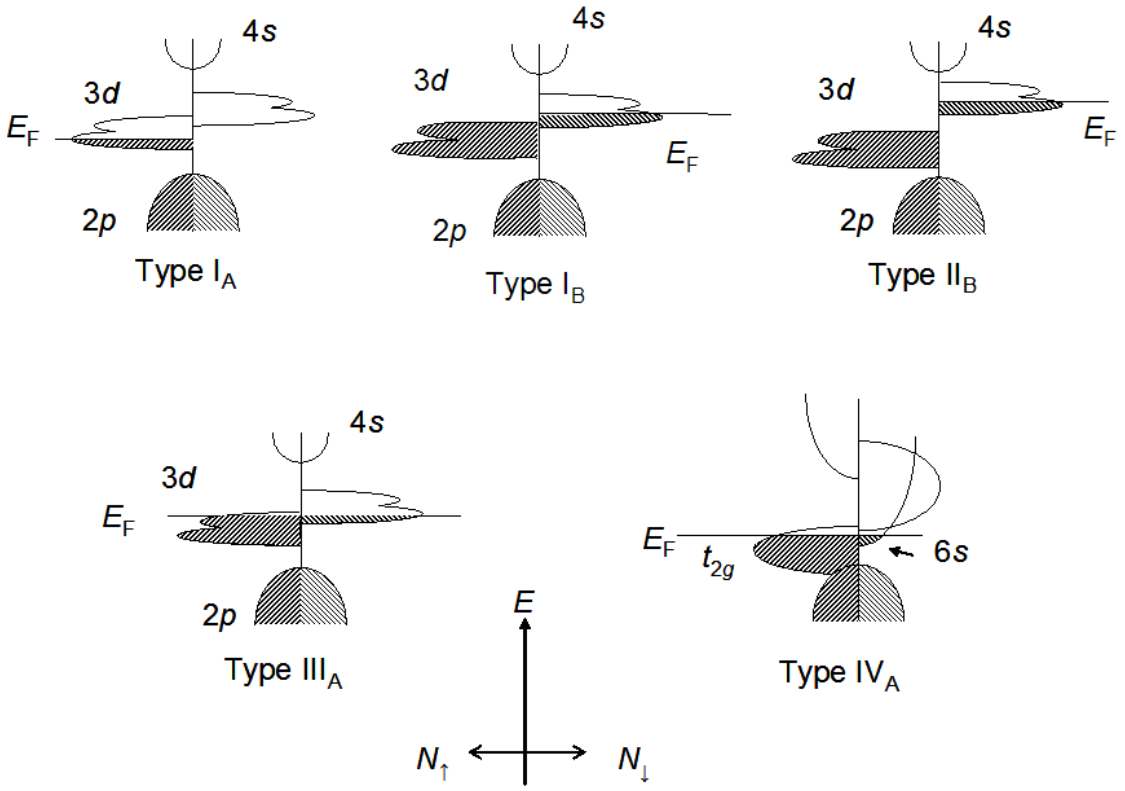

Figure 2.1: Half-metal classification scheme, after Coey *et al.* [2]. The 3*d* bands are split into e_g (higher energy) and t_{2g} states (lower energy) by the crystal field from the oxygen anions [3]. See text for description of various types.

This results in conduction by "hopping," a polaron-mediated mechanism by which carriers must be thermally excited to conduct at all. No carriers of the other spin type are near the Fermi level; a bandgap characterizes their relationship to the 4*s* conduction level. Fe_3O_4 belongs to this class.

Type III_A half-metals are materials such as $La_{0.7}Sr_{0.3}MnO_3$ where electrons of one spin type are metallically itinerant and those of the other spin type at the Fermi level are localized. Semimetals with magnetic ordering and a large effective mass difference between electrons and holes are classified as Type IV_A half-metals. An example of this class is $Tl_2Mn_2O_7$.

Experimental verification of half-metallicity is not straightforward. Techniques used to determine the spin polarization include photoemission experiments, magnetoresistance, point contact techniques, Tedrow-Mersevey superconducting tunnel

junctions, and Andreev point-contact reflection [4]. The best evidence for half-metallicity in any material was an Andreev reflection measurement of CrO_2 for which a polarization of 90% was observed [5]. In Andreev reflection, electrons from the normal material may join a Cooper pair in a contacting superconductor if they have the proper polarization. If they do, a hole is reflected back into the normal metal and this hole current reveals the spin polarization of the normal metal.

To construct spin-injection devices, half-metals are an obvious candidate for the polarizing contact. They generally have lower conductivities than elemental transmission metals and better spin polarization. Instead of CrO_2 as the half-metal of choice, however, it was decided to pursue the epitaxy of magnetite (Fe_3O_4). Epitaxy of this material on silicon and gallium arsenide was already known [6] and it was hoped that it could be grown on indium arsenide as well.

Magnetite has a Curie temperature of 860 K and has been known as a magnet since antiquity. It is the prototypical ferrimagnetic material and has an inverse spinel structure in which Fe atoms sit on two different sites. One of theses has an average oxidation of 2.5+ and a configuration of $(t_{2g}^3 e_g^2)^{\uparrow}(t_{2g}^0.5)^{\downarrow}$ (net moment $3.63\mu_B$) and the other having a 3+ oxidation state and a configuration of $(t_{2g}^3 e_g^2)^{\downarrow}$, net moment $-3.37\mu_B$ [2, 7]. The total magnetic moment of magnetite is $4.1\mu_B$/formula unit [8]. (A formula unit is a stoichiometric set of atoms in a compound. In this case, this would be three iron and four oxygen atoms.) It undergoes the Verwey transition at $T = 120$ K, below which it becomes a nonmagnetic insulator, meaning that Andreev measurement of spin polarization is practically impossible. Other measurements have been made to support the half-metallicity of Fe_3O_4, however. Dedkov *et al.* report a spin polarization of -80% [9] by photoemission experiments. (The negative value is because only minority spins populate the Fermi level.) The half-metallicity is critical since the resistivity at room temperature (10^{-3} Ω-cm) is too low to promote efficient spin-injection otherwise (see Fig. 8 of Ref. [10]).

2.2 Experimental Methods

2.2.1 Pulsed Laser Deposition

Growth of Fe_3O_4 has been achieved by numerous techniques in the literature . Although molecular beam epitaxy (MBE) is well established for epitaxy of oxide thin films including Fe_3O_4, pulsed laser deposition (PLD), also referred to as laser ablation, utilized existing facilities and expertise.

The technique of pulsed laser deposition was invented shortly after the demonstration of the ruby laser in the 1960s but only proliferated when it was shown to be particularly suited for fabrication of stoichiometric cuprate superconductors. In PLD a laser beam collides with a target; material thus ablated is deposited on the substrate. A discussion of the mechanisms of ablation is given by Kelly and Miotello [11]. The primary mechanisms are

- **Collisional sputtering** The ions in the ablation plasma are accelerated and sputter the target as a result.
- **Thermal sputtering** Boiling from the target.
- **Electronic sputtering** Sputtering from electronic phenomena such as Schottky defects.
- **Exfoliational sputtering** Explosive ejection of material resulting from thermal-stress fractures.
- **Hydrodynamic sputtering** Thermal expansion of droplets known as *asperities* breaks surface tension and expels liquid material from the target.

The rapid timescales of laser ablation make it very useful for the epitaxy of mixtures or compounds which do not decompose congruently, *e.g.*, oxide superconductors.

Figure 2.2 diagrams our PLD mechanism. Our laser is a Quantel BrilliantB solid-state Q-switched Nd:YAG system. Nd:YAG solid-state lasers are a mature technology and more compact than excimer lasers which are also popular for PLD. A series of

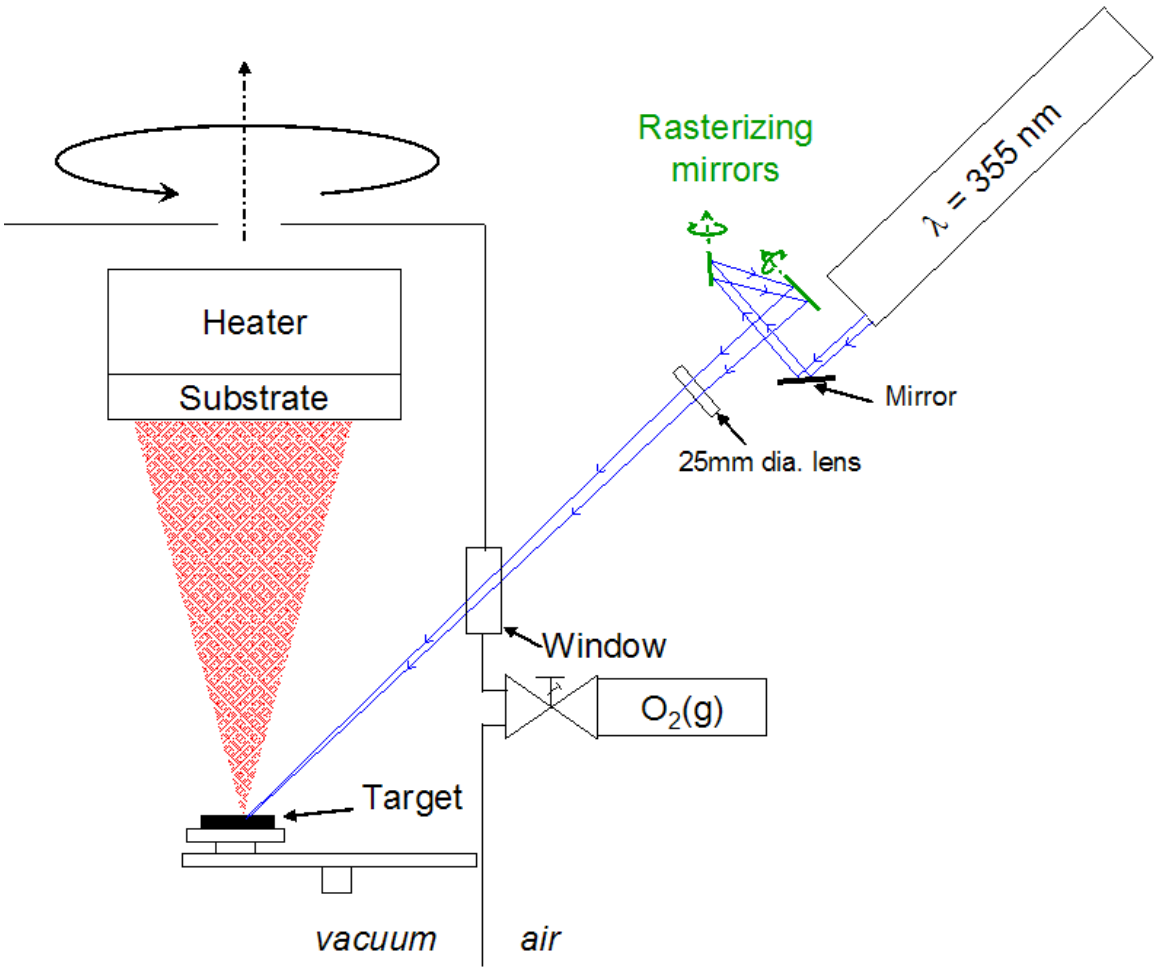

Figure 2.2: Schematic illustration of our pulsed laser deposition apparatus. See text for details.

nonlinear crystals propagates the third harmonic wavelength (355 nm) of the Nd:YAG line (fundamental wavelength of 1067 nm). The laser has a maximum energy output of 0.2 J and a maximum power of 2 W using the 355-nm harmonic. Pulse duration is $\sim$ 4 ns, and the laser was operated at a rate of ten pulses per second. Fluence at the target was unknown as measuring the spot size on the ultrahigh vacuum side was not feasible.

Substrate temperature was $T_{sub} = 350°C$ for all samples (see Sec. 2.2.2). All samples were rotated during growth to promote uniformity. Deposition rate was shown to be 0.3 Å/s (Sec. 2.3.1).

Shorter wavelength is desirable to reduce the problem of "splashing," the expulsion of large particulates onto the substrate due to subsurface boiling, recoil in the liquid phase, and the breaking of eroded solid structures. This is known to be an issue with the fundamental and second harmonics of the Nd:YAG laser [12]. Rastering the beam with two computer-controlled motorized mirrors oscillating randomly and at right angles minimizes the problem of splashing since this prevents the laser from ablating from one increasingly rough region of the target. The fourth harmonic at 267 nm was also available but this wavelength was found to dramatically reduce the lifetime of the components of the optical train.

Hematite (α-Fe_2O_3) ceramic targets were used. It was found after several depositions that this produced the desired stoichiometry (see Table 2.1) without input of O_2(g). Those samples for which O_2 was introduced are denoted whenever applicable. When it was used, it was bled into the chamber by means of a leak valve from a bottle at room temperature. The entire oxygen apparatus was evacuated by a turbomolecular pump and baked prior to use, and only ultrahigh purity O_2 was used in the system. Although plasma sources, neutral-atom sources, and ozone sources are often utilized in oxide epitaxy, these were not available. The oxygen pressure $P_{O_2} = 5 \times 10^{-6}$ torr when O_2(g) was introduced.

2.2.2 Substrate Preparation

Epitaxial InAs buffer layers were grown on (001)-oriented wafers in a Perkin-Elmer 430 molecular beam epitaxy (MBE) chamber. Ohring gives a basic overview of MBE [13]. Growth rates were maintained at 2 Å/s. During growth an excess of As_2 dimers was effused through a hot-filament cracker such that the growth rate was limited by the temperature of the In effusion cell. Substrate temperature was 450°C during growth. The material was p-doped using a Be effusion cell to a concentration of $N_A = 10^{18}$ cm^{-3}. The surface upon completion of MBE as determined by RHEED (see Sec. 2.3.3) was the (2×4) surface associated with As-rich growth. The substrate temperature was 350°C for all iron oxide films discussed in this chapter both because the InAs surface will decompose at temperatures above 400°C and, in order to compare growth across materials systems, it was desired to perform all growths at the same temperature.

Gallium arsenide was grown in a nearly identical manner, except that the substrate temperature in that case was higher (550-600°C). It also demonstrated the As-rich $c(4\times4)$ surface upon completion of growth. Magnesium oxide substrates were merely degreased before introduction to vacuum and were outgassed at 750°C before iron oxide growth. Silicon substrates, all having (111) orientation, were cleaned in a buffered HF etch to remove native oxides and introduced to vacuum. Epitaxial Si was grown by e-beam evaporation in the same chamber used for PLD. These were grown at a substrate temperature of 600°C until the (7×7) surface was evident by RHEED.

2.2.3 Post-deposition Processing

An iron oxide film deposited upon MgO in the presence of O_2(g) was annealed after removal from vacuum to determine if this could result in magnetization. It was annealed in a rapid thermal annealer at a temperature of 500°C in an argon atmosphere. This did not result in a magnetic film. No other post-deposition processing was performed.

2.3 Characterization

The iron oxide films prepared by PLD were analyzed by many different characterization techniques in order to ascertain their chemical and crystallographic properties as well as their magnetic moment, key to any future successful exploitation as a spintronic material system. Chemistry and crystal structure were probed by means of x-ray photoelectron spectroscopy (XPS) as well as reflection high-energy electron diffraction (RHEED). These techniques were natural choices for material characterization due to their availability in our ultrahigh vacuum (UHV) cluster. Determination of film thickness for calibration of growth rates was accomplished by x-ray reflectometry (XRR), an *ex situ* method. Finally, the magnetic properties of the iron oxide films were measured by magneto-optic Kerr effect (MOKE) polarimetry and by vibrating-sample magnetometry (VSM).

2.3.1 X-ray Reflectometry for Thin-Film Thickness Determination

The highly directional nature of PLD makes deposition rate monitoring by a quartz crystal monitor (QCM) extremely difficult if not impossible in most chamber configurations, including ours. Additionally, in cases where RHEED images are diffuse or growth proceeds in a three-dimensional regime, acquiring growth rate data by means of intensity oscillation measurement may also be impractical. Regardless, deposition rate determination is still a necessity for reproducible thin-film growth. To this end, XRR was used to determine thin-film thickness after growth in order to calibrate the deposition rate of PLD.

X-ray reflectometry uses the same components as x-ray diffractometry (XRD) but measures parameters such as thin-film thickness and interfacial roughness. X-ray reflectometry contrasts with XRD in that the latter measures phenomena associated with the interplanar spacing of a crystalline unit cell, whereas XRR is a "non-Bragg" process and examines interference patterns from an entire layer.

Two configurations are available for reflectivity measurement: *Specular*, where the

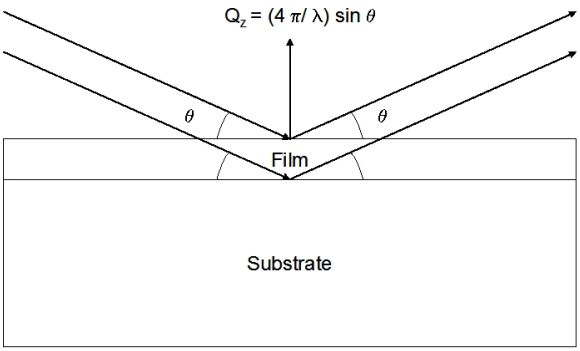

Figure 2.3: X-ray reflectometry. The reference angle $\omega = 0$ denotes perpendicular alignment of the sample normal and x-ray beam.

scan is referenced to the position at which the sample plane is parallel to the incident beam ($\omega = 0$ in the universally accepted notation for XRD), and *diffuse*, where the reference sample position denotes nonparallel alignment of the sample plane and beam ($\omega \neq 0$). Our system utilizes the specular arrangement, illustrated in Fig. 2.3.

X-ray reflectometry measurements require the ability to translate the sample into and out of the x-ray beam along the direction conventionally labeled the z axis, which in the case of studies of thin films deposited upon wafers is almost always the growth direction, *i.e.*, the normal to the wafer plane. This required modification of our system, a Philips Materials Research Diffractometer (MRD), as it was not equipped with z translation. A custom stage was constructed by Forvis Technologies of Santa Barbara, Calif., and mounted on our system.

Measurements require scanning the detector to find the forward intensity maximum $I = I_{max}$ of the beam. This position is denoted as $2\theta = 0$. The sample is then aligned with an iterative process. In the first step, the sample is translated into the beam until $I = I_{max}/2$. The sample angle ω is then scanned to find the intensity maximum, which becomes $\omega = 0$. Since at this position it is likely that $I \neq I_{max}/2$, the sample is translated again until $I = I_{max}/2$. ω is scanned again to find the maximum, and the whole process is repeated until the sample is exactly halfway into the beam and its normal is perpendicular to the beam propagation vector. The data scan is taken next. This is an $\omega/2\theta$ scan, an example of which is shown in Fig. 2.4. The first peak arises from the intersection of the beam with an increasing volume of the

sample; the second originates from refraction at the critical angle [14]. The peaks of interest are the periodic peaks at higher angles. Known as Kiessig fringes [15], these arise from the thin film on the sample surface. The intensity maxima occur where $\exp(-2ik_{0z}w) = 1$, where k_{0z} is the magnitude of the reflected wave vector in the z direction and w the layer thickness. The critical angle θ_c for external reflection is given by $\theta_c = \sin^{-1}\sqrt{2(1-n)}$, where n is the real part of the index of refraction of the deposited film and may be determined by inspection of a $\omega/2\theta$ reflectivity curve obtained as described above. In Fig. 2.4 this is seen to be $\theta_c \approx 0.25°$.

The maxima are found at

$$2\lambda = 2w\sqrt{\sin^2\theta_m - \sin^2\theta_c} \tag{2.1}$$

where λ is the x-ray wavelength, m is an integer, and θ_m is the angle at which the m^{th} Kiessig fringe occurs [16]. Using the approximation $\sin\theta \simeq \theta$ simple algebraic manipulation reveals

$$w \simeq \frac{\lambda}{2(\theta_{m+1} - \theta_m)} \tag{2.2}$$

2.3.2 X-ray Photoelectron Spectroscopy Analysis for Chemical State and Stoichiometry Determination

2.3.2.1 Historical Background and Instrument Description

X-ray photoelectron spectroscopy (XPS) is a very useful technique for the determination of the electronic structure of compounds. It was one of a family of techniques pioneered by Siegbahn *et al.* in the 1960s [17]. The umbrella term "electron spectroscopy for chemical analysis" (ESCA) came to refer specifically to XPS and the terms may be used interchangeably. The essence of the technique is that x-rays of a known energy are incident upon the sample of interest. Photoexcited electrons exit the sample and are detected and measured. X-ray photoelectron spectroscopy is one of the best techniques for measuring the chemistry of thin layers as it returns

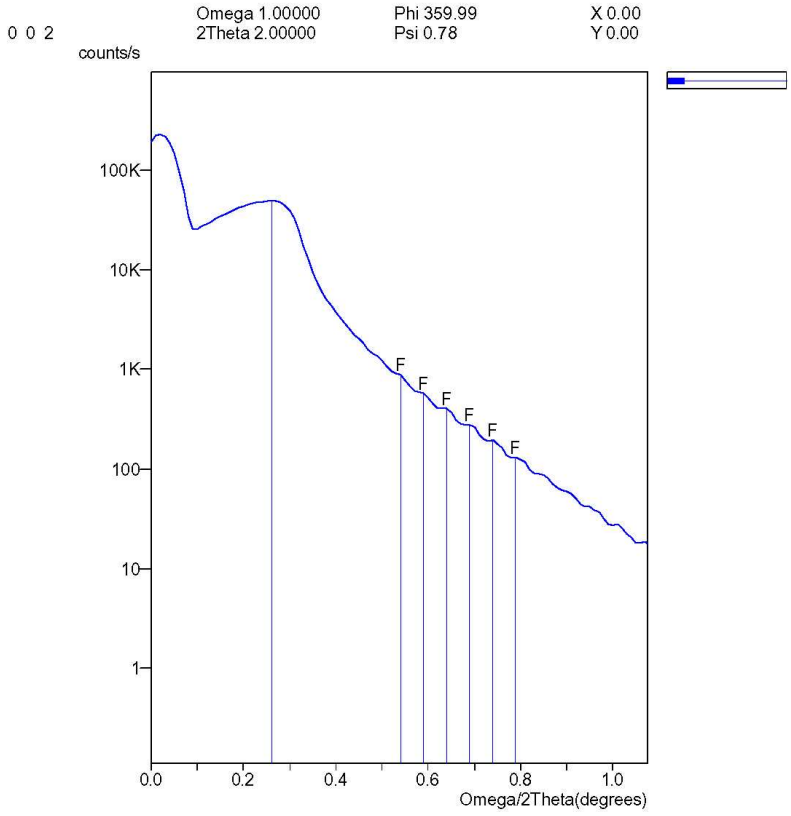

Scan: 916XRR.D01
Date: 4/26/2004
Interpretation: Superlattice Period

Mean Omega fringe period (°): 0.04995
Superlattice period (um): 0.0884 ± 0.0005

Omega/2Theta (°)	Omega Fringe Period (°)	Thickness (um)
0.54000 - 0.59002	0.05002	0.088231
0.59002 - 0.64009	0.05006	0.088164
0.64009 - 0.68955	0.04946	0.089231
0.68955 - 0.73972	0.05017	0.087976
0.73972 - 0.78973	0.05000	0.088270

Figure 2.4: X-ray reflectivity scan of Fe_3O_4/GaAs. The layer thickness of the iron oxide film is seen to be $\sim$ 884 Å. Analysis performed using Philips X'PERT 3.0 software.

information from only the topmost 100 Å of the sample or less. (The exact number depends on the signal intensity and surface chemistry.)

There is considerable diversity in x-ray source technology. Synchrotron facilities exist for XPS that emit x-rays with energies on the order of 100 keV. Such arrangements are impractical for on-campus university research unfortunately, and so conventional x-ray tubes with elemental targets are used. Electrons escape from a filament (the cathode) via thermionic emission and are focused by the anode onto the target. This stimulates the emission of x-rays from the target. All the characteristic wavelengths except the Kα emission are filtered by a metal window with an appropriate frequency cutoff; the Kα photons serve as the x-ray source for XPS.

This work used a PHI Model 5800 XPS system, which is connected by an ultrahigh vacuum (UHV) transfer system to each of the deposition systems discussed in this work and thus measures the "clean" as-grown surfaces of our thin films. The basic layout of the instrument is shown in Fig. 2.5. Measurements may be made with one of two sources. The Mg source produces x-rays with $E = 1486.6$ eV and a linewidth of 0.8 eV. The Al source produces 1253.6 ± 0.7 eV photons, but also mounts a monochromator which reduces the linewidth of this source to 0.3 eV. The monochromator consists of a quartz crystal with a radius of curvature of 500 mm and is positioned to minimize the linewidth of the Al Kα x-ray source.

The detector system consists of an Omni Focus III electron lens which collects the photoelectrons from the sample, a Perkin-Elmer Model 10-360 hemispherical analyzer consisting of two curved charged plates which serve to segregate the photoelectrons by energy. The kinetic energy of the emitted photoelectron is

$$T_{sp} = h\nu - E_B - \phi_s \tag{2.3}$$

where T_{sp} is the kinetic energy of the emitted photoelectron, $h\nu$ is the energy of the source x-rays, E_B indicates the binding energy of the electron emitted by the sample, and ϕ_s is the spectrometer work function [18]. The photoelectron is finally measured by a sixteen-channel detector and its binding energy computed by the system elec-

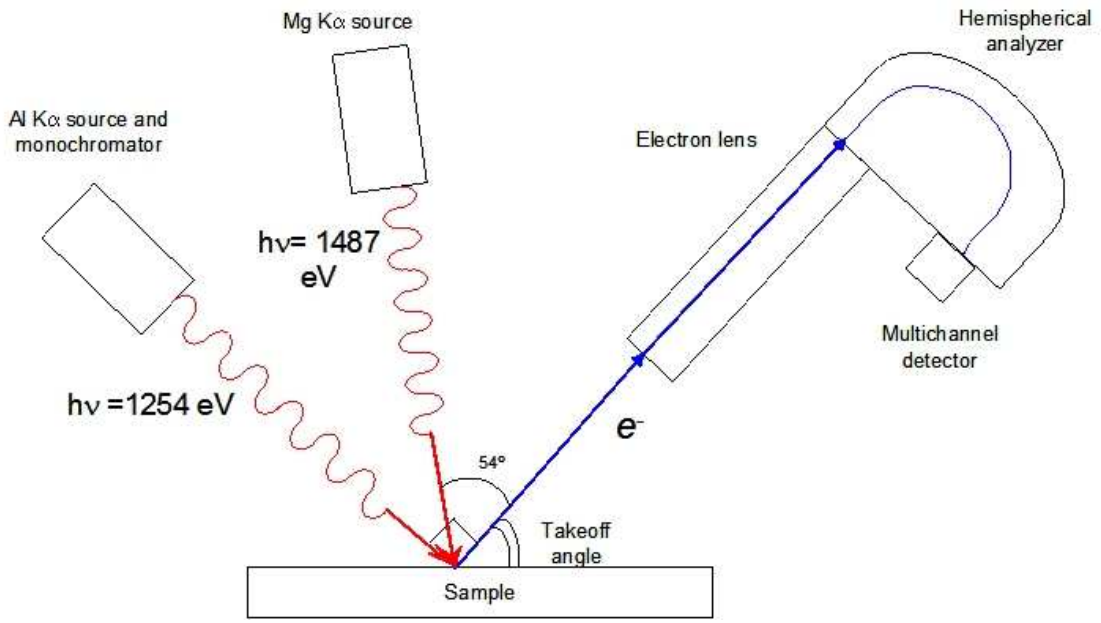

Figure 2.5: Schematic illustration of x-ray photoelectron spectroscopy system. Blue lines illustrate electron paths; red lines illustrate x-ray photon paths. The takeoff angle can be adjusted by the user, but the angles between the sources and detector are fixed.

tronics. The minimum resolution of the detector is 0.6 eV and, in high-resolution mode using the monochromated Al Kα source, the 5800 can attain resolution on the order of 0.05 eV.

The binding energy as measured by the instrument contains a considerable amount of information. The binding energy is defined as the difference in the energy level caused by the emission of the photoelectron, and in absolute terms refers to the energy difference between a core electron level and the Fermi level. Because of this fact the change in energy levels associated with the formation of compounds can be measured. Determination of the exact Fermi level is difficult and usually unnecessary as the core-level peak separations are characteristic of the formation of specific chemical states. This makes it possible to determine the band structure of heterostructures [19, 20].

Peak waveforms are usually modeled as Voigt or pseudo-Voigt functions, the Lorentzian term arising from a lifetime effect (the time resolution of the instrument being too slow to eliminate broadening from the post-ionization recombination process) as well as the natural x-ray linewidth associated with the $h\nu$ term in Eq. 2.3.

The Gaussian term is due to instrument error.

The ionization process results in spin-orbit splitting in p, d, and f levels. Doublets are formed with peak height ratios of 2:1 (p), 3:2 (d), and 4:3 (f). This can complicate the deconvolution if the difference in binding energy is small.

Since peak area is proportional to concentration, it is possible to obtain stoichiometry information. It is necessary to know the effective cross-section of each peak for each element (the "atomic sensitivity factor") relative to other elements. These were determined by the manufacturer for a system of identical configuration.

2.3.2.2 XPS Analysis of Iron Oxide Films

Samples grown by PLD were examined by XPS. Since Fe_3O_4/Si and Fe_3O_4/MgO epitaxy are well understood in the literature, emphasis was placed on bonding states formed upon deposition of iron oxide on GaAs and InAs. Stoichiometry for different PLD parameters was also estimated.

Figure 2.6 summarizes the XPS spectra associated with each stage of deposition. Figure 2.7 shows XPS spectra of the 3d peak of Ga before and after deposition of a thin layer of Fe_3O_4 from a Fe_2O_3 target with no additional oxygen at $T_{sub} = 350°C$. This figure shows the presence of considerable interreaction between the iron oxide and GaAs. Ga-O and As-O bonds [21] are seen as is the formation of a Ga-Fe intermetallic compound [22].

In contrast to Fe_3O_4/GaAs, Fe3O_4/InAs shows very little interfacial reaction. Figure 2.8 is analogous to Fig. 2.6, showing the deposition sequence upon an InAs substrate. Figure 2.9 shows the spectra of this system before and after deposition, using the same growth parameters as for Fig. 2.7. Some In-O reaction is seen.

Stoichiometry of the Fe_3O_4 films was also measured to determine the effect of bleeding O_2 into the chamber during deposition. Figure 2.10 gives deconvolution examples. Analysis is performed with the PHI MULTIPAK package for MATLAB. Baseline calculation is performed with a Shirley algorithm without further subsequent manipulation. Fits are performed to pseudo-Voigt models with reduced $\chi^2 \leq 2$.

Once the peak area is obtained, it is necessary to perform two additional cal-

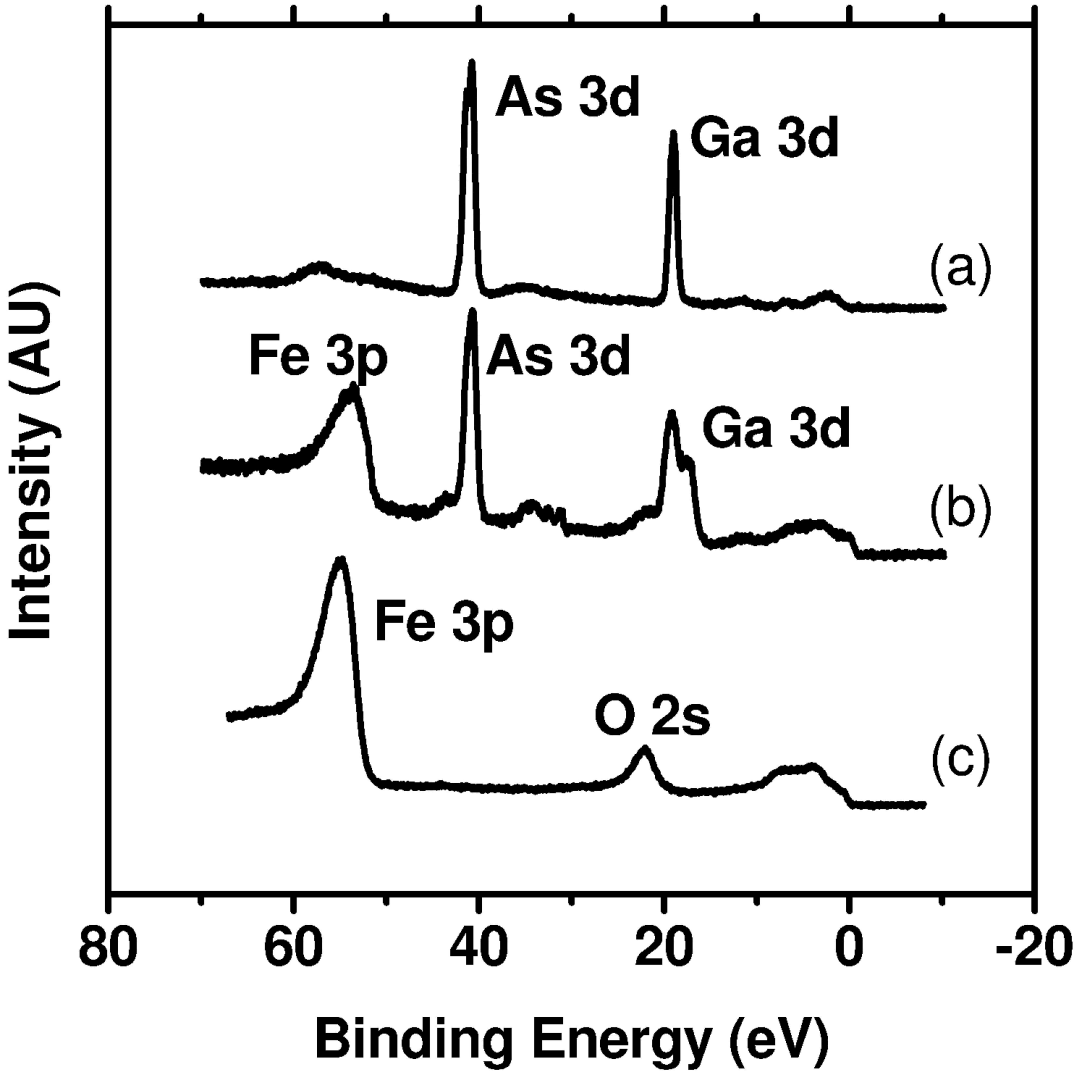

Figure 2.6: Spectra of Fe_3O_4/GaAs. (a) Epitaxial GaAs(001) surface before PLD. (b) After deposition of 50 Åof Fe_3O_4. (c) Thick layer of Fe_3O_4.

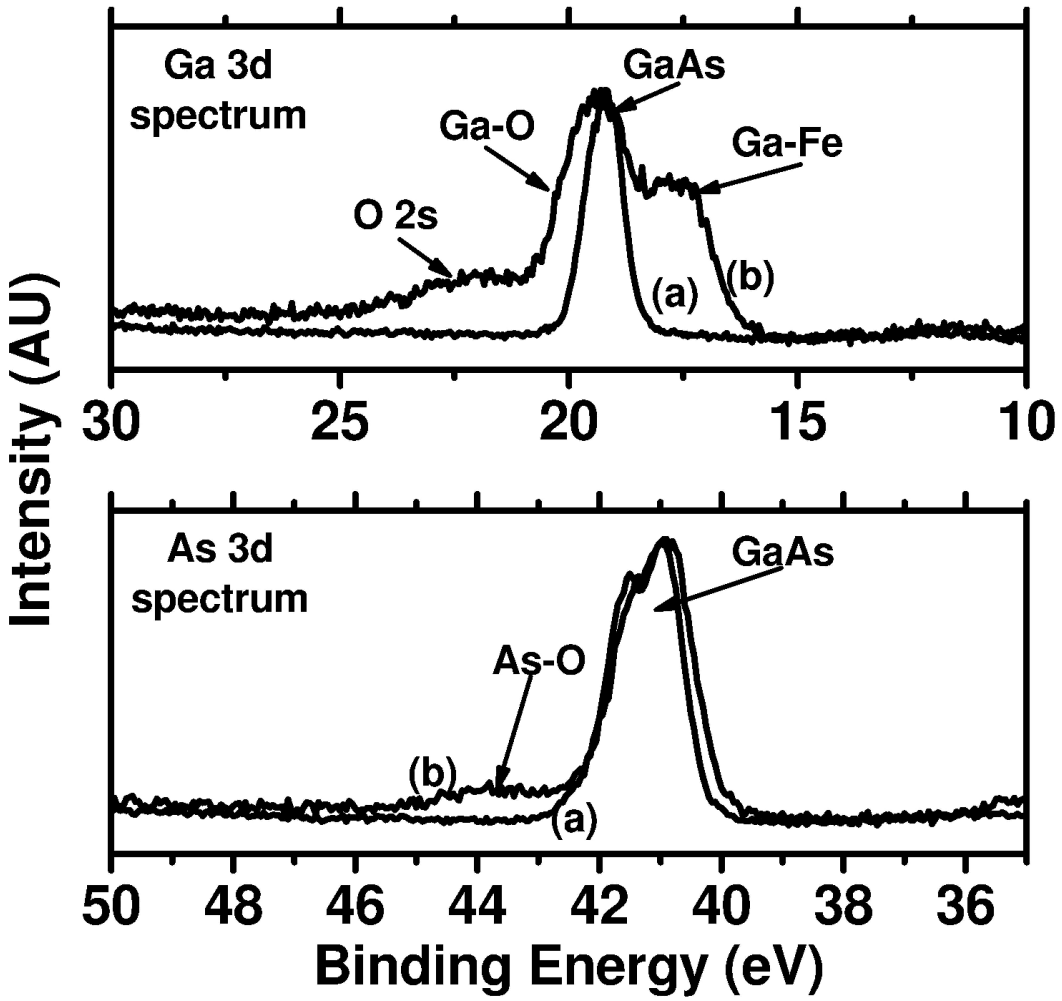

Figure 2.7: Spectra of $Fe3O_4$/GaAs. *Top:* Ga 3*d* spectrum showing original GaAs surface spectrum (a) and spectrum after deposition of 50 Åof Fe_3O_4 (b). *Bottom:* As 3*d* spectrum showing original spectrum (a) and spectrum after oxide growth (b).

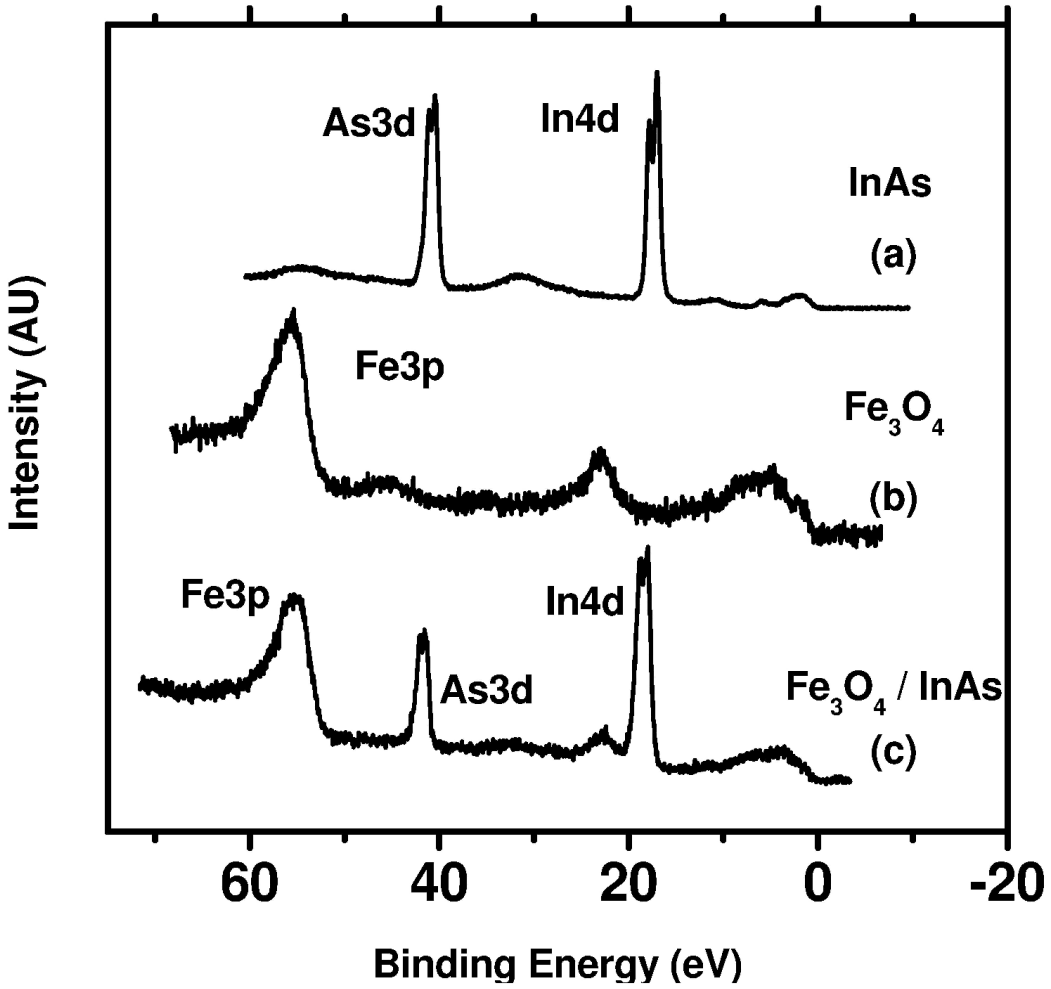

Figure 2.8: Spectra of $Fe3O_4$/InAs. (a) Epitaxial InAs(001) surface before PLD. (b) Thick layer of Fe_3O_4. (c) Epitaxial InAs(001) surface after deposition of 50 Åof Fe_3O_4.

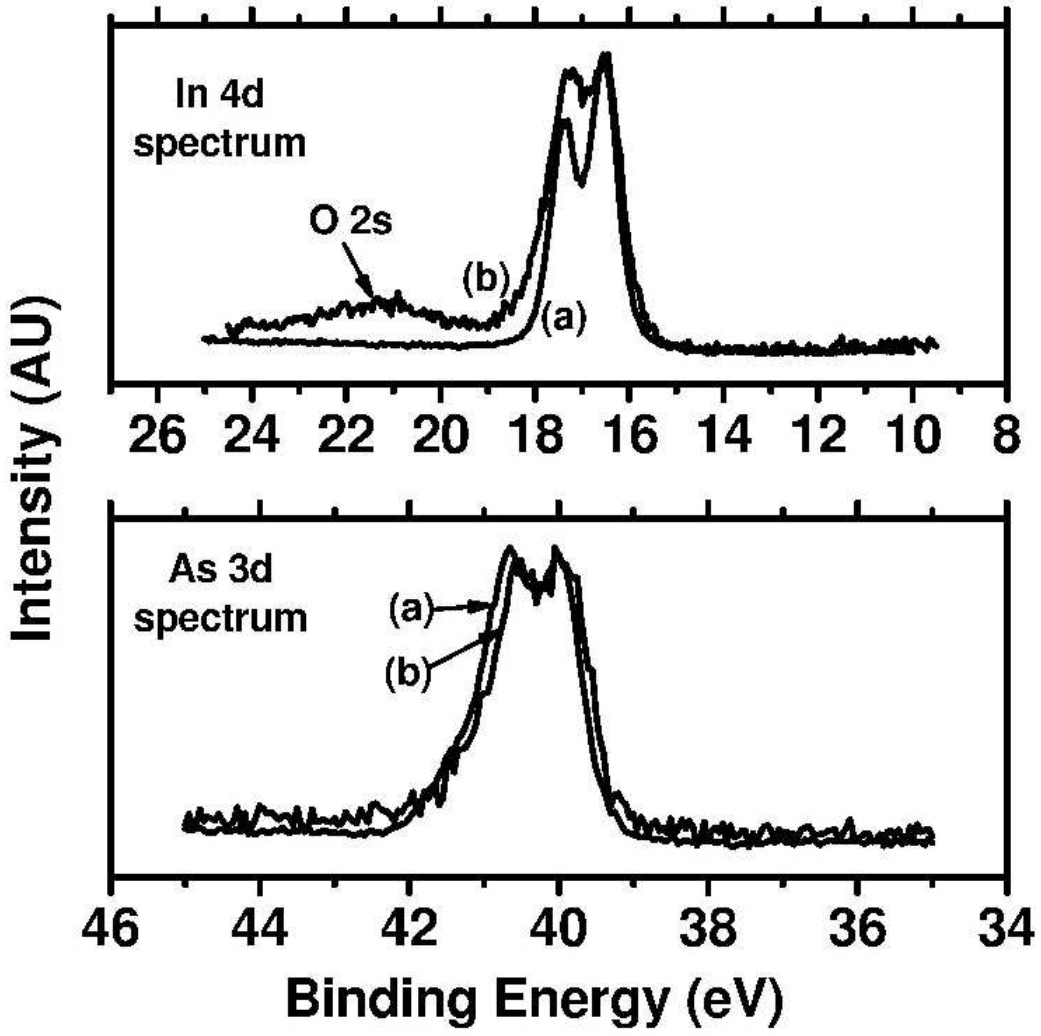

Figure 2.9: Spectra of Fe_3O_4/InAs. *Top:* In 4*d* spectrum showing original InAs surface spectrum (a) and spectrum after deposition of 50 Å of Fe_3O_4 (b). *Bottom:* As 3*d* spectrum showing original spectrum (a) and spectrum after oxide growth (b).

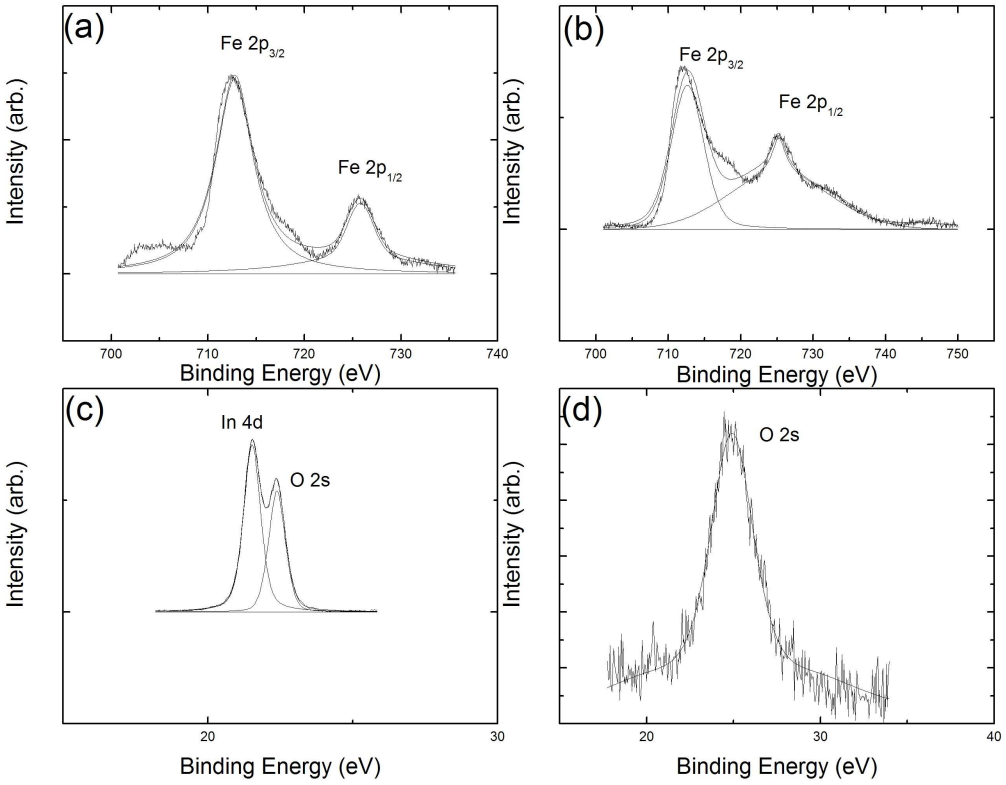

Figure 2.10: Deconvolution of Fe and O spectra for stoichiometry from Fe_3O_4 grown without added oxygen. (a) and (c) are taken with the Mg Kα source; (b) and (d) are taken with the Al Kα monochromated source.

Deposition Process	XPS Feature		Al Kα (90°)	Mg Kα (54°)
Fe_2O_3 target, no O_2(g) input				
	Fe $2p_{3/2}$			
		Peak area	7028	8392
		Peak area / ASF	3924	4258
	O $2s$			
		Peak area	7028	8392
		Peak area / ASF	3924	4258
	[O]/[Fe] ratio		1.306	1.305
Fe_2O_3 target, $P_{O_2(g)} = 5 \times 10^{-6}$ Torr				
	Fe $2p_{3/2}$			
		Peak area	4831	4141
		Peak area / ASF	2697	2101
	O $2s$			
		Peak area	129	110
		Peak area / ASF	4031	3438
	[O]/[Fe]		1.495	1.636

Table 2.1: Measured peak areas for different pulsed laser deposition conditions. ASF = atomic sensitivity factor (see text). Angle between source and detector is given in parentheses.

culations before stoichiometry data is obtained. First, it is necessary to divide the peak area by the relevant atomic sensitivity factor (ASF). While it would be possible to measure samples of known composition to obtain this information, manufacturer-supplied data is more comprehensive and readily available. Finally the relative area must be normalized to the concentration of the other elements in the measured volume. Thus the ratio of two elements A and B is seen to be

$$\frac{[\mathrm{A}]}{[\mathrm{B}]} = \frac{(\text{Peak Area of A})}{(\text{Peak Area of B})} \frac{(\text{ASF of B})}{(\text{ASF of A})} \tag{2.4}$$

For stoichiometry of the iron oxide films the O $2s$ and Fe $2p_{3/2}$ peaks were used as these have historically given consistent results with our instrument. Table 2.1 shows the results. While the variation is significant it appears that addition of $\sim 5 \times 10^{-6}$ torr O_2 promotes the growth of Fe_2O_3.

2.3.3 Crystallography of Iron Oxide Films

The nature of the crystallographic relationship between the iron oxide films and the various substrates was examined by reflection high-energy electron diffraction (RHEED). RHEED is perhaps the most commonly used *in situ* characterization technique for physical epitaxy methods including MBE and PLD. The RHEED system used was manufactured by SVT Associates of Eden Prairie, Minn., and has a maximum beam voltage of 10 kV, although usual operation was at a beam voltage of 8 kV.

The epitaxy of Fe_3O_4 upon MgO(001) surfaces has been well-explored in the literature where the orientation $Fe_3O_4(001)\|MgO(001)$ is reported [23]. Figures 2.11 and 2.12 show the pre- and post-deposition RHEED images of iron oxide grown upon MgO at identical orientations, respectively. What appears to be a twofold reconstruction in Fig. 2.12 is more likely the bulk lattice of the iron oxide film. The lattice constant of Fe_3O_4 (8.40 Å) is twice that of MgO (4.21 Å) and the system exhibits "cube on cube" epitaxy, namely, parallel alignment of the [100] orientations of the two films, which has been established in the literature. This we believe leads to the RHEED relationship seen here. However it is likely this film is not magnetite but is more probably maghemite (γ-Fe_2O_3) or a mixture of maghemite and magnetite. The film of Fig. 2.12 was grown in the presence of 5×10^{-6} torr O_2 and, as was shown in Table 2.1, the stoichiometry of such samples should be nearly Fe_2O_3. Maghemite and magnetite are isostructural, and maghemite has a lattice constant of 8.33 Å(-1.1% with respect to $2a_{\mathrm{MgO}}$).

Laser ablation growth of iron oxide on MgO(001) without the input of oxygen resulted in the RHEED image in 2.13. This surface shows reconstruction and three-dimensional growth. This is likely the $(\sqrt{2} \times \sqrt{2})R45^\circ$ reconstruction reported by Chambers [23].

Characterization of iron oxide films on Si and GaAs substrates was complicated by the fact that the associated RHEED images became very dim and blurry at the beginning of deposition. This is in accordance with the work of Kennedy and Stampe,

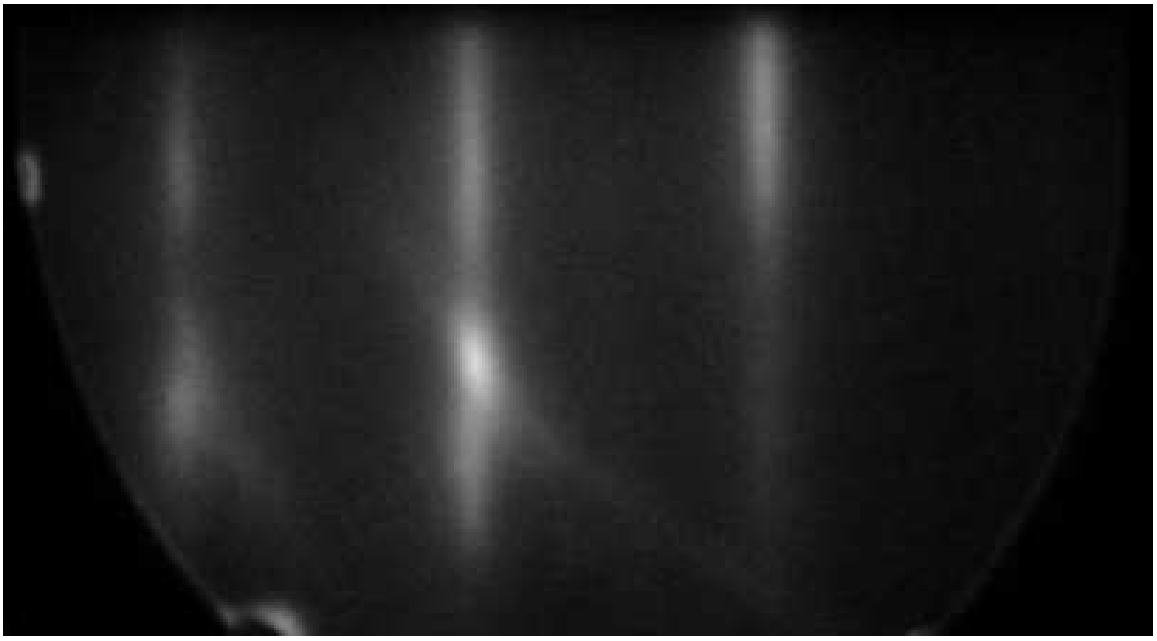

Figure 2.11: RHEED image of (1×1) MgO(001) surface at 350°C

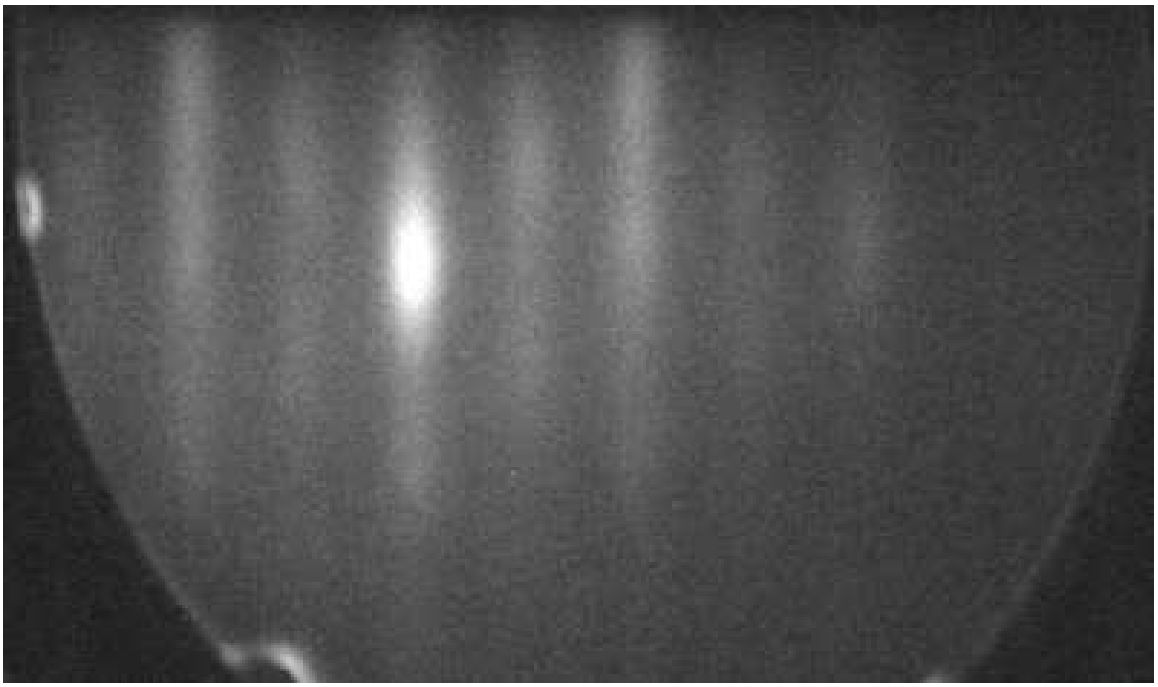

Figure 2.12: RHEED image of (1×1) iron oxide surface at 350°C on MgO substrate. $P_{O_2} = 5 \times 10^{-6}$ torr.

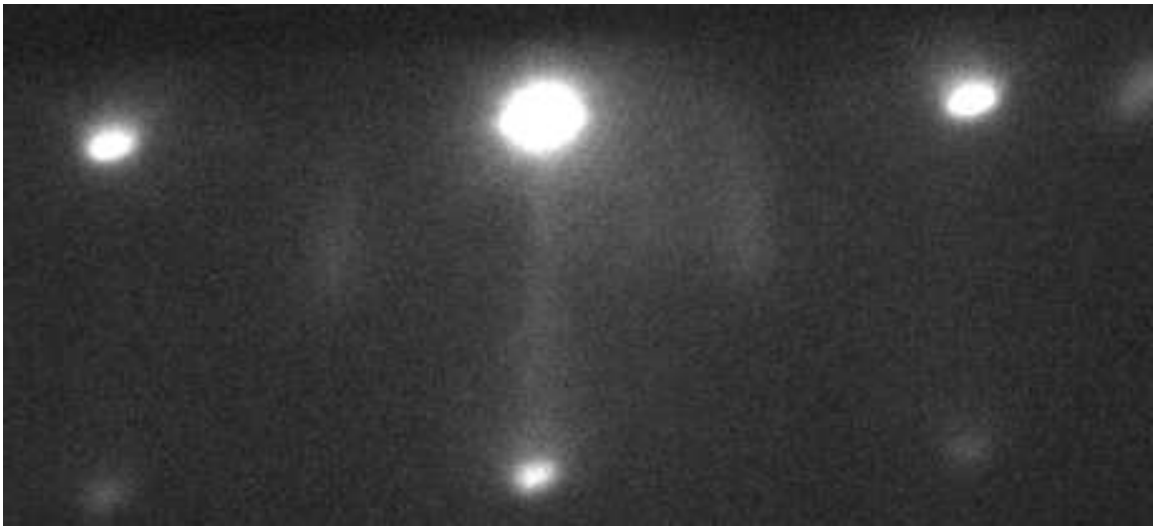

Figure 2.13: RHEED image of Fe_3O_4 surface at 350°C on MgO substrate. No added O_2(g).

who studied iron oxide PLD grown on Si(001) and GaAs(001) substrates using XRD rocking curves and pole figures [6]. In cases such as ours where no epitaxy buffer was grown between the substrate and magnetite, the observed relationship is that growth proceeds in the Fe_3O_4[111] direction. The films are polycrystalline and the grains are randomly oriented in-plane, *i.e.*, the grains are equally likely to assume any orientation that satisfies the condition $Fe_3O_4\{111\}\|$substrate(001).

Figure 2.14 shows images from PLD of magnetite on GaAs. No O_2(g) was added during the growth of this film. The leftmost image shows the bare GaAs surface at 350°C which, due to the absence of any As flux, has assumed the Ga-rich c(4x4) reconstruction [24]. When laser ablation begins this surface vanishes immediately, replaced by the image on the right. The streaks remain in the same location as the substrate holder rotates. This indicates that the sample is polycrystalline with random in-plane grain distribution. Using the GaAs substrate spacings as a guide, the streak spacing was measured to be that expected for Fe_3O_4(111).

Analysis of Fe_3O_4/InAs(001) was unique in that no work in this system is extant in the literature to our knowledge. Our determination is that growth proceeds in the Fe_3O_4[110] direction due to our observation that InAs[$\bar{1}$10]$\|Fe_3O_4$[001]. The argument is as follows: $a_{Fe_3O_4} = 8.40$Å and $a_{InAs} = 6.05$ Å. The diagonal of the InAs(001) face

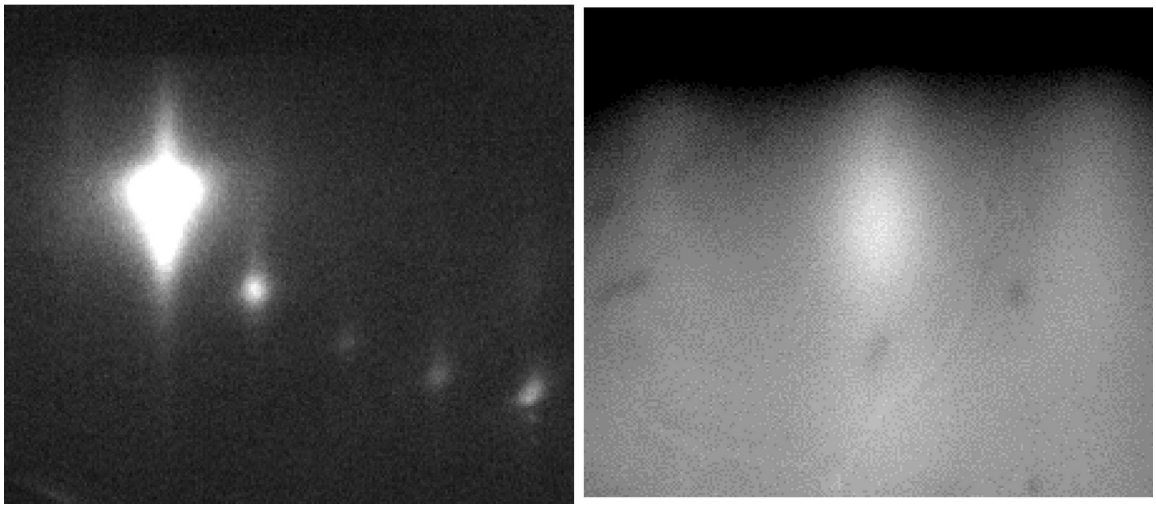

Figure 2.14: *Left*: Bare GaAs(001) surface, $c(4\times4)$ reconstruction, [110] azimuth. *Right*: Fe_3O_4 surface, all azimuths.

is 8.57 Å long. If Fe_3O_4[001] is coincident upon this line (as was seen experimentally) and is growing epitaxially, the linear mismatch is relatively small (-1.98%).

However, the interplanar spacing of $Fe_3O_4(110)$ is $(8.40\text{ Å})/\sqrt{2} = 5.94$ Å. This is what is seen in the second frame of Fig. 2.15; this is a bulk line representing the interplanar spacing and thus allowing identification of the lattice vector. However rotating the sample by 90° finds the InAs[110] lattice direction. There is no geometric relationship betwen the InAs[110] and Fe_3O_4[110] lattice directions.

A schematic illustration of the proposed interface model is given in Fig. 2.16. The fit is believed to minimize the number of unsatisfied oxygen bonds, which is the driving force in heteroepitaxy of oxide compounds upon semiconductors [25]. We examined the possible fits of other faces of Fe_3O_4 in this system and showed that these very poorly satisfied the requirement of satisfying open oxygen bonds [26].

The In layer in the cartoon in Fig. 2.16 is seen to have the full unreconstructed surface. Most properly the surface should demonstrate either a (2×4) As-rich surface or a (4×2) In-rich surface [27, 28, 24]. While growth was performed below 400°C to avoid As desorption, Fig. 2.9 appears to show In-O bonding. Regardless of the species on the surface, the basic geometry is the same. Substitution of the As sublattice would not change the physical nature of the epitaxial relationship, as both sublattices

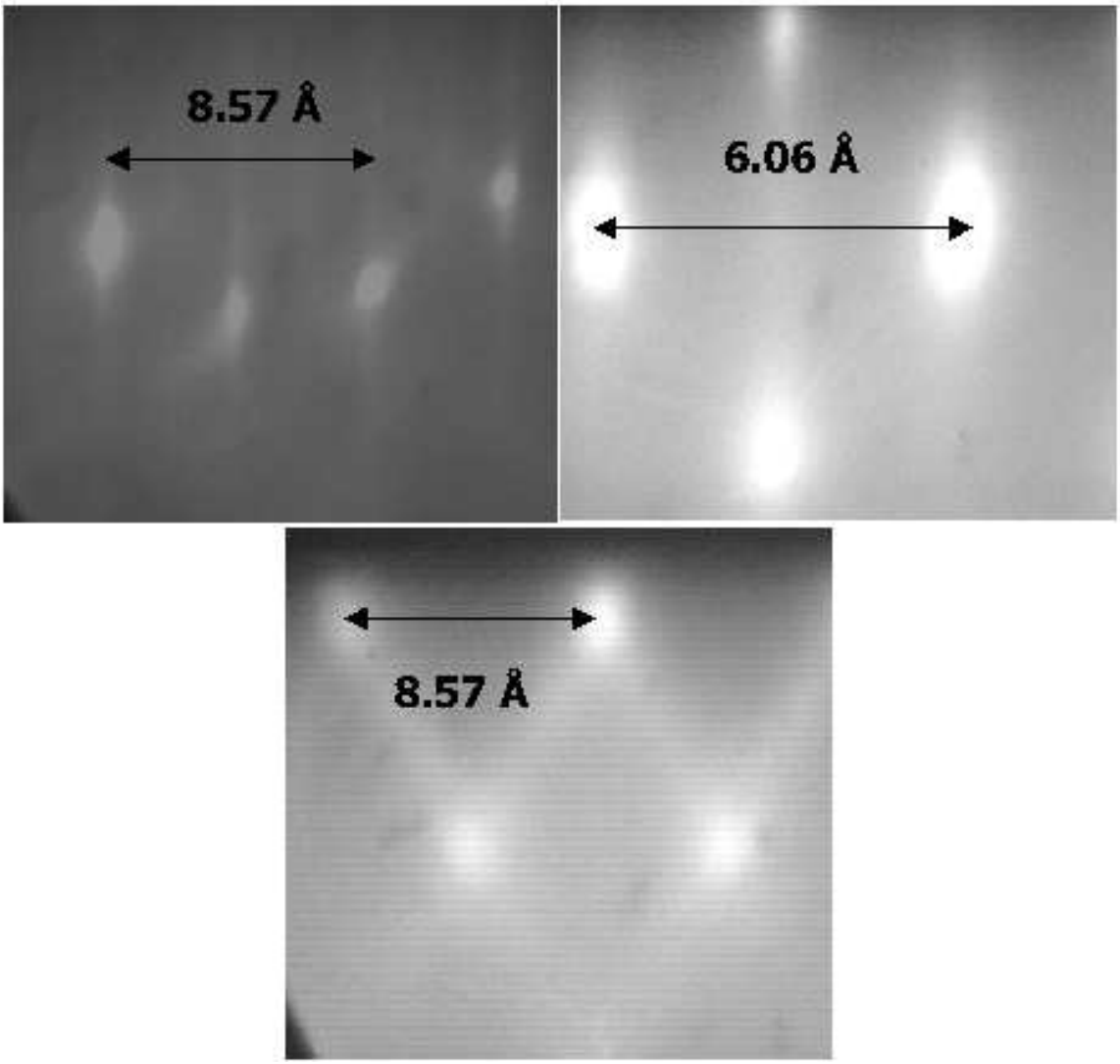

Figure 2.15: RHEED images of growth of Fe_3O_4/GaAs(001). *Top left*: InAs(001) surface, shown at the [110] azimuth (45° from [100]). *Top right*: Same azimuth after deposition of Fe_3O_4. This is a bulk line of Fe_3O_4 (namely, [001]) which is parallel to InAs[110]. *Bottom*: Top right image but rotated by 90°. The spacing is the same as that seen with the bare InAs surface.

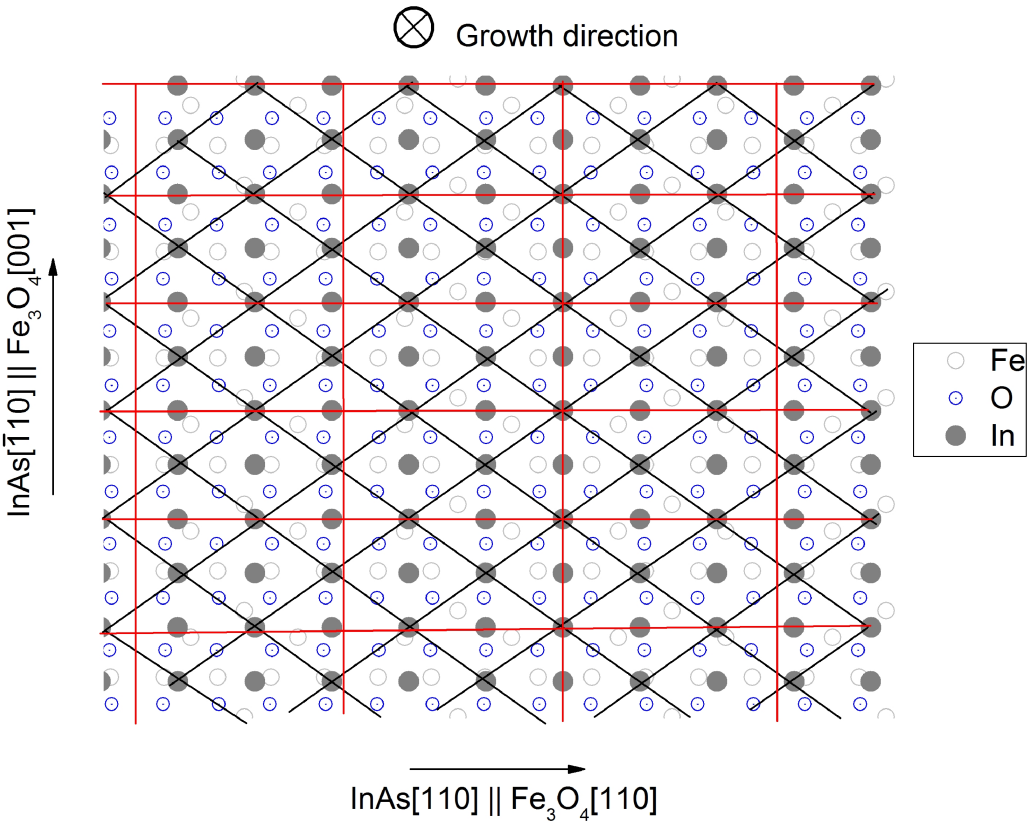

Figure 2.16: Schematic of Fe_3O_4/InAs interface. Growth direction is into the plane of the paper. Fe cations are deemphasized to reflect the importance of oxygen bonding. Red lines show the Fe_3O_4 unit cells; black lines bound the InAs unit cells.

have the same symmetry in the zincblende structure (Herman-Mauguin space group $F\bar{4}3m$).

2.3.4 Analysis of Magnetic Properties Using the Magneto-Optic Kerr Effect

The magneto-optic Kerr effect (MOKE) is a phenomenon which permits facile observations of the magnetic behavior of thin films. A magnetic layer will create optical anisotropy which manifests in a rotation of the polarization angle of reflected plane-polarized light, known as Kerr rotation. Since only the topmost 10-20 nm [29] of the sample contribute to the rotation, the effect is very useful for epitaxial material characterization. Most properly this technique is referred to as MOKE polarimetry but colloquially is known simply as MOKE.

The most important choice in construction of a MOKE apparatus is the selection of sample orientation with respect to the plane of incidence of light and the sense of the applied field vector ($\hat{H}$). There are three possible geometries.

- **Transverse MOKE** The applied field is parallel to the sample surface but normal to the plane of incidence.
- **Polar MOKE** The sense of the applied field lies in the plane of incidence but is normal to the sample surface. This arrangement is suited to probing of perpendicular magnetization.
- **Longitudinal MOKE** The applied field is parallel to the sample surface and its sense also lies in the plane of incidence.

Our MOKE apparatus, seen in Fig. 2.17, is constructed in the longitudinal geometry. Although polar MOKE measurements would have been useful for characterization as well, several technical difficulties are involved with polar MOKE. Most significantly it is necessary to train the laser on the thin edge of a wafer, typically 0.3-0.5 mm thick, which requires special consideration in terms of both sample mounting and optics.

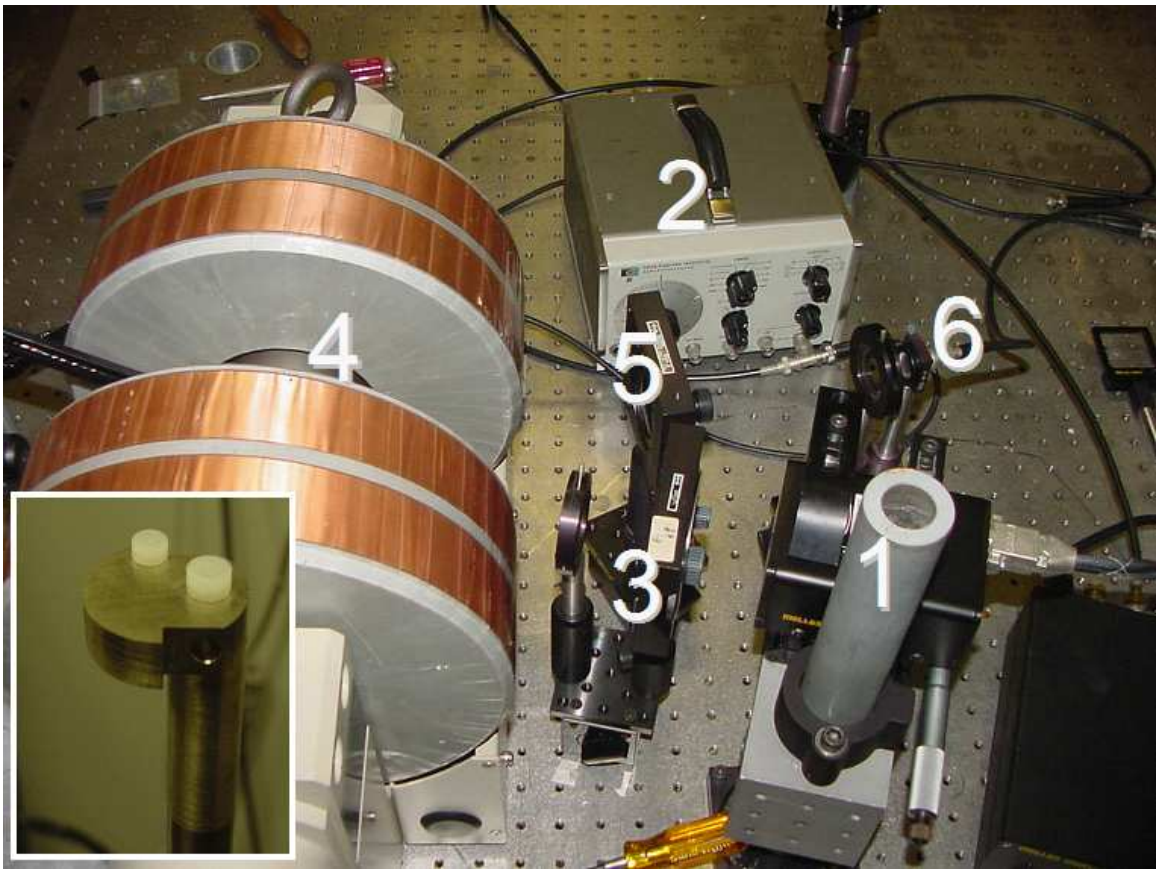

Figure 2.17: The SSDP MOKE polarimetry system. (1) He-Ne laser. (2) Function generator. (3) Polarizer (incident light). (4) Electromagnet. (5) Analyzer (reflected light). (6) Silicon photodiode. The sample holder at bottom left was machined from aluminum bronze, chosen for its extremely small magnetic susceptibility.

In contrast, longitudinal MOKE polarimetry may be performed with arbitrarily large samples. For this reason measurement of magnetization arising from perpendicular applied fields was performed using vibrating sample magnetometry (VSM).

A He-Ne red laser is used as the light source. (It is operated at a frequency of 20 kHz to enable signal measurement using a lock-in amplifier.) The light passes through a linear polarizer whose fast axis is parallel to the poles of the electromagnet. The light is then incident upon the sample. Using the classical Jones formalism of Bland *et al.* [29], the incident light $\vec{\mathcal{E}}^i$ is linearly polarized in the plane of incidence, or "P-plane." The reflected light $\vec{\mathcal{E}}^r$ is given by

$$\begin{pmatrix} \mathcal{E}'_p \\ \mathcal{E}'_s \end{pmatrix} = \begin{pmatrix} r_p & r_{ps} \\ r_{sp} & r_s \end{pmatrix} \begin{pmatrix} \mathcal{E}^i_p \\ 0 \end{pmatrix} \tag{2.5}$$

where the 2×2 matrix represents the complex dielectric matrix elements of the sample material. r_{sp} and r_{ps}, the off-diagonal terms, arise from the magnetism of the sample. The rotation in the polarization vector is known as the Kerr rotation and is given by

$$\tan\theta_K = \mathrm{Re}(r_{sp}/r_p) \tag{2.6}$$

and the intensity change associated with transmission through the analyzing polarizer is

$$\Delta I = 2\theta_K I_0 r_p r_p^* \sin\theta_A \cos\theta_A \tag{2.7}$$

I_0 is the intensity incident upon the sample and θ_A is the angle between the fast axis of the analyzing polarizer and the extinction position (90° from the fast axis of the first polarizer). In our scheme θ_A was set to 1°, meaning that the analyzing polarizer was rotated by 89° from the first polarizer.

The light transmitted through the analyzer is then detected by a commercial Si photodiode. This signal passes through a current preamplifier and then through a lock-in amplifier that is tuned to the function generator controlling the He-Ne laser. The output from the lock-in amplifier is plotted as a function of the magnetic flux between the two poles of the electromagnet, which is varied with time.

Longitudinal MOKE in this configuration is incapable of giving absolute values of permanent magnetic moment. ΔI does not contain $|\mathbf{M}|$ directly. However the hysteretic behavior is evident as a function of applied field and thus our apparatus is very useful as a qualitative diagnostic tool.

Figs. 2.18, 2.19, and 2.20 show the result of scans taken with our MOKE system. The Fe_3O_4 film grown on InAs, while demonstrating more recognizable epitaxy than the other films, is clearly not magnetic.

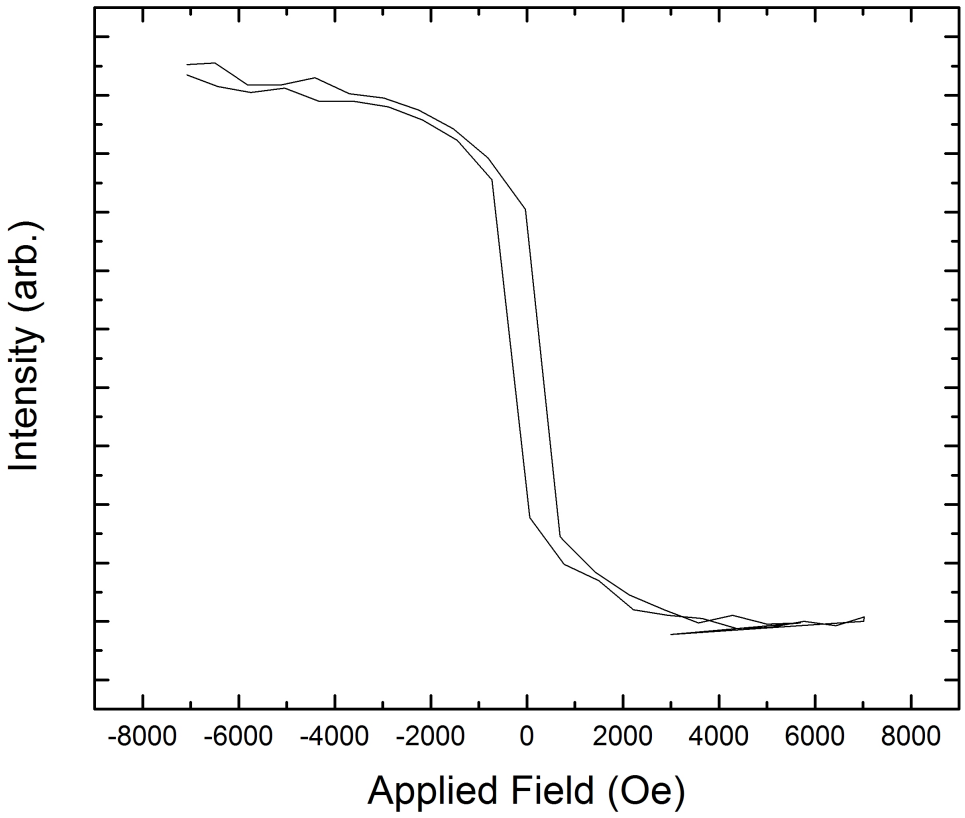

Figure 2.18: Magnetization of Fe_3O_4/Si(111) from MOKE polarimetry.

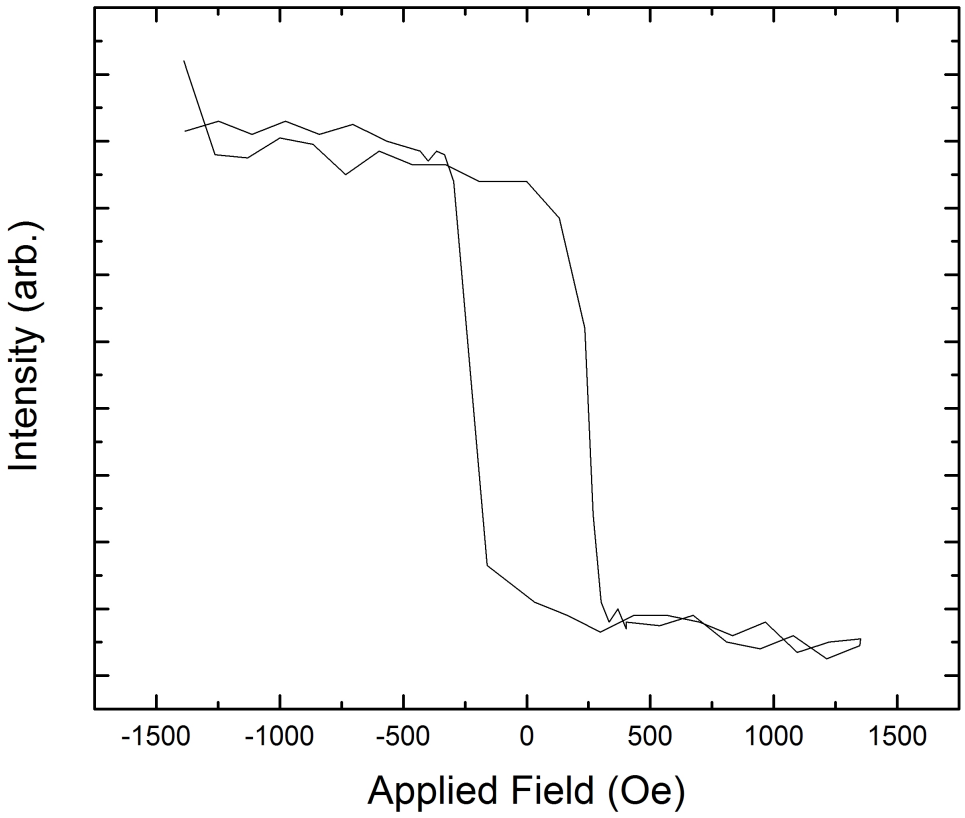

Figure 2.19: Magnetization of Fe_3O_4/MgO(001) from MOKE polarimetry

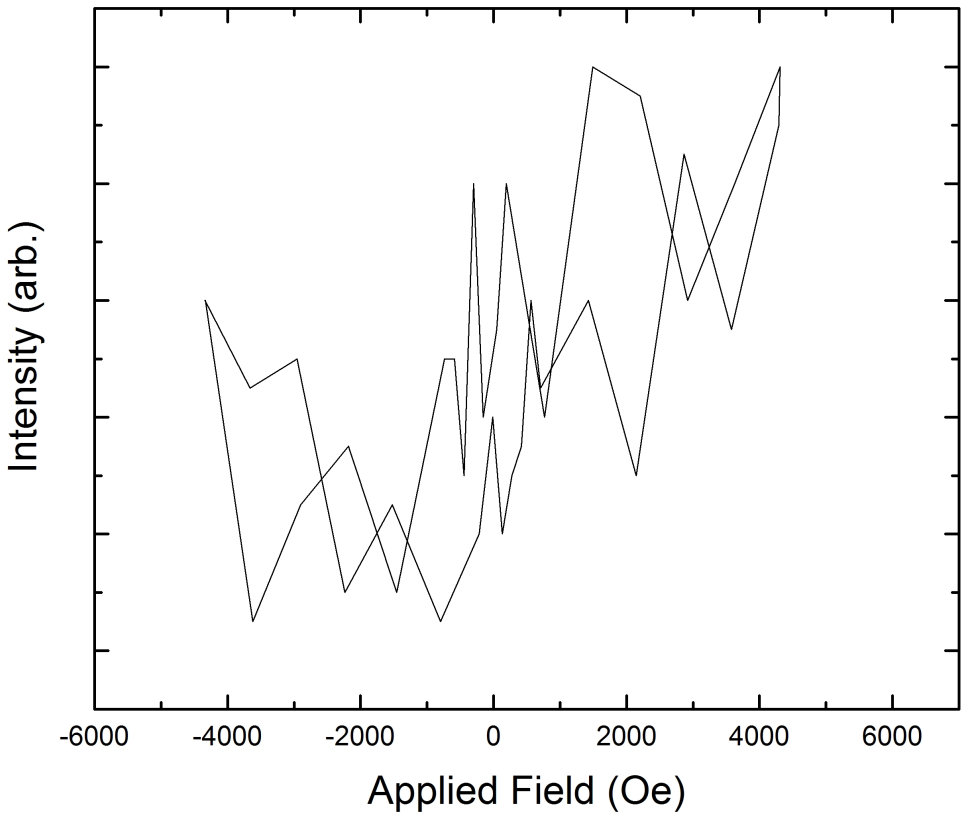

Figure 2.20: MOKE polarimetry scan of Fe_3O_4/InAs(001). Sample exhibits no magnetism.

2.3.5 Analysis of Magnetic Properties Using Vibrating Sample Magnetometry

More detailed analysis of magnetization behavior was desired, namely, quantitative analysis of the magnetization hysteresis. For this the vibrating sample magnetometry (VSM) technique was useful. The sample is oscillated while positioned in a magnetic field and the resultant induction in a sensing coil is measured; locking into the frequency of the oscillation allows measurement of the magnetic moment by the following relation:

$$V = MAfS \tag{2.8}$$

where V is the voltage induced in the sensing coil, M the magnetic moment of the sample, A the amplitude, f the frequency of oscillation, and S the sensitivity. Measurements were performed externally by Lake Shore Cryotronics of Westerville, Ohio, using a Model 7404 VSM. For this instrument, the sensitivity is 0.1 μemu at an air gap (*i.e.*, physical pole separation) of 16.2 mm and a maximum field of 18 kOe. The signal-to-noise ratio (SNR) is dependent upon sample size [30] but varies from 28.5 for a 9 mm^2 sample to 79.3 for a 100 mm^2 sample.

Figures 2.21 and 2.22 give magnetization "loops" for Fe_3O_4 films deposited upon Si(111) and GaAs(001) respectively. Both samples were deposited from Fe_2O_3 targets with no added O_2(g) at $T_{\text{sub}} = 350°C$. The data has been corrected both for the sample holder magnetization ($M_{\text{sample}} = M_{\text{sample and holder}} - M_{\text{holder}}$) and linearized to remove the diamagnetic contributions of the substrates.

From these M vs. H curves it is possible to identify four important materials properties. The saturization magnetization (M_s) is defined as the maximum absolute value of M. The retentivity or remanence (M_r) is the magnetization retained by the film after the applied field is switched off. The coercive field or coercivity (H_c), defined as the intersection of the hysteresis with the abscissa in a plot of M vs H, defines the field above which the sample will retain a permanent magnetic moment. The squareness $S_r \equiv M_r/M_s$ is a measure of the sample's ability to retain its magnetization

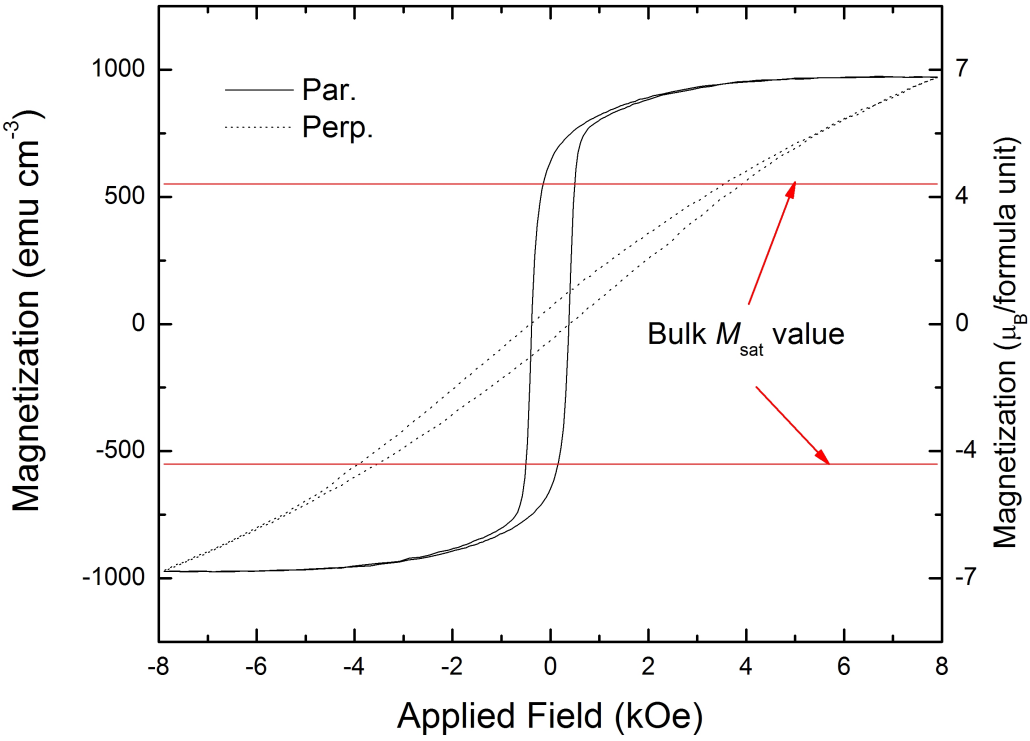

Figure 2.21: VSM analysis of Fe_3O_4/Si(111). "Par" line is for field applied in the sample plane; "perp" denotes field applied normal to the sample plane. Red lines show the literature value of bulk saturated magnetic moment for magnetite.

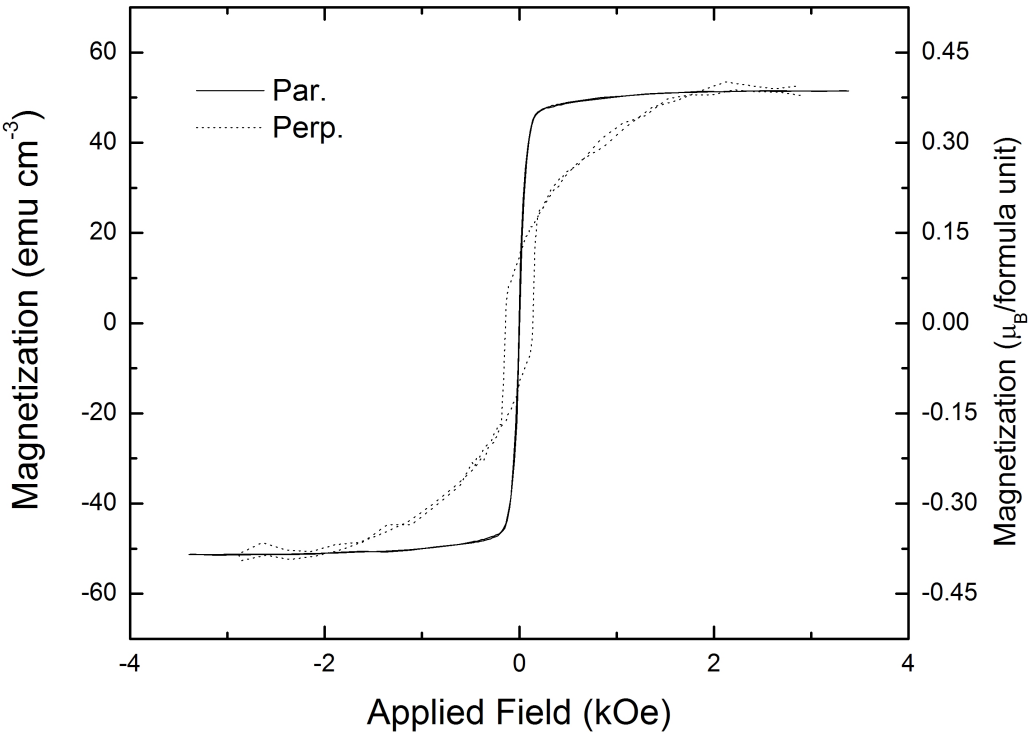

Figure 2.22: VSM analysis of Fe_3O_4/GaAs(001). "Par" line is for field applied in the sample plane; "perp" denotes field applied normal to the sample plane.

	Si(111) Substrate	GaAs(001) Substrate
$H_{c\perp}$ (Oe)	401	141
$H_{c\parallel}$ (Oe)	383	3
M_s (emu cm^{-3})	975	52
$M_{r\perp}$ (emu cm^{-3})	68	14
$M_{r\parallel}$ (emu cm^{-3})	642	2
$S_{r\perp}$	.07	.04
$S_{r\parallel}$	.66	.27

Table 2.2: Summary of magnetic properties of PLD Fe_3O_4 films as determined by VSM.

after H is switched off [8]. For the samples above these properties are summarized in Table 2.2.

The literature value for M_s^{bulk} for Fe_3O_4 is 551 emu cm^{-3} (4.1 μ_B/formula unit). It is seen here that the reported M_s for the Fe_3O_4/Si(111) *exceeds* the bulk value. Kennedy and Stampe also witnessed this phenomenon on both Si(001) and GaAs(001) substrates [6]. They speculated that some regions of elemental Fe could be present; however, they performed ablation from an elemental Fe target. We did not detect unbonded Fe in our XPS studies and to our knowledge no further investigations exist of this topic.

The low M_s and H_c we report for the Fe_3O_4 film grown on GaAs(001) is not understood. It is possible that the interfacial reactions seen in Fig. 2.7 had some deleterious effect on the subsequent microstructure.

2.4 Discussion

The observed epitaxial relationship between Fe_3O_4 and InAs ($Fe_3O_4(110)\|InAs(001)$) cannot be described as a coincidence site lattice (CSL) without strain. The two-dimensional lattice of InAs(001) is a square with lattice constant $a_{\text{InAs}} = 6.05$ Å, and the two-dimensional lattice of $Fe_3O_4(110)$ has dimensions 8.40 Å × 11.9 Å. To describe the interface in terms of a CSL it is necessary that the distance from the origin to some point on the basal lattice be exactly equal to some integer multiple of a lattice constant of the overgrowth lattice [31], a condition which this situation

does not satisfy. Therefore strain is necessary to describe the interface. This may relate directly to the lack of observed magnetism. Jeng and Guo predict that the half-metallicity of magnetite is destroyed (and the magnetization greatly reduced) for in-plane strains less than -1.3% (*i.e.*, for more than 1.3% compression) and greater than $+2.1\%$ [32]. We measured a strain along the in-plane Fe_3O_4[001] direction of 1.86%. This is not quite outside the limits stated by Jeng and Guo, but is comparable to their estimate for the upper limit.

We propose that the use of a metamorphically grown [33] $In_{0.72}Al_{0.28}As$ substrate ($a = 5.93$ Å by Vegard's Law) could allow for the growth of unstrained epitaxial Fe_3O_4. It is not clear what effect the relaxation in the buffer layer would have on properties such as spin lifetime, however, or what the role of aluminum, which reacts strongly with oxygen, would be. Many avenues remain open for exploring integration of magnetite and III-V compound semiconductors.

Bibliography

[1] R. A. de Groot, F. M. Mueller, P. G. van Engen, and K. H. J. Buschow, Phys. Rev. Lett. **50**, 2024 (1983).

[2] J. Coey, M. Venkatesan, and M. Bari, in *High Magnetic Fields: Applications in Condensed Matter Physics and Spectroscopy*, edited by C. Berthier, L. Lévy, and G. Martinez (Springer, Berlin, 2001), p. 377.

[3] J. M. D. Coey, in *Spin Electronics*, edited by M. Ziese and M. J. Thornton (Springer-Verlag, Berlin, 2001), p. 292.

[4] J. M. D. Coey and C. L. Chien, MRS Bull. **28**, 720 (2003).

[5] R. J. Soulen Jr., J. M. Byers, M. S. Osofsky, B. Nadgorny, T. Ambrose, S. F. Cheng, P. R. Broussard, C. T. Tanaka, J. Nowak, J. S. Moodera, A. Barry, and J. M. D. Coey, Science **282**, 85 (1998).

[6] R. J. Kennedy and P. A. Stampe, J. Phys. D. Appl. Phys. **32**, 16 (1999).

[7] M. Pénicaud, B. Siberchicot, C. B. Sommers, and J. Kübler, J. Magn. Magn. Mater. **103**, 212 (1992).

[8] R. C. O'Handley, *Modern Magnetic Materials: Principles and Applications*, 1st ed. (Wiley-Interscience, New York, 2000).

[9] Y. S. Dedkov, U. Rüdiger, and G. Güntherodt, Phys. Rev. B. **65**, 064417 (2002).

[10] D. L. Smith and R. N. Silver, Phys. Rev. B **64**, 045323 (2001).

[11] R. Kelly and A. Miotello, in *Pulsed Laser Deposition of Thin Films*, edited by D. B. Chrisey and G. K. Hubler (Wiley-Interscience, New York, 1994), p. 55.

[12] J. T. Cheung, in *Pulsed Laser Deposition of Thin Films*, edited by D. B. Chrisey and G. K. Hubler (Wiley-Interscience, New York, 1994), p. 14.

[13] M. Ohring, *The Materials Science of Thin Films* (Academic Press, San Diego, 1992), p. 307ff.

[14] *PC-MRD: Software for the Materials Research Diffractometer*, Philips Electronics N.V., 1993.

[15] H. Kiessig, Ann. Phys.-Berlin **10**, 769 (1931).

[16] V. Holý, U. Pietsch, and T. Baumbach, *High-Resolution X-Ray Scattering from Thin Films and Multilayers* (Springer-Verlag, Berlin, 1999), p. 120.

[17] K. Siegbahn, Philos. T. Roy. Soc. A **268**, 1184 (1970).

[18] J. F. Moulder, W. F. Stickle, P. E. Sobol, and K. D. Bomben, *Handbook of X-ray Photoelectron Spectroscopy*, Perkin-Elmer Corporation, 1992.

[19] E. A. Kraut, R. W. Grant, J. R. Waldrop, and S. P. Kowalczyk, Phys. Rev. B **28**, 1965 (1983).

[20] E. T. Yu, J. O. McCaldin, and T. C. McGill, Solid State Phys. **46**, 1 (1992).

[21] E. A. Albanesi, S. J. Sferco, I. Lefebvre, G. Allan, and G. Hollinger, Phys. Rev. B **46**, 13260 (1992).

[22] M. W. Ruckman, J. J. Joyce, and J. H. Weaver, Phys. Rev. B. **33**, 7029 (1986).

[23] S. A. Chambers, Surf. Sci. Rep. **39**, 105 (2000).

[24] W. G. Schmidt, Appl. Phys. A-Mater. **75**, 89 (2002).

[25] M. Yoshimoto, H. Nagata, T. Tsukahara, and H. Koinuma, Jpn. J. Appl. Phys. **29**, L1199 (1990).

[26] E. J. Preisler, J. Brooke, N. C. Oldham, and T. C. McGill, J. Vac. Sci. Technol. B **21**, 1745 (2003).

[27] S. Ohkouchi and N. Ikoma, Jpn. J. Appl. Phys. **33**, 3710 (1994).

[28] C. Ohler, C. Daniels, A. Förster, and H. Lüth, J. Vac. Sci. Technol. B **15**, 702 (1997).

[29] J. A. C. Bland, M. J. Padgett, R. J. Butcher, and N. Bett, J. Phys. E Sci. Instrum. **22**, 308 (1989).

[30] B. C. Dodrill, The Performance of the Model 7400 VSM: Sensitivity, Lake Shore Cryotronics, Inc.

[31] T. Hondoh, in *Lattice Defects in Ice Crystals*, edited by A. Higashi (Hokkaido University Press, Sapporo, Hokkaido, 1988), pp. 131–132.

[32] H.-T. Jeng and G. Y. Guo, Phys. Rev. B **65**, 094429 (2002).

[33] P. Win, Y. Druelle, A. Cappy, Y. Cordier, J. Favre, and C. Bouillet, Appl. Phys. Lett. **61**, 922 (1992).

Chapter 3

Metallurgy of Thin-Film Cobalt-Chromium Alloys

3.1 Motivation

The majority of schemes for efficient injection of spin-polarized current into semiconductors depend upon thin-film ferromagnetic contacts. Thin ferromagnetic films, almost without exception, exhibit a preference for in-plane or "parallel" magnetization. The optical detection device outlined in Fig. 1.3 requires that the magnetic field be parallel to the direction of propagation of the emitted light, since the circular polarization indicative of efficient injection is referenced to the sense of the magnetic field vector. Ejecting the elliptically polarized light from the side of the device instead of the top is theoretically permitted but the observed intensity is $\sim 0.7\%$ of the signal from top emission [1]. Some workers have exploited the oblique Hanle effect to create out-of-plane magnetization [2, 3] with fields smaller than those needed for the $H \parallel z$ configuration shown in Fig. 1.3 and used by workers such as Hanbicki *et al.* [4]. These fields are applied at an angle between parallel and perpendicular orientations. However the need for an external applied field has not been eliminated to date.

We describe here an attempt to fabricate a thin-film ferromagnet which naturally has an out-of-plane or "perpendicular" easy axis. The goal of this work is to create a contact which retains a significant perpendicular magnetic moment after magnetization and thus can be used in $H = 0$ configurations, leading to spin injection devices

for which injection is possible in the out-of-plane direction and which do not require operation in large electromagnets or superconducting magnets.

In-plane magnetization occurs in most ferromagnetic thin films because, in a typical randomly oriented polycrystalline sample, the magnetostatic energy of the shape dominates the net magnetic moment. O'Handley gives the demagnetizing factor N of a cylinder. If we treat a thin film as a cylinder whose length/diameter ratio approaches zero, $N \simeq 1$ [5]. The magnetostatic energy density u in MKS units is

$$u = \frac{\mu_0 N M^2}{2} \tag{3.1}$$

where M is the magnitude of the magnetic moment normal to the surface under consideration and μ_0 is the permeability of vacuum. The magnetostatic energy density can only be minimized if $M_\perp$ is minimized. The influence of the geometry of the magnet on the magnetization orientation energetics is referred to as shape anisotropy.

Another important consideration is crystalline anisotropy. The crystallographic orientation with the lowest energy for magnetization is referred to as the easy axis. Iron and nickel, both cubic crystals, have easy axes of <100> and <111>, respectively, which are high-multiplicity directions. This implies that even in an epitaxial film, some easy-axis crystallographic orientation will likely be found in the film plane. Cobalt however has a [0001] easy axis in its hcp phase (ϵCo). If pure Co films are grown in a randomly oriented polycrystalline manner the resulting shape anisotropy will dominate and the preferred magnetization will be in-plane as seen with Fe and Ni. However, deliberately prepared films of sputtered cobalt-chromium alloys were demonstrated in 1975 to show perpendicular magnetic anisotropy [6]. This generated considerable interest in the magnetic recording industry. The mechanism was not correctly understood until Maeda *et al.* utilized plan-view transmission electron microscopy (TEM) of wet-etched thin foils of Co-Cr to study the microstructure [7]. Their results are shown in Fig. 3.1. A partial phase diagram for temperatures below 400°C is given in Fig. 3.2.

Cobalt-chromium alloys with a Cr content between $\sim$ 10 and 27 at.% are allowed

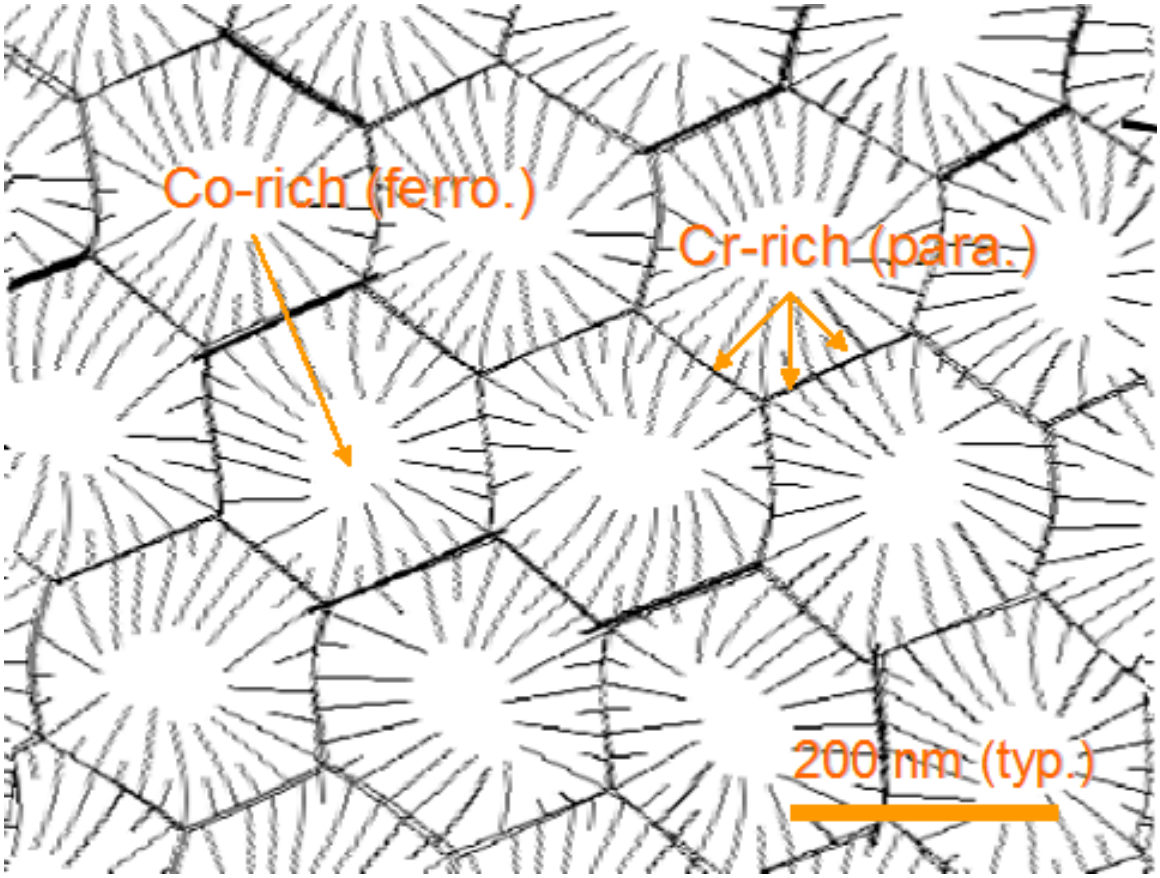

Figure 3.1: Plan view of the microstructure of Co-Cr alloy displaying out-of-plane easy axis. The white regions at the center of the grains are hcp cobalt; the black lines are a paramagnetic Cr-rich phase (approximately 35 at.% Cr).

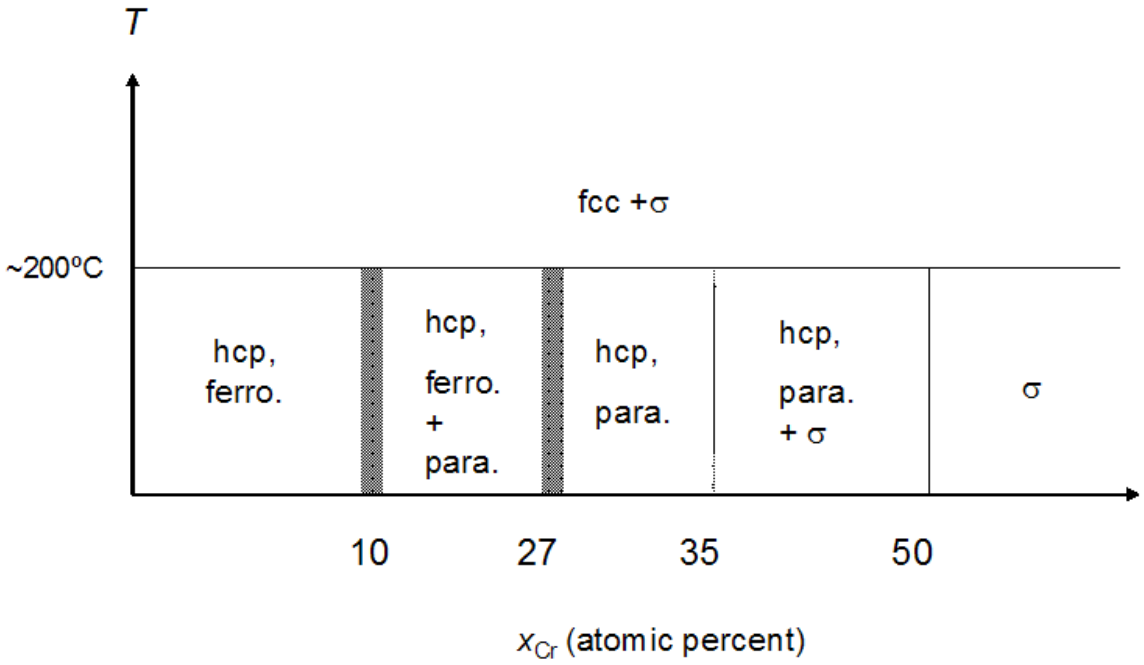

Figure 3.2: Phase diagram of Co-Cr system at room temperature. After [7]. The σ phase is the intermetallic compound Cr_3Co_2.

to have an out-of-plane easy axis. The mechanism for this is as follows.

1. Grains grow in columnar fashion, specifically with the Co[0001] direction parallel to the growth direction. See Sec. 3.4.2 for a discussion of formation of this morphology. The crystalline anisotropy is now favorable to out-of-plane magnetization. This is a necessary condition, but not a sufficient one.

2. The Cr-rich phase is immiscible in the Co-rich phase (Fig. 3.2) and segregates from it, radiating toward the grain boundaries in the chrysanthemum pattern.

3. This paramagnetic Cr-rich phase decouples the magnetic domains of the individual grains.

4. For cylinders with a length/diameter ratio approaching infinity, the demagnetizing factor N in Eq. 3.1 approaches zero [5]. Thus the magnetostatic energy is now minimized with M oriented perpendicular to the film plane,

not parallel to it, and shape anisotropy as well as crystalline anisotropy now requires out-of-plane magnetization. These are necessary and sufficient conditions.

Deposition of Co-Cr thin-film alloys primarily has been performed with sputtering. Perpendicular magnetization does not seem tied to any substrate; perpendicular anisotropy has been shown on SiO_2 [8, 9, 10, 11], polymers [12], amorphous carbon TEM grids [9, 10], Fe-Ni alloys [13], and silicon [9]. Techniques have included sputtering [8, 9, 11], and electron-beam evaporation [12]. Substrate temperatures ranged from 150°C [9] to 170° and up [11]. We conclude from the literature that perpendicular magnetization is not very dependent upon the substrate material and as such this will not be an important factor in the properties of the films.

3.2 Dual-Source Deposition of Co-Cr Thin Films

Initial attempts to deposit thin-film Co-Cr perpendicular magnets utilized two-gun electron-beam (or "e-beam") evaporation (EBE). The basic mechanism of EBE is shown in in Fig. 3.3. The system used for this work consists of an ultrahigh vacuum (UHV) chamber mounting dual Thermionics Model 100-0040 guns, each with four 2.2-cm^3 crucibles. A Thermionics SEB-06 power supply delivers a bias of up to 6 kV to the the tungsten cathode filaments with respect to their anodes. The system also includes current controls, which may be operated manually or externally through BNC connectors.

High current passes through the filament, resulting in thermionic emission of electrons. A permanent magnet with its south pole closest to the air side (such that $\vec{B}$ points toward the gun flange) steers the electron beam onto the crucible, which heats the source and results in evaporation. Evaporant is deposited upon the growth substrate, which may be heated. Adjusting the source bias controls the lateral deflection of the e-beam.

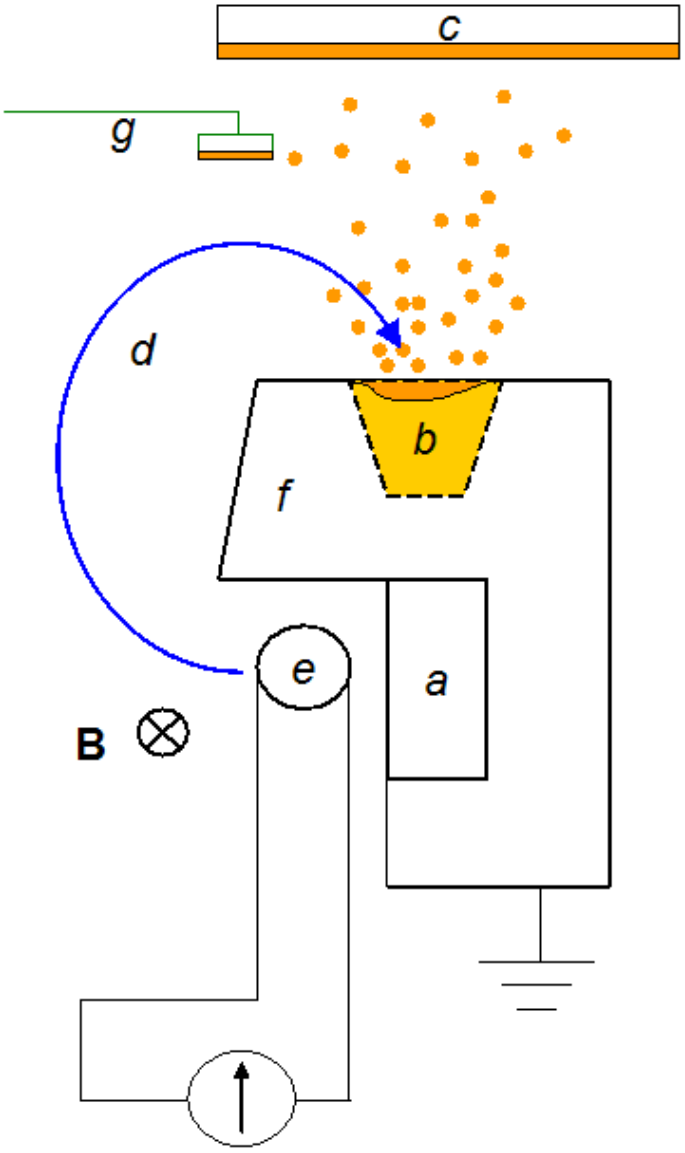

Figure 3.3: Schematic illustration of EBE. (a) Permanent magnet with north pole closest to viewer; south pole obscured by north pole. (b) Source in insulating crucible liner, typically FABMATE^{TM}graphite. (c) Substrate and growing film. (d) Electron beam. (e) Filament (cathode). (f) Anode (grounded). (g) Quartz crystal monitor.

Deposition is monitored by quartz crystal monitors (QCMs). These function by measuring the change in resonant frequency of the crystal during deposition and relating that to the deposited mass. [14]. This is referred to as the Z-match technique for which the shear moduli of the deposited materials must be known since the thickness read by the monitor is given by

$$h_{\text{film}}(t) = \frac{A}{\rho_{\text{film}} f(t) Z} \arctan\left(Z \tan(\frac{\pi(f_0 - f(t))}{f_0})\right) \tag{3.2}$$

where A is a quartz material constant, t is the time elapsed since the beginning of measurement, h_{film} is the deposited film thickness, $f(t)$ is the resonant frequency of the quartz crystal at t, f_0 is the resonant frequency at the beginning of measurement, and Z represents the acoustic impedance ratio

$$Z = \sqrt{\frac{\rho_{\text{quartz}} G_{\text{quartz}}}{\rho_{\text{film}} G_{\text{film}}}} \tag{3.3}$$

ρ_M representing the density of material M and G_M the shear modulus of M. An approximation was used for the Co-Cr materials properties: $\rho_{\text{film}} \simeq 0.8\rho_{\text{Co}} + 0.2\rho_{\text{Cr}} = 8.404$ g cm^{-3} and $G_{\text{film}} \simeq 0.8G_{\text{Co}} + 0.2G_{\text{Cr}} = 97.9$ MPa, giving $Z \simeq 0.327$ which was used for all EBE experiments in this chapter.

The geometric error related to the location of the crystal monitor with respect to the substrate must also be calibrated. Referred to as the "tooling factor," this represents the ratio of material deposited upon the monitor to material deposited on the substrate.

Our chamber has two QCM feedthroughs which may be connected either to a pair of Inficon XTC monitor-controllers or to a single Leybold-Inficon XTM/2 monitor. The former formed the basis of a proposed scheme for Co-Cr deposition. As both guns could be operated simultaneously, EBE from elemental Co and Cr sources was an obvious method for attempting to grow perpendicular Co-Cr magnets. In this scheme, dual-source deposition would be controlled by a feedback loop where each XTC was connected to a specific QCM, measured the deposition rate on that QCM, and adjusted the current through one of the guns. This requires a degree of mathe-

matical manipulation as each gun deposits on both crystal monitors. If the tooling factor is accurately measured for each monitor for each element in separate runs, it is possible to calculate the deposited amount of each element and determine the volume fraction of each in the deposited film.

For purposes of calibration, $F_{i+1} = F_i h_{act}/h_{disp}$, where F_i is the initial guess for the tooling factor, F_{i+1} is the actual tooling factor, and h_{act} and h_{disp} are the actual deposited thickness and reported thickness, respectively. Also for films of unknown density $\rho_{i+1} = \rho_i h_{disp}/h_{act}$. We can conceive of these "initial guesses" not as erroneous quantities but inputs used to determine the parameters which allow the controllers to produce the desired rate of deposition of different materials. We note both calibration equations assume the other quantity (density or tooling) is correctly set. Defining F_{in} and ρ_{in} as the tooling and density input into a given controller and F_{act} and ρ_{act} as the true tooling and density for that controller,

$$h_{disp} = \frac{\rho_{act}}{\rho_{in}} \frac{F_{in}}{F_{act}} h_{act}$$

Consider a case where two sources, one of element A and another of element B, are evaporating onto the QCM. The tooling factor for each element with respect to the QCM will be different since each source is located in a different location and thus has a different geometry associated with it. This situation gives

$$\begin{aligned} h_{disp} &= \frac{\rho^A_{act}}{\rho_{in}} \frac{F_{in}}{F^A_{act}} h^A_{act} + \frac{\rho^B_{act}}{\rho_{in}} \frac{F_{in}}{F^B_{act}} h^B_{act} \\ &= \frac{F_{in}}{\rho_{in}} \left(\frac{\rho_A}{F^A_{act}} h^A_{act} + \frac{\rho_B}{F^B_{act}} h^B_{act} \right) \end{aligned} \tag{3.4}$$

Now we consider that there are two controller-monitors. We denote the thicknesses as matrices,

$$\underline{h}_{act} = \begin{pmatrix} h^{\mathrm{Co}}_{act} \\ h^{\mathrm{Cr}}_{act} \end{pmatrix}$$

and

$$\underline{h}_{disp} = \begin{pmatrix} h_{disp}^{\mathrm{Co}} \\ h_{disp}^{\mathrm{Cr}} \end{pmatrix}$$

This allows the construction of a matrix equation which describes the situation in our chamber. Superscripts "I" and "II" denote quantities pertaining to a specific QCM.

$$\underline{h}_{disp} = \underline{\underline{M}}\underline{h}_{act} \tag{3.5}$$

$$\underline{\underline{M}} = \begin{pmatrix} \frac{F_{in}^{I}\rho_{\mathrm{Co}}}{\rho_{in}^{I}F_{\mathrm{Co}}^{I}} & \frac{F_{in}^{I}\rho_{\mathrm{Cr}}}{\rho_{in}^{I}F_{\mathrm{Cr}}^{I}} \\ \frac{F_{in}^{II}\rho_{\mathrm{Co}}}{\rho_{in}^{II}F_{\mathrm{Co}}^{II}} & \frac{F_{in}^{II}\rho_{\mathrm{Cr}}}{\rho_{in}^{II}F_{\mathrm{Cr}}^{II}} \end{pmatrix} \tag{3.6}$$

It is also useful to know the inverse of $\underline{\underline{M}}$ to determine the volume fraction of the elements in a deposited film. This is given by

$$\underline{\underline{M}}^{-1} = \begin{pmatrix} (M^{-1})_{11} & (M^{-1})_{12} \\ (M^{-1})_{21} & (M^{-1})_{22} \end{pmatrix} \tag{3.7}$$

$$(M^{-1})_{11} = \frac{\rho_{in}^{I}F_{\mathrm{Co}}^{I}F_{\mathrm{Co}}^{II}F_{\mathrm{Cr}}^{I}}{\rho_{\mathrm{Co}}F_{\mathrm{Co}}^{II}F_{\mathrm{Cr}}^{I}F_{in}^{I} - \rho_{\mathrm{Co}}F_{\mathrm{Co}}^{I}F_{\mathrm{Cr}}^{II}F_{in}^{I}} \tag{3.8}$$

$$(M^{-1})_{12} = \frac{\rho_{in}^{II}F_{\mathrm{Co}}^{I}F_{\mathrm{Co}}^{II}F_{\mathrm{Cr}}^{II}}{\rho_{\mathrm{Co}}F_{\mathrm{Co}}^{I}F_{\mathrm{Cr}}^{II}F_{in}^{II} - \rho_{\mathrm{Co}}F_{\mathrm{Co}}^{II}F_{\mathrm{Cr}}^{I}F_{in}^{II}} \tag{3.9}$$

$$(M^{-1})_{21} = \frac{\rho_{in}^{I}F_{\mathrm{Co}}^{I}F_{\mathrm{Cr}}^{II}F_{\mathrm{Cr}}^{I}}{\rho_{\mathrm{Cr}}F_{\mathrm{Co}}^{I}F_{\mathrm{Cr}}^{II}F_{in}^{I} - \rho_{\mathrm{Cr}}F_{\mathrm{Co}}^{II}F_{\mathrm{Cr}}^{I}F_{in}^{I}} \tag{3.10}$$

$$(M^{-1})_{22} = \frac{\rho_{in}^{II}F_{\mathrm{Co}}^{II}F_{\mathrm{Cr}}^{II}F_{\mathrm{Cr}}^{I}}{\rho_{\mathrm{Cr}}F_{\mathrm{Co}}^{II}F_{\mathrm{Cr}}^{I}F_{in}^{II} - \rho_{\mathrm{Co}}F_{\mathrm{Co}}^{I}F_{\mathrm{Cr}}^{II}F_{in}^{II}} \tag{3.11}$$

These values were calibrated by growing elemental samples by EBE and measuring the film thickness with variable-angle spectroscopic ellipsometry (VASE). However, one crystal monitor was found to have no measurable line of sight to the Co source

	First dual-source	Second dual-source
$H_{c\perp}$ (Oe)	325.39	654.05
$H_{c\parallel}$ (Oe)	22.765	458.82
M_s (emu cm^{-3})	1200	600
$M_{r\perp}$ (emu cm^{-3})	1200	80
$M_{r\parallel}$ (emu cm^{-3})	1100	300
$S_{r\perp}$	0.99169	0.13578
$S_{r\parallel}$	0.96771	0.45445

Table 3.1: Summary of magnetic properties of dual-source EBE Co-Cr films. Magnetization values are normalized to estimated sample volume.

and thus $F^I_{Co} = 0$. As may be seen in Eq. 3.6 this leads to division by zero in matrix element M_{11}. While this problem may be addressed earlier in the derivation by omitting one of the terms in Eq. 3.4, and thus setting $M_{22} = 0$, our system is not sufficiently agile to compensate for the associated incomplete feedback. Thus it was necessary to manually adjust the gun currents to maintain stable output. A single QCM was used to measure growth using a density value of 8.4 g cm^{-3} (see above) and a tooling factor of 100%. Since measured tooling factors were between 90% and 110% the associated thickness error was 10%.

Two samples were grown by the dual-source method and measured by VSM (Sec. 2.3.5). For both films $T_{sub} = 190$°C. This is below the reaction at 200°C and also similar to literature temperatures [11]. In Fig. 3.4 the film demonstrates excellent perpendicular magnetization; the second film (Fig. 3.5) had poor squareness.

Magnetic properties are summarized in Table 3.1. Simultaneous manual deposition of Co and Cr is very difficult to to perform since over most deposition temperatures the vapor pressure of Cr is at least one order of magnitude higher than that of Co (Sec. 3.4.1).

The inconsistency between runs, in addition to other mechanical difficulties with the dual deposition system, motivated a search for another deposition technique which would allow UHV-contained deposition of perpendicularly magnetizing thin films upon semiconductor spin detector structures with better reproducibility than the dual-source EBE method.

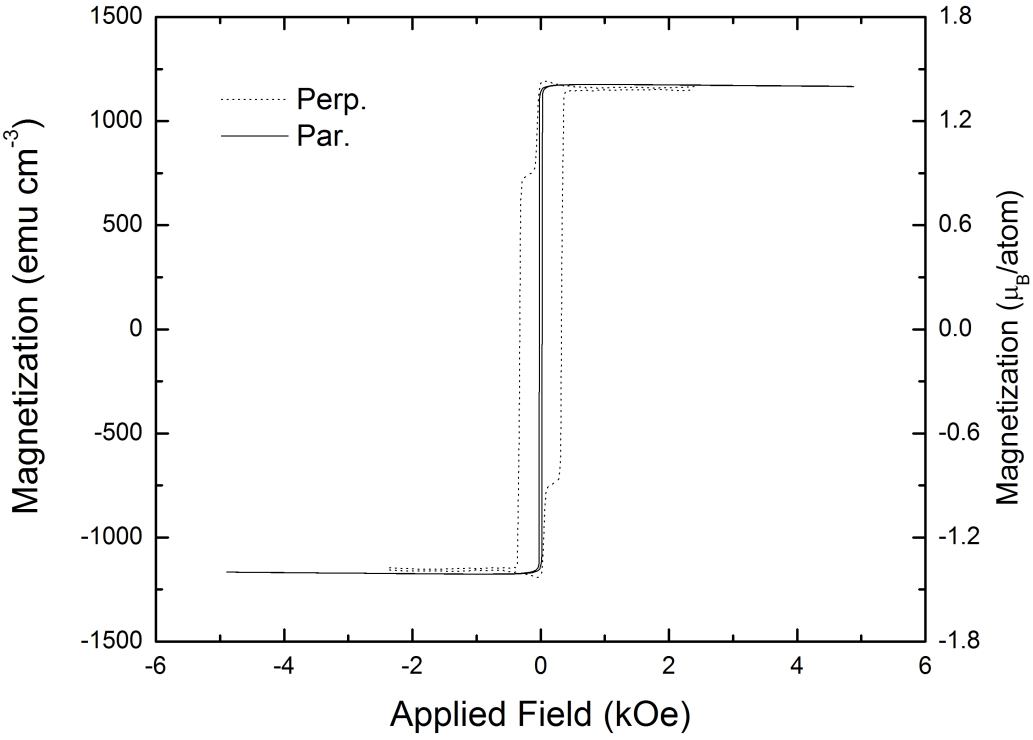

Figure 3.4: VSM measurement of first dual-source Co-Cr thin film, showing excellent squareness. The hysteresis loop suggests the presence of two magnetic phases of different compositions.

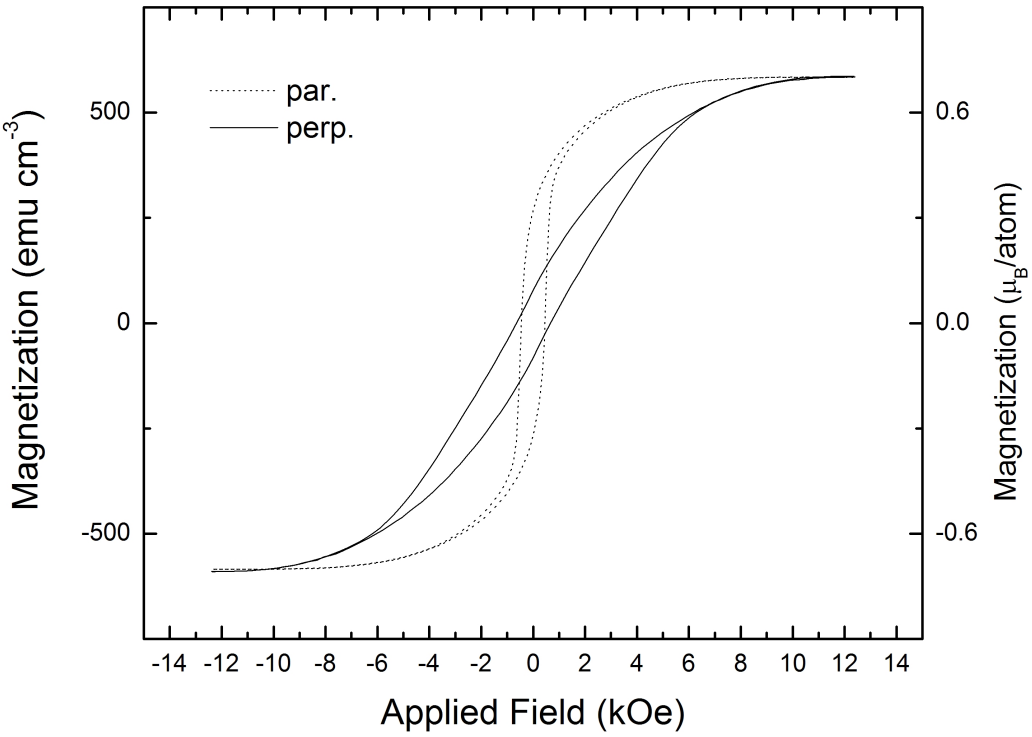

Figure 3.5: VSM measurement of second dual-source Co-Cr thin film, showing poor squareness out of plane.

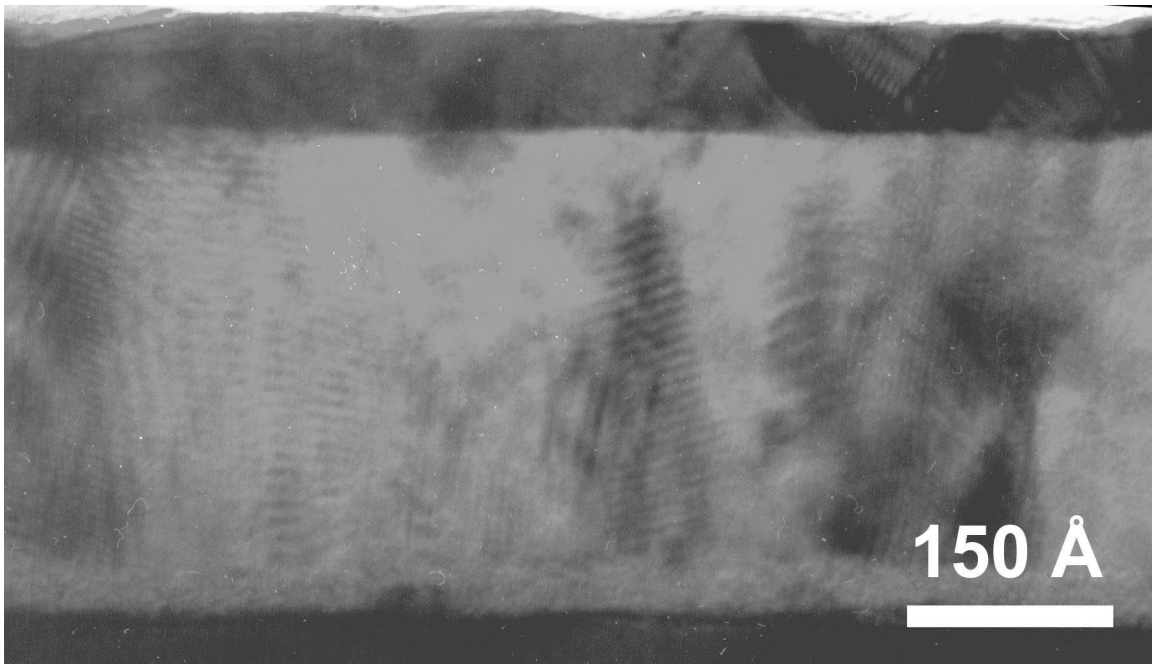

Figure 3.6: Cross-sectional electromicrograph of Co-Cr thin film grown by PLD taken with a Philips EM430 microscope operating at 300 kV. Capping layer is Au. Substrate material is GaO_x/(Al,Ga)As.

3.3 Pulsed Laser Deposition of Co-Cr Thin Films

The next method which was examined as a means of fabricating Co-Cr perpendicular magnets was PLD. Pulsed laser deposition of metals is qualitatively different than that of ceramics such as iron oxide. No electronic sputtering occurs because of the abundance of free carriers. In fact, the primary mechanism of laser-target interaction is free carrier absorption, and the primary cause of ablation is thermal sputtering [15].

A PLD target of composition $x_{\mathrm{Cr}} = 0.22$ was obtained and ablated onto a substrate of GaO_x/(Al,Ga)As for potential examination as a spin injection structure (Ch. 4). The same laser parameters were used as for the laser ablation of iron oxide (Sec. 2.2.1). For compatibility with prior EBE experiments $T_{\mathrm{sub}} = 190°\mathrm{C}$. The film deposited is shown by cross-sectional transmission electron microscopy (TEM) in Fig. 3.6.

TEM analysis revealed two aspects of Co-Cr PLD. The EDAX energy dispersive x-ray fluorescence spectroscopy unit mounted on the electron microscope measured the composition of the as-deposited film as being remarkably identical to that of

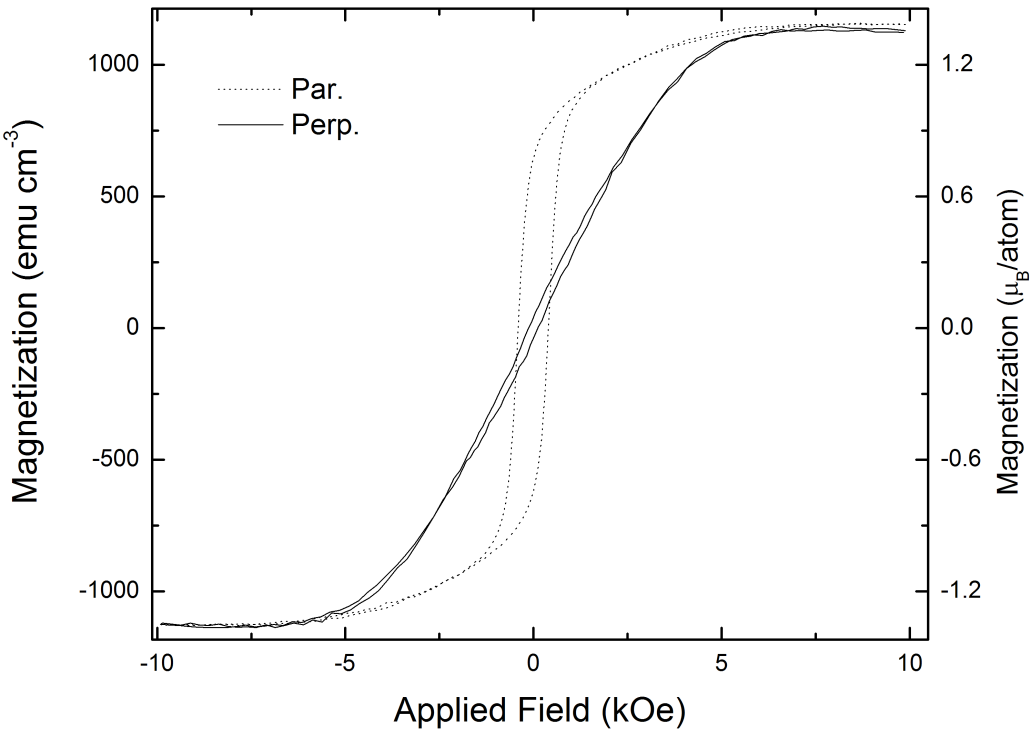

Figure 3.7: M vs. H curves for Co-Cr film grown by PLD. The out-of-plane magnetic properties are poor.

the target, namely 22 at.% Cr, 78 at.% Co, with an error less than 0.5 at.%. This is further evidence of the superb stoichiometric nature of PLD films. However, by measuring the electromicrograph of the Co-Cr layer, the growth rate was found to be 0.06 Å/s, which is extremely slow. Given that the repetition rate was 10 pulses/s, this is very similar to the Co ablation rates reported by Kools [15]. This growth rate is apparently not amenable to the formation of columnar grains and thus will not form the perpendicularly magnetizing microstrucutre, as confirmed in Fig. 3.7.

Vibrating sample magnetometry data for this sample found that the perpendicular magnetization was very poor. The out-of-plane squareness ratio was only 0.0340, compared to 0.5504 for the in-plane squareness. The perpendicular coercivity was only 119.49 Oe. With these results it was decided to pursue other avenues of perpendicular

magnet fabrication.

3.4 Single-Source Deposition of Co-Cr Thin Films

3.4.1 Thermodynamic Predictions of Evaporation Behavior

A physical metallurgy-driven solution to the problem of reproducible alloy films was attempted. Because PLD is a nonequilibrium process, it is not necessary to consider the equilibrium between the vapor and the condensed states. By contrast EBE operates by exploiting this equilibrium. At a given temperature the difference in vapor pressure between two elements can be orders of magnitude. The field of surface coatings has developed processes which account for this phenomenon. Metzner and Scheffel studied the effect of nonideal mixing and vapor pressure difference for stainless steel (Fe-Cr-Ni) alloys [16].

The EBE system as examined by Metzner and Scheffel consists of four phases: The solid source, liquid melt, evaporant, and depositing film. Conservation of mass requires that with steady-state heat input the system should after some time achieve an equilibrium where all four phases have the same composition. The material evaporated must equal the material melted. Nonetheless there is a finite time during which the difference in vapor pressure will dictate that the evaporant has a different composition than the melt. It is found that this "transient time" in the case of transition metal alloys is on the order of hours, far longer than is necessary to deposit the thin optical windows that are the goal of this work.

The evaporation rate at the surface for element i is

$$r_i(T) = A_i b a_i(T, x_i) p_i(T) \sqrt{\frac{\mathcal{M}_i}{T}} \tag{3.12}$$

where A_i is a unitless "evaporation coefficient," b is a constant and equal to 0.05866 $\mathrm{g}^{1/2}\ \mathrm{torr}^{-1}\ \mathrm{cm}^{-2}\ \mathrm{mol}^{1/2}\ \mathrm{K}^{1/2}\ \mathrm{s}^{-1}$, p_i is the vapor pressure of i, $\mathcal{M}_i$ the atomic mass of i, and T is the surface temperature of the evaporating phase. a_i is the activity of i in the evaporating phase, equal to the product of the activity coefficient and

atomic fraction: $a_i = \gamma_i x_i$. The combined pressure of evaporant is

$$P = \sum_i a_i p_i = \sum_i \gamma_i x_i p_i \tag{3.13}$$

Metzner and Scheffel use the form $p(T) = K_1 \exp(-K_2/T)$ for vapor pressure. For consistency and simplicity this form was retained in this work. For Cr they give $K_1^{\mathrm{Cr}} = 7.748 \times 10^9$ torr and $K_2^{\mathrm{Cr}} = 45771$ K. Vapor pressure data for Co was obtained [17] and fit to this representation with ORIGINPRO's Advanced Fitting Tool. This yielded $K_1^{\mathrm{Co}} = 3.50537 \times 10^9$ torr and $K_2^{\mathrm{Co}} = 47593$ K.

If the activity coefficient and vapor pressure are known, Eq. 3.12 forms a basis for design of alloy targets for single-source evaporation. Since the vapor pressure of Cr is so very large with respect to that of Co, it was believed that successful deposition of a film having the desired composition (Cr atom fraction ~ 0.22) might result without melting the source. This was the basis of the narrow choice of temperature range for determination of activity coefficients (see Appendix A). Over the range 1027°C to 1157°C, the following equations were found to fit the activity coefficient data well:

$$\begin{aligned}
&\gamma_{\mathrm{Co}}(T, x_{\mathrm{Cr}}) = \\
&\quad (3.9776 \times 10^{-8} + 1.0460 \times 10^{-8} x_{\mathrm{Cr}} - 1.8676 \times 10^{-8} x_{\mathrm{Cr}}^2)(-3.2443 \times 10^{-8} \\
&\quad +744250T - 528.23T^2 + 0.12495T^3)
\end{aligned} \tag{3.14}$$

$$\begin{aligned}
&\gamma_{\mathrm{Cr}}(T, x_{\mathrm{Cr}}) = \\
&\quad @3.6334 \times 10^{-8} - 1.0211 \times 10^{-7} x_{\mathrm{Cr}} + 2.2717 \times 10^{-7} x_{\mathrm{Cr}}^2)(-2.7249 \times 10^{-8} \\
&\quad +718630T - 549.79T^2 + 0.13749T^3)
\end{aligned} \tag{3.15}$$

where T is in Kelvin.

The values of evaporation rate r_i are by themselves of little interest. It is the ratio of deposition rates that indicates the relative amounts of Co and Cr in the depositing film. Assuming that evaporation coefficients are roughly equal ($A_{\mathrm{Co}} \approx A_{\mathrm{Cr}}$) the deposition ratio approximation is

$$D^{\text{low}}(T, x_{\text{Cr}}) \equiv \frac{r_{\text{Co}}(T, x_{\text{Cr}})}{r_{\text{Cr}}(T, x_{\text{Cr}})} \simeq \frac{(1 - x_{\text{Cr}})}{x_{\text{Cr}}} \frac{\gamma_{\text{Co}}(T, x_{\text{Cr}})}{\gamma_{\text{Cr}}(T, x_{\text{Cr}})} \frac{p_{\text{Co}}(T, x_{\text{Cr}})}{p_{\text{Cr}}(T, x_{\text{Cr}})} \tag{3.16}$$

Again, it is important to note that x_{Cr} is the atomic fraction of Cr in the source, *not* the depositing film. The atomic fraction of Cr in the depositing film, denoted as y_{Cr}, is equal to

$$y_{\text{Cr}}^{\text{low}}(T, x_{\text{Cr}}) = \frac{1}{1 + D^{\text{low}}(T, x_{\text{Cr}})} \tag{3.17}$$

Preliminary investigation of Eq. 3.17 yielded surprising results. It was found that "low" EBE temperatures with even small concentrations of Cr led to very large pressures. For example, at $T = 1400$ K and $x_{\text{Cr}} = 0.1$, $y_{\text{Cr}} = 0.80$ is predicted (Eq. 3.17) with a resulting beam pressure of $P = 1.1$ torr (Eq. 3.13). It was unknown if this is a physically real result, *i.e.*, if beam equivalent pressures in EBE are actually that large, or if actual deposition temperatures were much lower. Since the chamber pressure had not historically exceeded 10^{-6} torr during deposition, the former was cast into doubt. Even though the pressure in the metal vapor flux should be large, it is striking that it could be several orders of magnitude larger than the background pressure in the chamber. Simultaneously solving Eqs. 3.13 and 3.17 for a more desirable parameter set yields unrealistically low temperatures. For example, numerically solving for $P = 10^{-5}$ torr and $y_{\text{Cr}}^{\text{low}} = 0.22$ yields $T = 636°\text{C}$ and $x_{\text{Cr}} = 5.4 \times 10^{-4}$. Not only is this well outside the fitting range for the activity coefficients, it is unlikely that the deposition rate associated with temperatures that low would be measurable with a QCM or if the blackbody radiation emitted by the source would be visible.

Considering the case of evaporation at even higher temperatures, the liquidus temperature of Co-Cr reaches a maximum of 1768 K [18] at the pure Co end of the phase diagram and decreases as x_{Cr} increases. In the pure liquid phase, the solution is ideal, since there neither element has a structure as such, so $\gamma_i = 1$. The difference between solidus and liquidus temperatures is small, which makes the probability deposition would occur in this region negligibly small. A simplification of Eq. 3.16 to reflect this case yields

$$D^{\text{high}}(T, x_{\text{Cr}}) \equiv \frac{r_{\text{Co}}(T, x_{\text{Cr}})}{r_{\text{Cr}}(T, x_{\text{Cr}})} \simeq \frac{(1 - x_{\text{Cr}})}{x_{\text{Cr}}} \frac{p_{\text{Co}}(T, x_{\text{Cr}})}{p_{\text{Cr}}(T, x_{\text{Cr}})} \tag{3.18}$$

and

$$\begin{aligned} y_{\text{Cr}}^{\text{high}}(T, x_{\text{Cr}}) &= \frac{1}{1 + D^{\text{high}}(T, x_{\text{Cr}})} \\ &= \frac{x_{\text{Cr}}}{x_{\text{Cr}} + 0.72601(1 - x_{\text{Cr}}) \exp((-42388\,\text{K})/T)} \end{aligned} \tag{3.19}$$

3.4.2 Experimental Analysis of Single-Source Co-Cr Films

In order to test the method, a custom source of Co-2Cr (2.00 weight percent Cr, $x_{\text{Cr}} = 0.0177$) was fabricated by Plasmaterials, Inc., of Livermore, Calif., by arc melting and introduced into our system. Evaporation was performed at $T_{\text{sub}} = 190°\text{C}$ on a clean silicon wafer. The chemistry of the films was determined externally at Charles Evans and Associates (CEA) of Sunnyvale, Calif., using Rutherford backscattering spectroscopy (RBS); magnetization was measured by VSM as before (Sec. 2.3.5).

Rutherford backscattering spectroscopy is based on the Rutherford scattering of high-energy (1-4 MeV) positively charged particles, *e.g.*, ^{4}He nuclei (alpha particles), accelerated toward the sample of interest. Most of these particles are implanted into the sample, but some will collide with atoms in the sample and be backscattered by Coulombic repulsion. The energy of the backscattered atoms will be characteristic of the atomic number of the impinged atom Z and the backscattering angle. We define m_1 as the mass of the projectile atom, m_2 as the mass of the target atom, θ as the scattering angle (*e.g.*, 160° in Fig. 3.8), and K_{m_2} as the kinematic ratio , finding [19]:

$$K_{m_2} = \left(\frac{\sqrt{m_2^2 - m_1^2 \sin^2 \theta} + m_1 \cos \theta}{m_2 + m_1} \right)^2 \tag{3.20}$$

Thus, for a target atom of ^{59}Co ($m_2 = 59$), ^{4}He as a projectile ($m_1 = 4$), scattering angle $\theta = 160°$, and $E_{\text{incident}} = 2.275$ MeV, the energy of the backscattered atom is 1.748 MeV. This energy is characteristic and associated with the atoms of that isotope

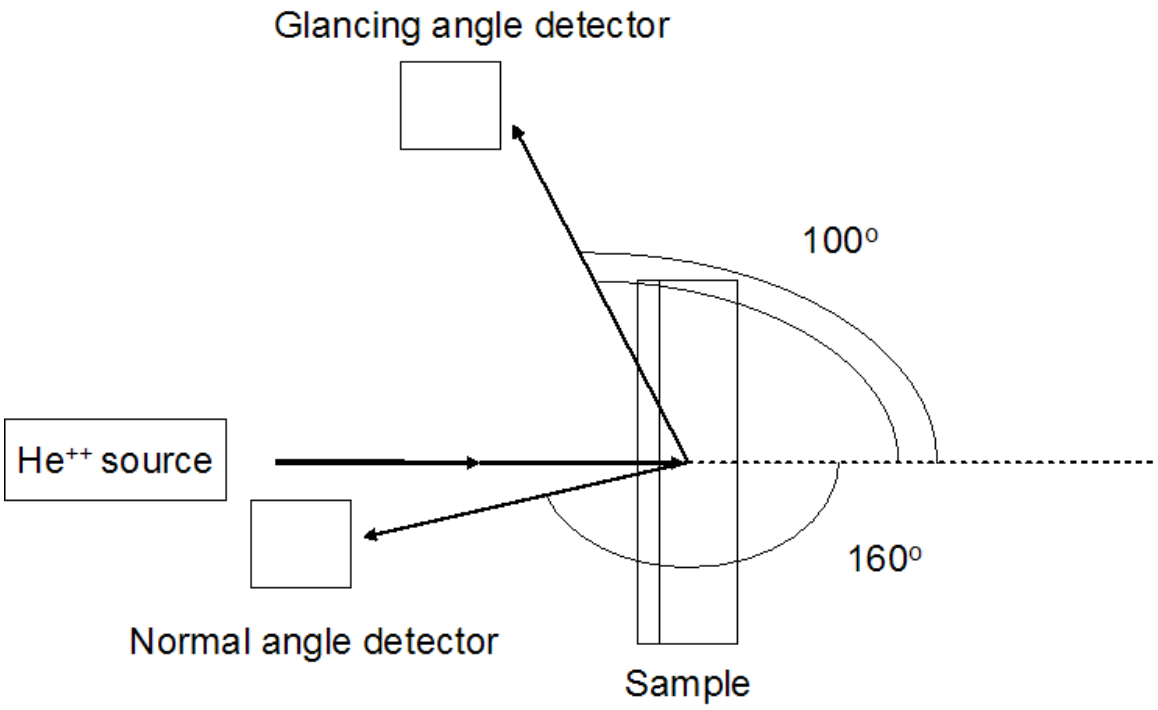

Figure 3.8: Configuration of CEA RBS system. The sample is perpendicular to the incoming 2.275-MeV $^4He^{2+}$ beam.

closest to the detector. Thus the presence of the element is identifiable by the most energetic signal which it produces. Projectile atoms backscattered by target atoms deeper in the sample will experience inelastic processes which reduce their kinetic energy. The spread in energy owed to this attenuation is given by

$$\Delta E = [\epsilon] N w \tag{3.21}$$

where w is the thickness of the region in the sample containing the appropriate element and N is the atomic density (units of 1/volume). The quantity $[\epsilon]$ is the effective stopping cross-section; literature compilations of these quantities exist. Thus, from the spread in the RBS spectrum, the thickness of the material is measurable.

The signal intensity for normal projectile incidence to first order is

$$I \simeq \sigma(E) \Omega Q N w \tag{3.22}$$

Here $\sigma(E)$ is the cross-section of the target atom as a function of the energy of the projectile atom incident upon it (which may be attenuated by passage through the sample), Q is the total charge of the incident projectile atoms, and Ω is the solid angle of the sphere centered upon the target atom that is subtended by the detector channel which collects backscattered atoms with energy in the neighborhood of E. See Ref. [19] for an exhaustive discussion of RBS signal analysis. Data analysis is performed by constructing a theoretical prediction for the experimental curve and adjusting the concentration and depth parameters in the theoretical curve to fit the experimental data.

It is also important to note that the units of the abscissa of these plots is given as "channels." This refers to the physical channels of the instrument detector. These channels are correlated to the backscattered particle energy in an instrument-specific manner which must be calibrated before measurement.

Fit of the RBS spectrum in 3.9 by CEA found that for the as-deposited Co-Cr layer in Fig. 3.9, $y_{\mathrm{Cr}} = 0.057$. Solving Eqs. 3.17 and 3.19 for this case ($x_{\mathrm{Cr}} = 0.0177$ and $y_{\mathrm{Cr}} = 0.057$) yields deposition temperatures of 4479 K and 3832 K respectively. Clearly these are not physical results. The magnetization is shown in Fig. 3.10.

From the chemical and magnetic data the necessity of higher Cr content in the sources was obvious. Custom sources were obtained at compositions Co-6Cr and Co-14Cr and used for deposition.

The deposition of these materials proved challenging. Melting the source occasionally resulted in such violent bubbling that one source even escaped from the crucible. (It is possible this was the result of minute amounts of air trapped between the source and crucible liner.) Even before this threshold was reached the ejection of high-velocity fragments ("spitting") would occur. The protocol for these depositions which developed as a result was to shutter the substrate, heat the source into the "spitting" regime, reduce the power incrementally until it ceased, hold the source at that level until the deposition rate as seen by the QCM stabilized, and finally open the shutter to begin deposition.

The substrate temperature was also varied for some of these depositions. Even

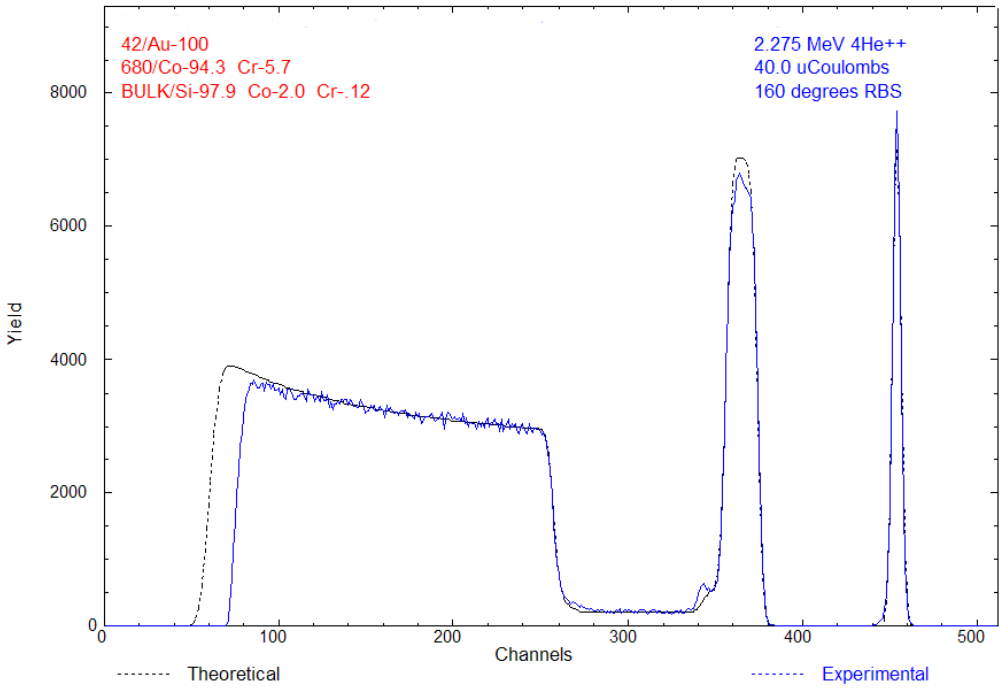

Figure 3.9: Rutherford backscattering spectrum of Au/Co-Cr/Si sample. Cobalt-chromium layer deposited by single-source EBE from Co-2Cr source material.

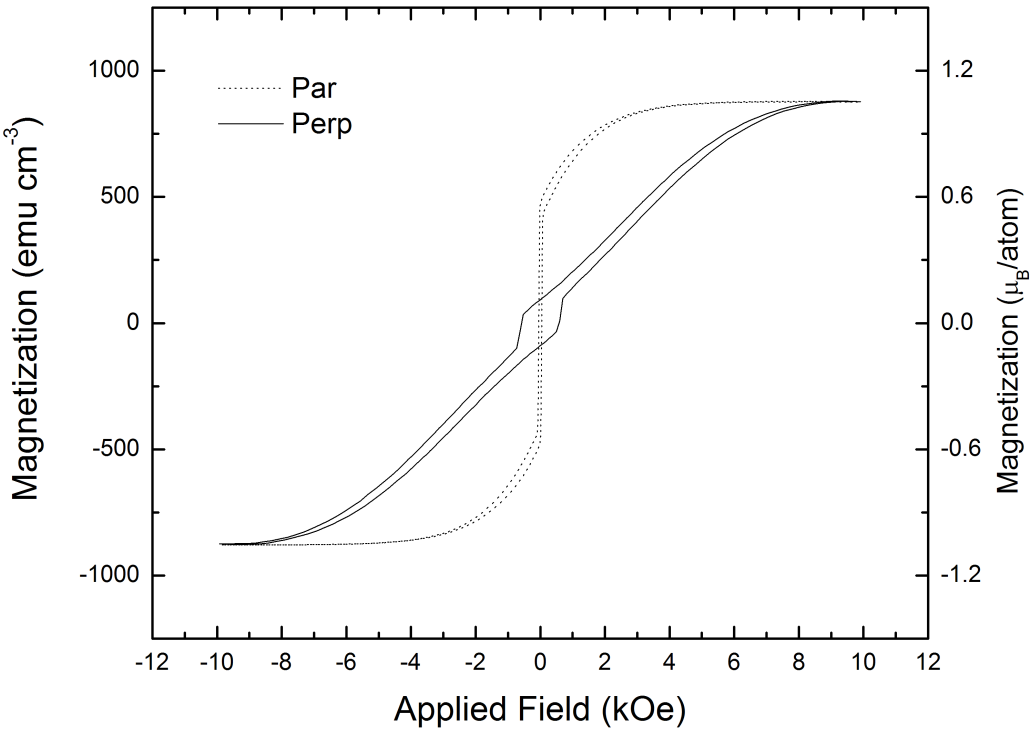

Figure 3.10: Magnetization of Co-Cr layer grown from Co-2Cr source.

Source Material	Co-2Cr	Co-6Cr	Co-6Cr	Co-14Cr
$T_{\text{sub}}(^{\circ}C)$	190	20	190	20
Atomic fraction Cr	0.057	0.167	0.196	0.343
Squareness, H in plane	0.52939	0.81055	-	-
Squareness, H out of plane	0.10379	0.48846	-	.12696
Coercivity, H in plane (Oe)	46.12	47.79	-	-
Coercivity, H out of plane (Oe)	578.18	264.83	-	7.0044

Table 3.2: Summary of magnetic and chemical properties of single-source EBE Co-Cr thin films.

though 190° is a low temperature in metallurgical terms, room temperature should reduce the surface mobility of adatoms even further. The parameter which normally determines as-deposited grain size is the homologous temperature $T_H = T_{\text{sub}}/T_{\text{melt,film}}$. For these Co-Cr alloys, the solidus temperature is 1700-1770 K, so at $T_{\text{sub}} = 190°\text{C}$, $T_H \simeq 0.27$; at room temperature, $T_H = 0.17$. While both of these temperatures reside in what Ohring refers to as "Zone I" [20], the lower temperature enhances the behavior of this zone: Deposition dominated by *shadowing* effects as opposed to surface or bulk diffusion. The behavior is described as shadowing because as columns grow, they obfuscate the substrate from the evaporant and thus promote their own growth. The lower temperature should also increase the sticking coefficient and the deposition rate as a result.

Tests were performed with the Co-6Cr source at room temperature and at $T_{\text{sub}} = 190°\text{C}$. The RBS spectra which resulted are shown in Figs. 3.11 and 3.12.

The models of Sec. 3.4.1 were unable to calculate an evaporation temperature. However the perpendicular magnetization was definitely improved by room-temperature deposition, as summarized in Table 3.2.

Finally deposition was performed using the Co-14Cr source with the substrate at room temperature. This yielded a very high Cr concentration (Figs. 3.15). Figure 3.16 shows the magnetization behavior. The small sample volume complicates the analysis, but no permanent moment was found.

The important properties of the single-source EBE thin films are given in Table 3.2.

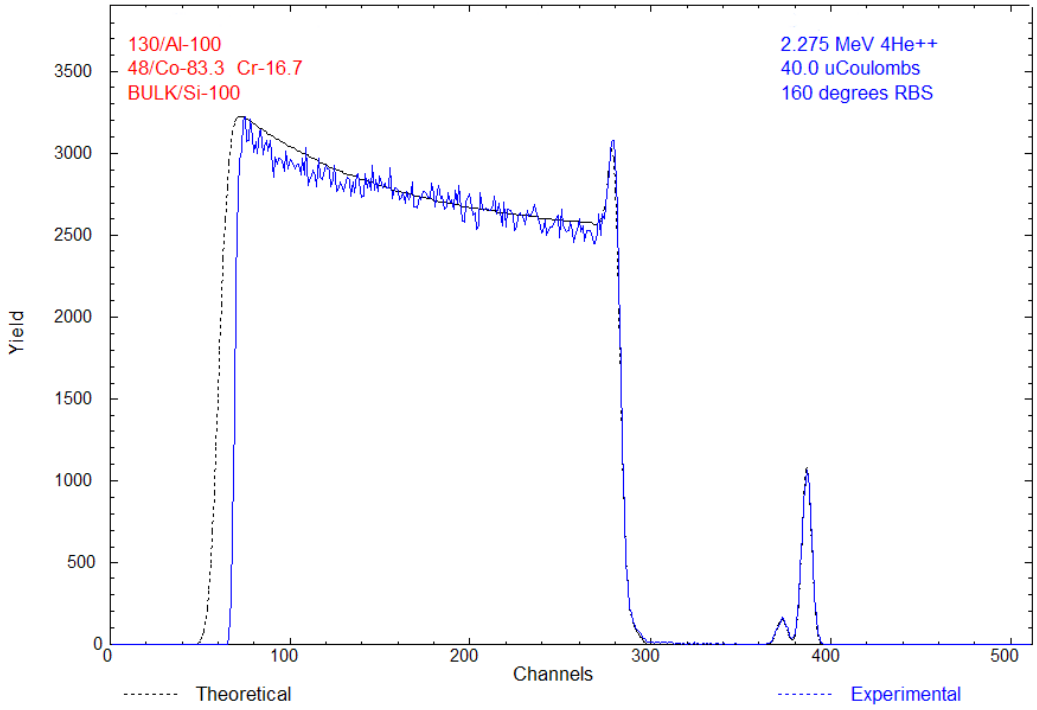

Figure 3.11: Rutherford backscattering spectrum of Al/Co-Cr/Si sample. Cobalt-chromium deposited by single-source EBE using Co-6Cr source material. $T_{\text{sub}} = 20°\text{C}$. As-deposited composition is 16.7 at.% Cr, balance Co.

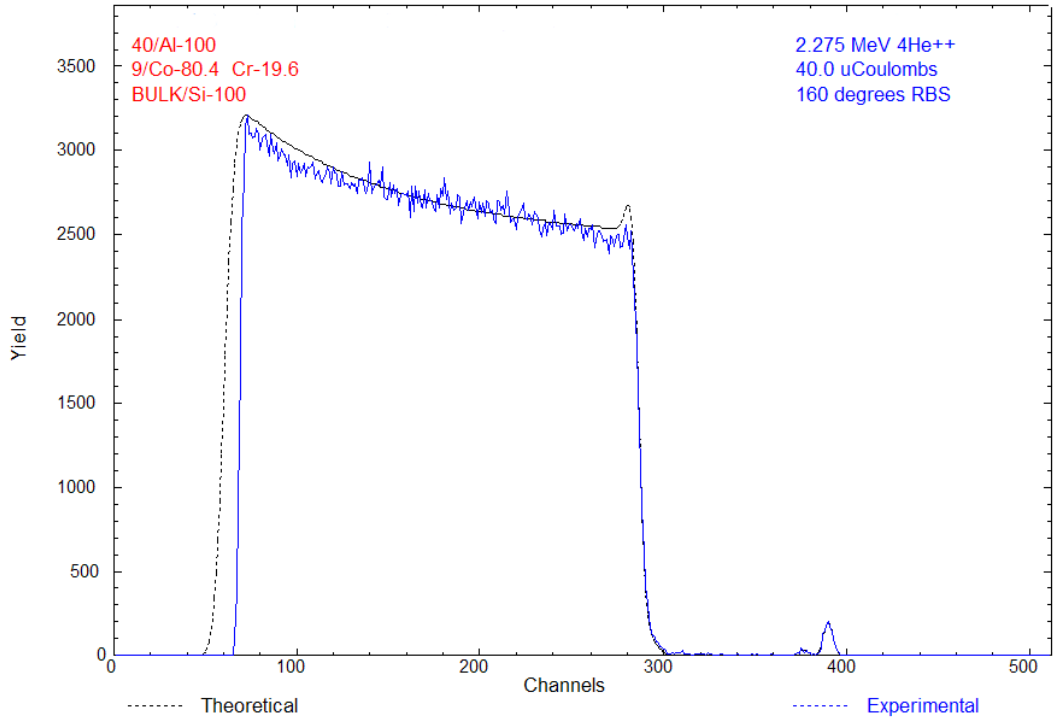

Figure 3.12: RBS spectrum of single-source EBE sample, Co-6Cr source, $T_{\text{sub}} = 190°\text{C}$. As-deposited composition is 19.6 at.% Cr, balance Co.

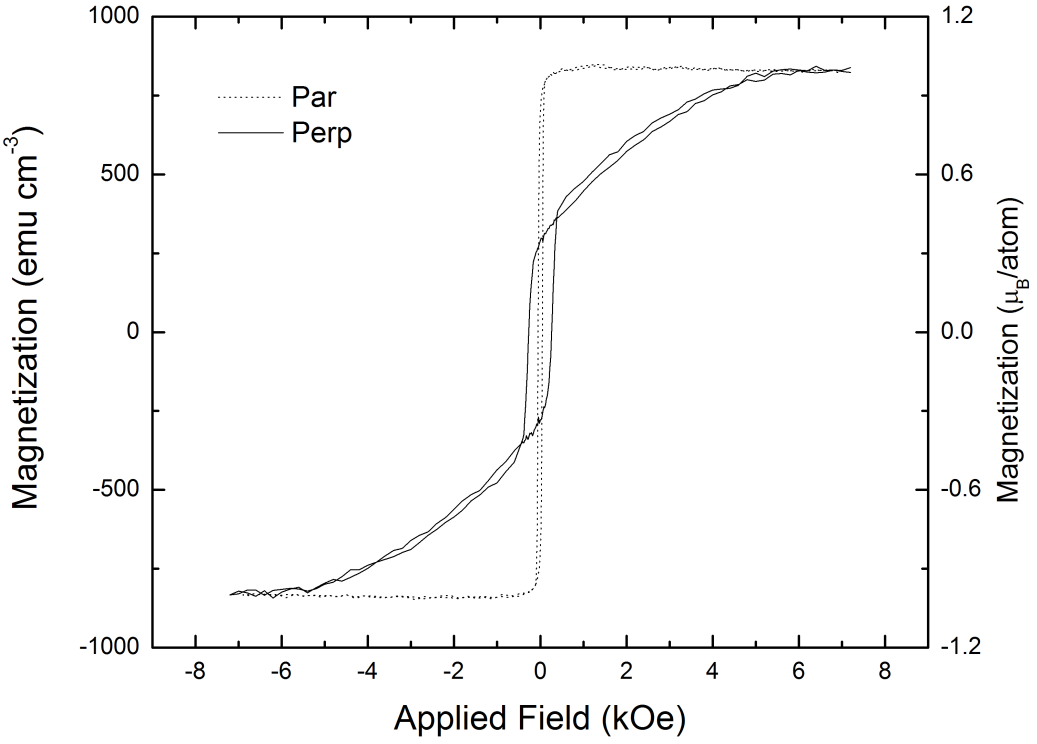

Figure 3.13: Magnetization of Co-Cr layer grown from Co-6Cr source. $T_{\text{sub}} = 20°\text{C}$.

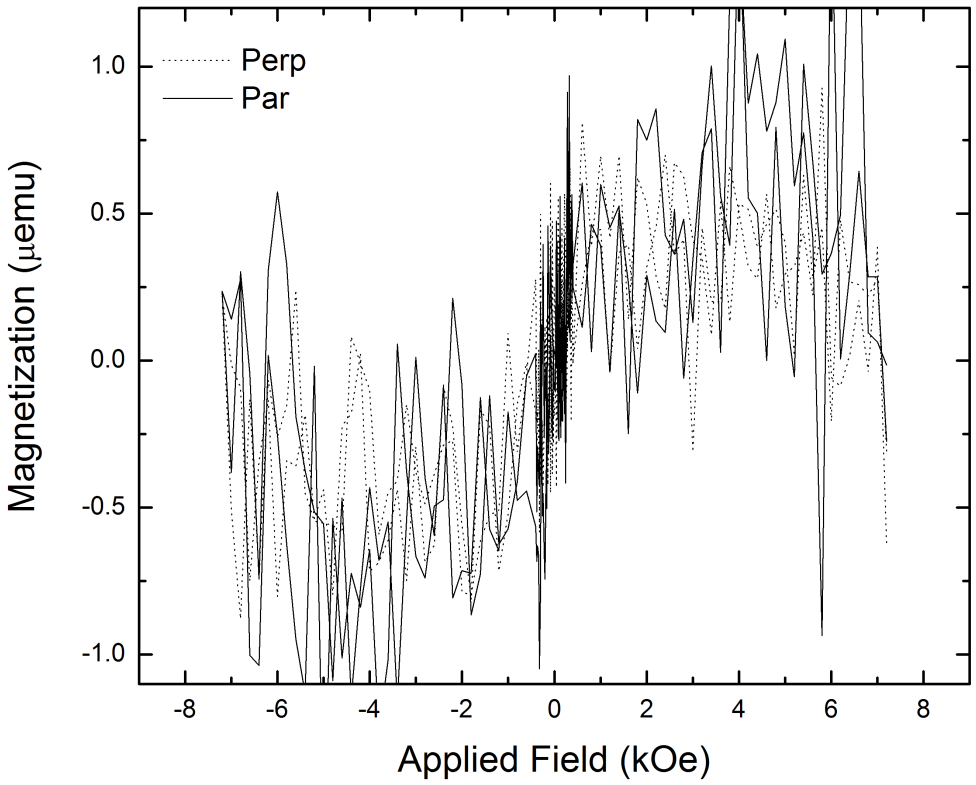

Figure 3.14: Magnetization of Co-Cr layer grown from Co-6Cr source. $T_{\text{sub}} = 190°\text{C}$. Magnetization not observed perhaps due to small volume.

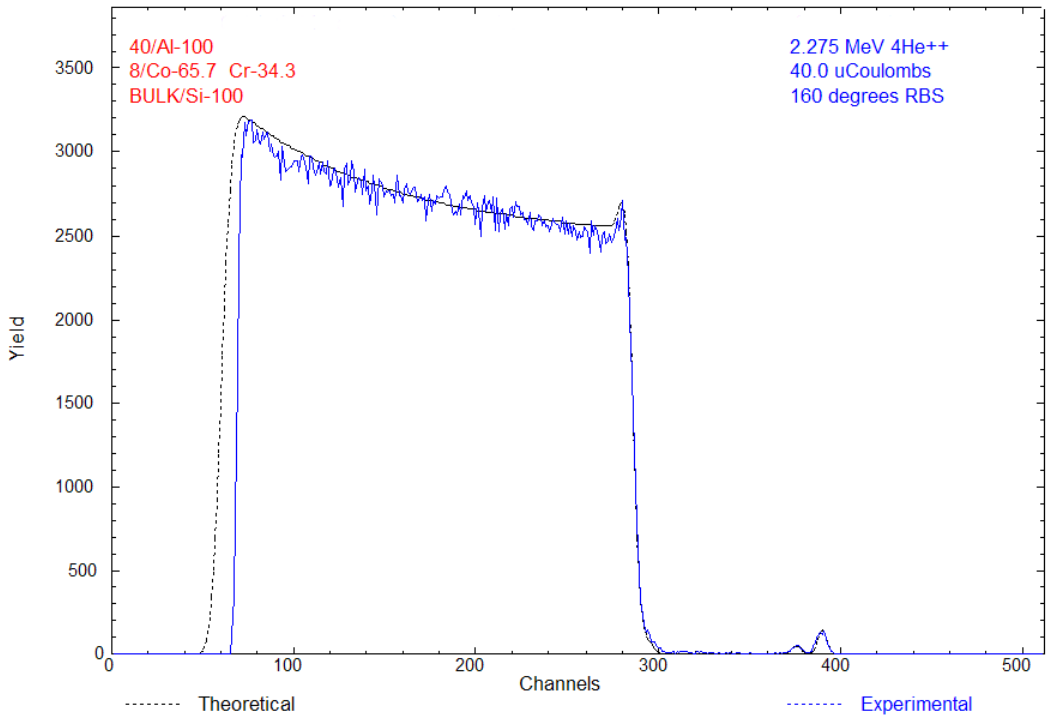

Figure 3.15: RBS spectrum of single-source EBE sample, Co-14Cr source, $T_{\text{sub}} = 190°\text{C}$. As-deposited composition is 34.3 at.% Cr, balance Co.

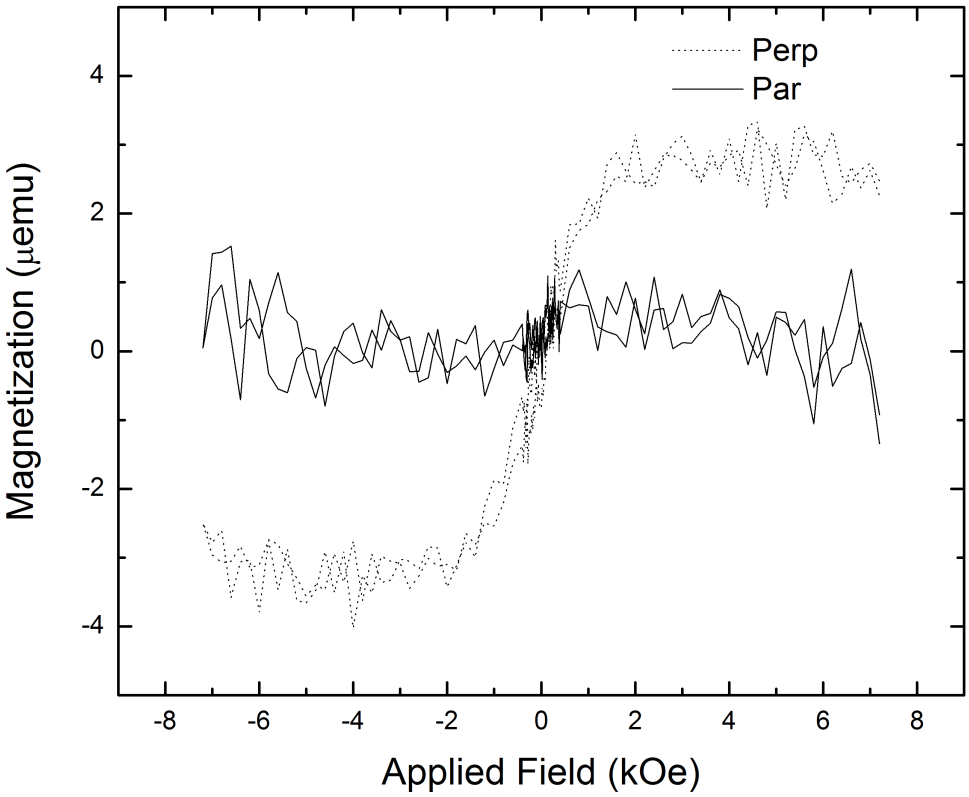

Figure 3.16: Magnetization of Co-Cr layer grown from Co-14Cr source. $T_{\text{sub}} = 20°\text{C}$. Very little if any permanent magnetic moment.

3.5 Discussion

The failure of the model proposed by Metzner and Scheffel to predict the composition of the as-deposited Co-Cr films must be examined in terms of the difference between the two deposition systems. Most significantly, their sources are considerably larger (500 cm^3 [16] versus 2.2 cm^3) and the beam spot is a much smaller fraction of the crucible area. Additionally, fresh alloy is continuously fed into the crucible during evaporation. This acts as a heat sink and promotes thermal stability because the solid-liquid interface does not move. In our system however the solid-liquid interface continually moves into the solid since there is always a net mass loss. The result of this is that the crucible heat capacity decreases somewhat during deposition and, since the heat input is constant, the deposition temperature slowly rises during evaporation. Essentially the transition time is infinite and the system can never attain equilibrium. An experimental means of determining the evaporation temperature, such as a high-temperature optical pyrometer, would aid considerably in the elucidation of our "small-crucible" process. Other attempts to numerically solve the deposition ratio for different forms of the vapor pressures as well as non-unity ratios of evaporation coefficients ($A_{\mathrm{Co}}/A_{\mathrm{Cr}}$) did not yield realistic deposition temperature numbers. The ratio of evaporation coefficients is not likely to deviate considerably from unity since the heat capacities of Co and Cr are very similar.

Thus it is believed that the model may only relate in a qualitative manner to our system. However it did predict that to obtain a specific chromium concentration y_{Cr} in a film, the chromium fraction in the source x_{Cr} must be considerably smaller. It is observed from the RBS fits in Table 3.2 that x_{Cr} should be roughly a third of the desired film composition y_{Cr}. Since the Co-Cr films must be thin enough (100-200 Å) to be transparent at the wavelength of the quantum well in Fig. 1.3, the thermal stability of deposition is not as critical as it would be for a thicker film, as long as the same procedure is followed for each deposition, and so we believe the process to be repeatable.

The model derived here for deposition using multiple QCMs for control, which

may be expanded to arbitrarily large numbers of sources and monitors by adding terms to Eq. 3.4, is universally valid and a useful tool for multicomponent physical vapor deposition.

Finally, growth from the Co-6Cr source with the substrate at room temperature yields an improved perpendicular coercivity and squareness. A large perpendicular coercive field is desired for the perpendicular magnetic recording industry, with $H_{c,\perp}$ as large as 1500 Oe reported in the literature [9] and would be useful for a spin polarizing contact, enabling it to behave as a hard magnet. The more important parameter is the out-of-plane squareness ratio, which is seen to improve to nearly 0.5 in our best result. If these layers are to serve as "portable" spin injection contacts, the retentivity is critical for efficient injection. Slightly higher concentrations of Cr in the source (Co-8Cr, perhaps) may allow deposition of films near the optimal 20-24 at.% Cr composition.

Bibliography

[1] S. R. Ichiriu, X. Cartoixà, and T. C. McGill (unpublished).

[2] V. F. Motsnyi, J. De Boeck, J. Das, W. Van Roy, G. Borghs, E. Goovaerts, and V. I. Safarov, Appl. Phys. Lett. **81**, 265 (2002).

[3] J. Strand, B. D. Schultz, A. F. Isakovic, C. J. Palmstrøm, and P. A. Crowell, Phys. Rev. Lett. **91**, 036602 (2003).

[4] A. T. Hanbicki, B. T. Jonker, G. Itskos, G. Kioseoglou, and A. Petrou, Appl. Phys. Lett. **80**, 1240 (2002).

[5] R. C. O'Handley, *Modern Magnetic Materials: Principles and Applications*, 1st ed. (Wiley-Interscience, New York, 2000).

[6] S. Iwasaki and H. Yamazaki, Co-Cr Sputtered Films of Perpendicular Magnetic Anisotropy, 7th Annual Conference on Magnetics, Japan, 1975.

[7] Y. Maeda, M. Asahi, and M. Seki, Jpn. J. Appl. Phys. **25**, L668 (1986).

[8] S. Yamamoto, H. Wada, H. Kurisu, and M. Matsuura, J. Magn. Magn. Mater. **235**, 133 (2001).

[9] J. C. Lodder, T. Wielinga, and J. Worst, Thin Solid Films **101**, 61 (1983).

[10] P. J. Grundy and M. Ali, J. Magn. Magn. Mater. **40**, 154 (1983).

[11] T. M. Coughlin, J. H. Judy, and E. R. Wuori, IEEE T. Magn. **17**, 3169 (1981).

[12] R. Sugita, T. Kunieda, and F. Kobayashi, IEEE T. Magn. **17**, 3172 (1981).

[13] J. C. Lodder, J. Magn. Magn. Mater **159**, 238 (1996).

[14] C.-S. Lu, J. Vac. Sci. Technol. **12**, 578 (1975).

[15] J. C. S. Kools, in *Pulsed Laser Deposition of Thin Films*, edited by D. B. Chrisey and G. K. Hubler (Wiley-Interscience, New York, 1994), pp. 456–457.

[16] C. Metzner and B. Scheffel, Surf. Coat. Tech. **146**, 491 (2001).

[17] http://www.veeco.com/learning/learning_vaporelements.asp, Veeco Instruments, May 4, 2004.

[18] *Binary Phase Alloy Diagrams*, edited by T. B. Massalski (ASM International, Materials Park, Ohio, 1990), Vol. 2, p. 1180.

[19] W.-K. Chu, J. W. Mayer, and M.-A. Nicolet, *Backscattering Spectrometry* (Academic Press, New York, 1978).

[20] M. Ohring, *The Materials Science of Thin Films* (Academic Press, San Diego, 1992), pp. 223–232.

Chapter 4

Deposition and Characterization of Gallium Oxide Ultrathin Films

4.1 Motivation

Research into thin-film gallia and the related material $(Ga,Gd)_2O_3$ has been steady for several decades [1]. Interest in fabricating gallium arsenide MOSFETs has compelled research into use of Ga_2O_3 as the gate dielectric in such devices (Fig. 1.1) and while such efforts have not yet resulted in a commercial device a large body of knowledge has been acquired regarding the properties of Ga_2O_3 on semiconductors.Hong *et al.* claim an interfacial density of states $\sim 5 \times 10^{10}$ eV^{-1} cm^{-2} for $(Ga,Gd)O_x$ insulator layers on GaAs; this would be comparable to commercial SiO_2/Si interfaces. Recently gallium nitride MOSFETs have been envisioned as an application for gallium oxide as well [2].

A superior interface would be useful for spin injection as well. Section 1.4.1 reviews the consensus that tunnel barriers between ferromagnets and semiconductors are of considerable utility in efficient injection of spin-polarized currents. The direct motivation for our study of Ga_2O_3 was the work of Li *et al.* who found superior junction magnetoresistance (JMR) in a Co/Ga_2O_3/permalloy structure compared to junctions made with Al_2O_3 [3]. Specifically the room temperature JMR was significant (18.2%) with an ultrathin gallium oxide film, approximately 13-14 Å thick.

Note in this work that the term "GaO_x" always refers to an underoxidized amor-

Sample	Growth Temperature (°C)	Final Reconstruction
I	575	$c(4\times4)$
II	550	(2×4)

Table 4.1: Epitaxial GaAs buffer layers.

phous thin film of gallium oxide, where as "Ga_2O_3" refers to the crystalline stoichiometric form. The term "gallium sesquioxide" is encountered in the literature for Ga_2O_3 but is not used here.

4.2 Experimental Methods

4.2.1 Substrate Preparation

For this work, GaAs(001) wafers were indium-bonded to molybdenum blocks for molecular-beam epitaxy (MBE) growth and outgassed in ultrahigh vacuum (UHV) before growth of epitaxial layers. Growth was performed in an excess flux of As_2 as for substrates grown to study Fe_3O_4 epitaxy (Sec. 2.2.2). It was desired to study the effect of reconstruction and thus arsenic concentration upon subsequent gallium oxide deposition, so two sets of growths were performed, as summarized in Table 4.1. The samples were also doped with beryllium to an acceptor concentration of 3×10^{18} cm^{-3} in anticipation of observing electroluminescence from electron-hole pair recombination from the region below the oxide film. This level of doping should not impact the chemical analysis below; beryllium peaks were not observable in x-ray photoelectron spectra.

The fact that Sample II was removed from the arsenic flux earlier (upon cooling through 450°C) contributed to a lower arsenic concentration. This was actually measured using x-ray photoelectron spectroscopy before further work was performed.

The data shown in Table 4.2 that in the sample volume measured by XPS (approximately the topmost 50 Å of a given sample) that there is slightly more arsenic in the case of Sample I, perhaps representing no more than the fact that the final

	Sample I		Sample II	
	Mg Kα	Al Kα	Mg Kα	Al Kα
I_{Ga}	29672	8889	42749	10133
FWHM (eV)	2.4	2.3	2.5	2.4
I_{As}	35173	10535	41462	9465
FWHM (eV)	2.6	2.5	2.6	2.5
Observed [As]/[Ga]	1.185	1.185	0.970	0.934

Table 4.2: XPS analysis of GaAs epitaxial surfaces. The [As]/[Ga] ratio is obtained by use of the atomic sensitivity factors for $3d$ peak areas.

monolayer is relatively dense As.

After XPS measurements, samples were transferred to the electron-beam evaporation (EBE) chamber for deposition of Ga_2O_3. Section 3.2 describes the equipment and general procedure used. The sources for evaporation were commercially obtained monolithic Ga_2O_3 sintered lumps of purity 99.995 % (metals basis). The electron beam was observed to bore conical holes with smooth edges into the lumps during evporation as opposed to melting the source. A quartz crystal monitor indicated deposition rates of 0.1-0.2 Å/s.

The substrate temperature was 300°C for all depositions. This is believed to be below the temperature at which arsenic desorbs from the GaAs surface (although arsenic loss was later measured by XPS in Sec. 4.3.2) and sufficiently hot that adatom lateral mobility on the surface was very high. We believe this measured loss to be the result of displacement by oxygen atoms.

After evaporation, samples were returned to the XPS chamber for further analysis. After this was completed, the samples were returned to the EBE system again for the deposition of metal capping layers: Gold for Sample I and nickel for Sample II. The capping evaporations were performed at room temperature and no reaction is expected.

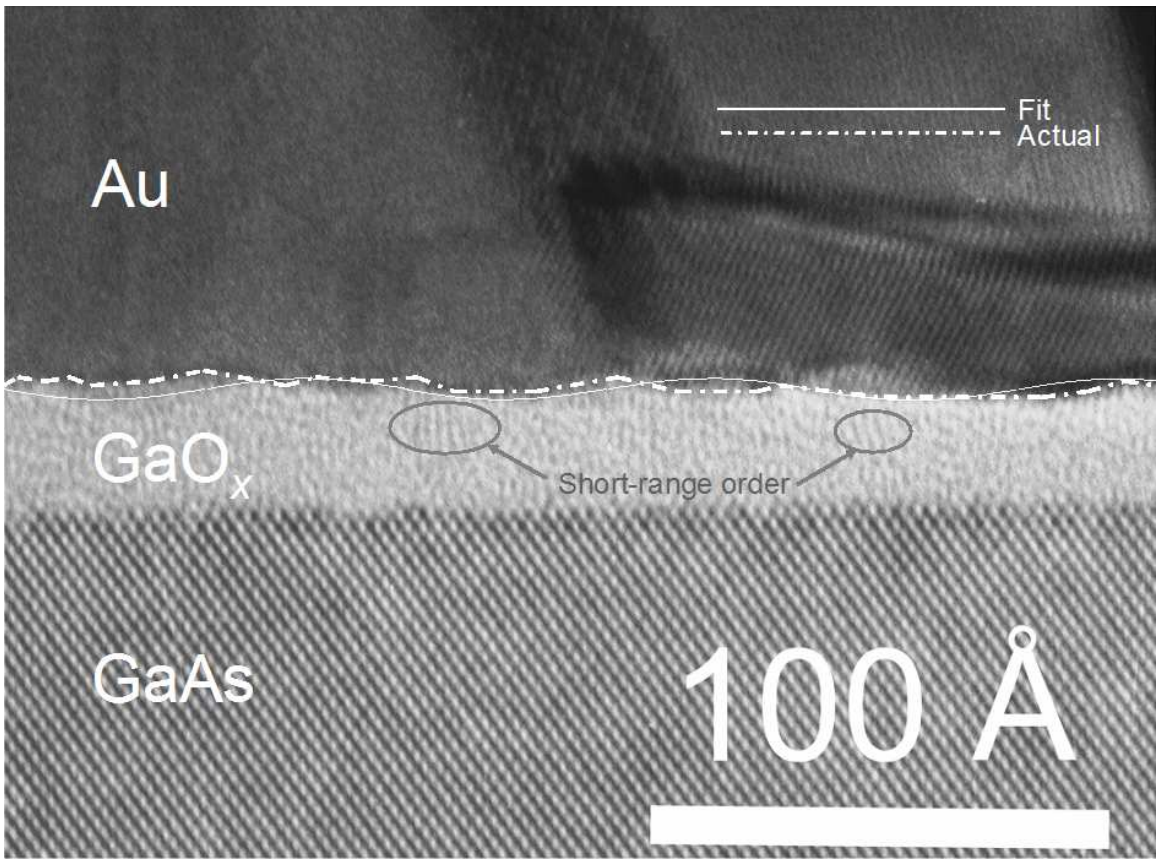

Figure 4.1: Electromicrograph of Ga_2O_3 ultrathin film (Sample I) with Au cap.

4.3 Characterization of Ultrathin Layers

4.3.1 Interfacial Analysis by Transmission Electron Microscopy

The ultrathin films were measured by transmission electron microscopy (TEM) in cooperation with the Caltech Materials Science TEM Facility. A Philips EM430 TEM was used at a filament bias of 300 kV. The samples were prepared by a standard polishing, dimpling, and ion-milling procedure and viewed in cross section ("XTEM").

Both ultrathin films are clearly amorphous. This is typical of oxides grown by MBE or EBE without additional oxygen input [4] and in agreement with the findings of Hong *et al.* [5].

Points along the metal/oxide interfaces were plotted by hand from these images

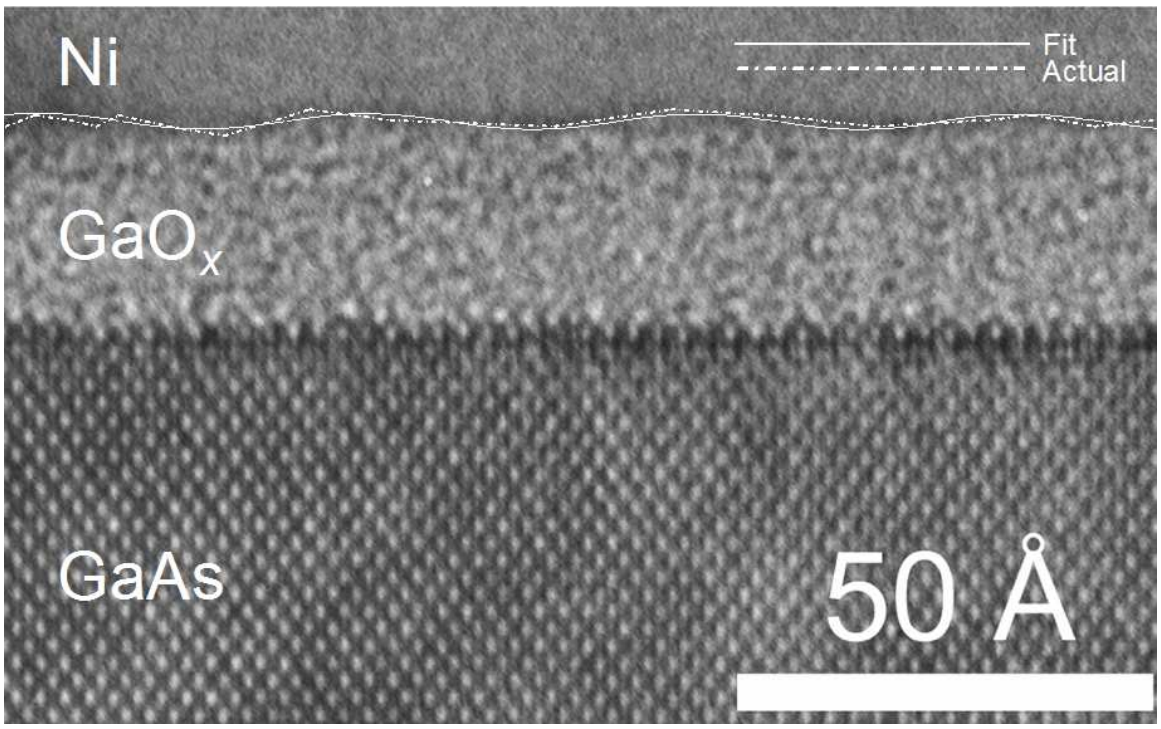

Figure 4.2: Electromicrograph of Ga_2O_3 ultrathin film (Sample II) with Ni cap.

and fit to a sinusoidal roughness model. This yielded roughness wavelengths of 66 Å (Sample I) and 66 Å (Sample II) and rms roughness 1 Å. The roughness of the metal/oxide interface is of interest because of the phenomenon of Néel "orange-peel" coupling for magnetic contacts. Protrusions in the metal film can act as magnetic poles and have an detrimental impact on tunneling properties. Conversely, the coupling can be used to measure the roughness. Using such a measurement Schrag *et al.* measured an rms roughness of 7.3 Å and a wavelength of 94 Å for ultrathin alumina films deposited by sputtering [6].

Long-range order does not appear to manifest in these films, but some short-range ordering seems evident. This likely arises from the four- and six-oxygen complexes which are present in the bulk β-Ga_2O_3 structure (Herman-Mauguin space group $C2/m$). Sample I appears to have more short-range ordering than Sample II, possibly due to the larger oxygen content (see Table 4.4).

4.3.2 X-ray Photoelectron Spectroscopy

Chemical state identification in the Ga-As-O system has been the subject of intense study and different reports have emerged. The reference used for this work is that of Hollinger *et al.* [7]. Generally speaking the preferred transitions for chemical study of this system are the As and Ga 3*d* doublets since these are closest to the Fermi level and thus show the most shift upon bonding.

Analysis of these peaks served two purposes. The first was a measurement of the film thickness, and the second was determination of the stoichiometry of each film.

Thickness determination of thin films by XPS may be accomplished by a technique known as angle-resolved XPS. The essence of the technique is to vary the takeoff angle (see Fig. 2.5) and measure the relative intensity of a substrate peak as a function of this angle. This requires the identification of substrate peaks as well as determination of the electron inelastic mean free path. A widely accepted method of estimating the electron inelastic mean free path (IMFP) is given by Tanuma, Powell, and Penn [8].

The first step in this process is to calculate the free-electron plasmon energy:

$$E_p = (28.8\text{ eV})\sqrt{\frac{N_v \rho}{\mathcal{M}_{\text{tot}}}} \tag{4.1}$$

where N_v is the total number of outer-shell electrons (*i.e.*, the number of electrons from each atom in excess of its noble gas configuration) , ρ is the bulk density in g cm^{-3}, and $\mathcal{M}_{\text{tot}}$ is the total molecular or atomic weight of the material. In the case of Ga_2O_3, $N_v = 44$ (six from each oxygen and eight from each gallium), $\rho = 6.44$ g cm^{-3}, and $\mathcal{M}_{\text{tot}} = 187.4$ g mol^{-1}.

The parameters β and γ are computed next.

$$\gamma = 0.151\rho^{-0.49} \tag{4.2}$$

$$\beta = -0.0252 + \frac{1.05}{\sqrt{E_p^2 + E_g^2}} + 8.10 \tag{4.3}$$

with E_g representing the electronic bandgap in eV. For Ga_2O_3 this is 4.84 eV [9]. Finally the IMFP is given by

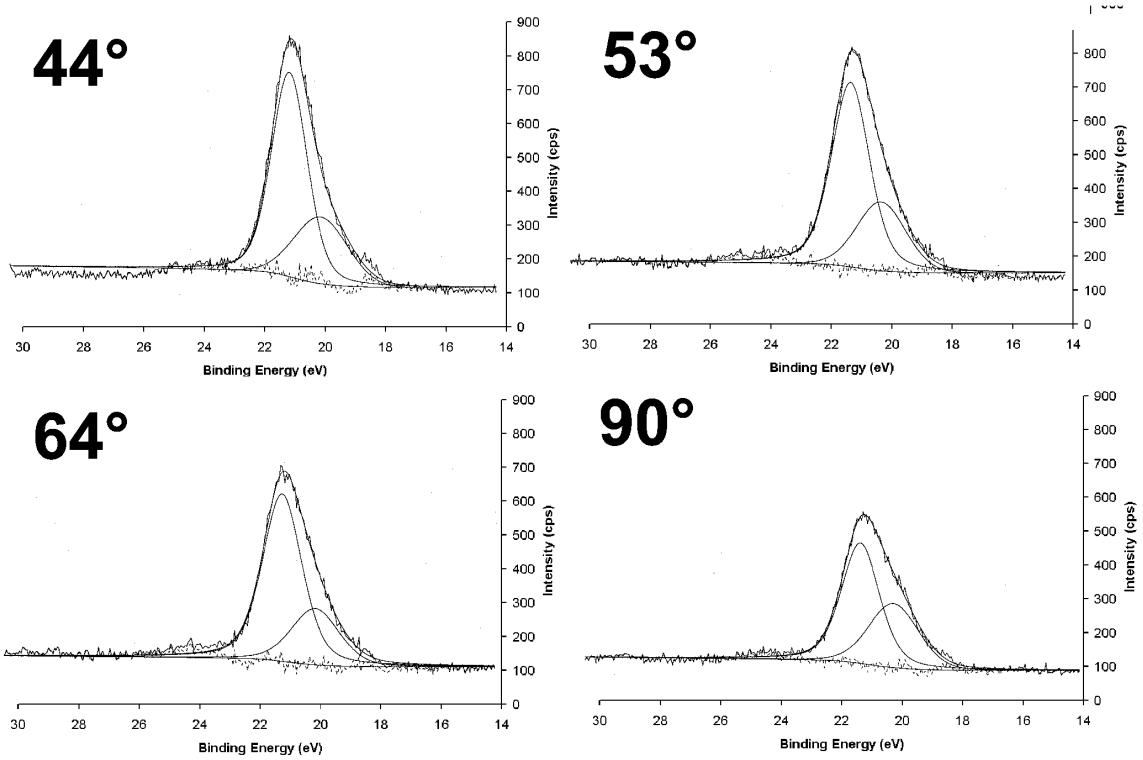

Figure 4.4: Deconvolution of Ga 3d peaks of Sample II for angle-resolved XPS. The angle in each panel denotes the takeoff angle. Doublets are not resolved. Rightmost peaks originate from Ga-As bond (substrate); leftmost peaks originate from Ga-O bonds (film).

$$\Lambda = \frac{T_{sp}}{E_p^2 \beta \ln(\gamma T_{sp})} \text{ Å} \tag{4.4}$$

T_{sp} is the electron kinetic energy; see Eq. 2.3. In our system only the Mg Kα x-ray source may be used for angle-resolved measurements since at high takeoff angles the sample stage obscures the monochromated Al Kα x-ray source. Thus $T_{sp} \simeq 1230$ eV, which is equal to $h\nu$ of Mg Kα x-rays minus the binding energy of the peak of interest (Ga 3d, 20 eV). For this energy, Eq. 4.4 gives $\Lambda = 24.2$ Å.

The deconvolutions of the Ga 3d peaks is shown in Fig. 4.4. Shirley background subtraction was performed, but no noise reduction was applied. Table 4.3 summarizes the result of fitting the angle-resolved data for Sample II.

The relative intensity data was fit to the linear attenuation equation

Takeoff angle	$Ga_{Ga_2O_3}$ Area (arb.)	$Ga_{Ga_2O_3}$ FWHM (eV)	Ga_{GaAs} Area (arb.)	Ga_{GaAs} FWHM (eV)	χ^2	$\frac{I_{Ga_{GaAs}}}{I_{Ga_{Ga_2O_3}}}$
44°	1009	1.55	317	2.02	1.170	0.31417
53°	923	1.53	291	1.96	1.362	0.31528
64°	839	1.61	312	1.93	1.371	0.37187
90°	714	1.51	322	1.96	1.487	0.45098

Table 4.3: Summary of data analysis of peaks shown in Fig. 4.4. Subscripts indicate which compound is the source of the associated peak.

	I		II	
Transition	Mg Kα	Al Kα	Mg Kα	Al Kα
$Ga_{Ga_2O_3}$ 3d	61298	10988	64193	9819
Ga_{GaAs} 3d	34431	8533	33724	6807
As 3d	5316	1967	4052	988
O 1s	90153	16367	87321	13570
$\frac{2I_O}{I_{Ga_{Ga_2O_3}}}$	2.9415	2.9791	2.7206	2.7639
$\frac{I_{As}}{I_{Ga_{GaAs}}}$	0.1544	0.2305	0.1201	0.1451

Table 4.4: Determination of stoichiometry of ultrathin gallium oxide films.

$$I(\theta) = I_0 \exp\left(-\frac{d}{\Lambda \sin\theta}\right) \tag{4.5}$$

I_0 is the intensity of the signal of the chosen substrate peak at the interface, determined by the fit; θ is the takeoff angle; d is the thickness. In this case the thickness was found to be 19.6 Å with $R^2 = 0.807$. Broader scans were performed to obtain As 3d areas as well for the stoichiometry determination. The results are given in Table 4.4

We see that the arsenic-rich surface is closest to Ga_2O_3 in composition. It is also noted that the amount of As measured by XPS is well below that needed for stoichiometric GaAs.

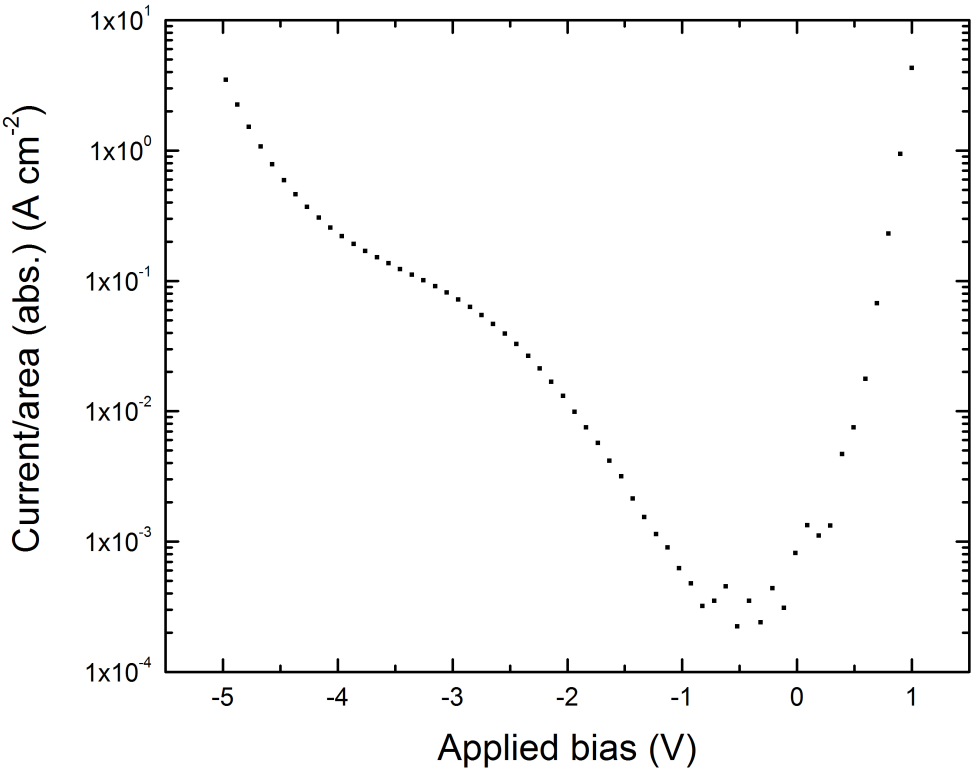

Figure 4.5: $I - V$ characteristics of typical Au/Ni/GaO_x/p-GaAs diode. Breakdown occurs at an applied bias of $\sim$ -4 V.

4.3.3 Electrical Characterization of MIS Diodes

To evaluate the electrical properties of these films, diodes were fabricated using contact lithography to define mesas, DC sputtering to add Au contacts, and a nitric acid etch to isolate devices. Current-voltage relationships were measured with an Alessi REL-4100A probe station and a Hewlett-Packard 4156A semiconductor parameter analyzer. Figure 4.5 shows a typical device. Breakdown voltage was -4 to -5 V. Leakage is obviously a concern for MIS structures with ultrathin insulators and, in this case, the diode (from Sample II) has a substantial oxygen deficiency. It is very likely paths of metallic gallium exist in the ultrathin layer. Negative differential resistance, a hallmark of tunneling, was not observed for any device.

The electroluminescence of a diode was measured with the same apparatus used to measure spin-polarized injection from scanning-tunneling microscope probes [10] at a reverse bias of 1.1 V in the applied field of a permanent magnet ($\sim$ 500 Oe). While some light was observed, the signal was faint and had no circular polarization to indicate spin injection. The magnet was not adequate to orient the magnetic moment of the nickel contact out-of-plane.

4.4 Rutherford Backscattering Spectroscopy of Gadolinium Gallium Garnet Source

Some EBE depositions were performed from gadolinium gallium garnet (GGG, $Gd_3Ga_5O_{12}$), the source material used by Hong *et al.* [5]. Monolithic sources were used of very high purity and no oxygen was introduced during deposition. It was noted that the source changed color from purple to white during evaporation. This generated concern about the reproducibility of such depositions. The source was removed from vacuum and submitted to CEA for RBS analysis as detailed in Sec. 3.4.2.

By fitting the RBS data in Fig. 4.6 it was determined that the outermost 700 Å of the source had experienced a complete loss of gadolinium and had formed Ga_2O_3. The interior of the source retained the composition $Gd_3Ga_5O_{12}$, however. It is thus possible that such sources have a limited service life.

4.5 Discussion

The origin of the low concentrations of As seen by XPS in the post-oxide spectra is not clear. Surfactant action is one possibility: Oxygen supplants arsenic at the surface, then arsenic "floats" upward as GaO_x is deposited. Once gallium oxide deposition is complete it is reasonable to expect the As to boil off; the vapor pressure of As at 300° is between 0.01 and 0.1 torr [11]. While this sounds plausible, it would appear to contradict the electromicrographs of Figs. 4.1 and 4.2 where the underlying GaAs

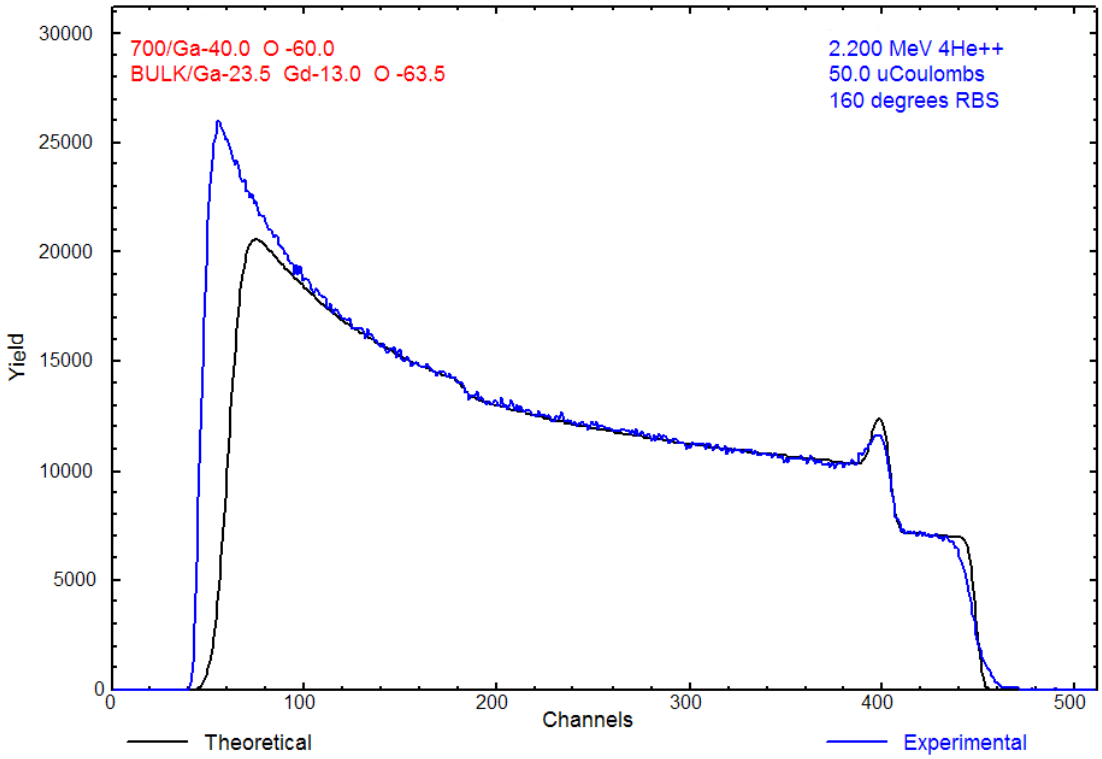

Figure 4.6: Rutherford backscattering spectrum of depleted GGG source.

layers look largely pristine. Surely disordering and recrystallization would accompany the loss of over half the arsenic seen by XPS. Another possibility is that the atomic sensitivity factor for As is miscalibrated, but this is very unlikely given the agreement between the two x-ray sources seen in Table 4.2. Unfortunately this remains an open question.

It can be stated authoritatively that little As-O bonding is taking place at the GaO_x/GaAs interface. The separation between O 1s and As 3d binding energies is measured to be 490.0 eV. Hollinger *et al.* find that in cases of As-O bond formation this separation is $\leq$ 486.5 eV [7]. The standard-state Gibbs free energy of formation $\Delta\overline{G}^0$ of GaAs at 573 K is -1.14 eV, while that of $\frac{1}{2}Ga_2O_3$ is -5.91 eV [12]. This is in accord with the observations of Hong *et al.* [13].

The smoothness of the film was very satisfactory and as such recommends EBE as a technique for the contstruction of magnetic tunnel junctions to overcome Néel coupling issues [6]. It also seems that the As-rich surface yields more highly oxidated films. As long as the films remain amorphous, nearly complete oxidation is desirable to reduce the free metallic gallium which can form conductive shorts in tunneling devices.

Since this work was initially reported [14], Hale *et al.* utilized scanning tunneling microscopy to study the deposition of O_2(g) on (2×4) GaAs surfaces by MBE from a monolithic source and observed the same displacement of arsenic from the surface. By using an aperature to control the relative decomposition of Ga_2O_3(s) from an effusion cell, they were able to create pinned or unpinned Fermi surfaces on GaAs. Interest in deposition of ultrathin gallium oxide films is ongoing due to photonic and other applications [15, 16].

It remains uncertain if truly efficient spin injection through such an oxide tunnel barrier may be realized. To date the best known literature result for spin injection in an FM/I/SC structure at room temperature is 12% [17] using the oblique Hanle effect for electroluminescence measurement of a permendur/AlO_x/(Al,Ga)As configuration. Many improvements must be made to the injection scheme before useful spin transistors using mobile charges may be deployed for applications.

Bibliography

[1] J. E. Stannard, T. A. Kennedy, and B. D. McCombe, B. Am. Phys. Soc. **23**, 275 (1976).

[2] T. S. Lay, M. Hong, J. Kwo, J. P. Mannaerts, W. H. Hung, and D. J. Huang, Solid State Electron. **45**, 1679 (2001).

[3] Z. Li, C. de Groot, and J. H. Moodera, Appl. Phys. Lett. **77**, 686 (1995).

[4] S. A. Chambers, Surf. Sci. Rep. **39**, 105 (2000).

[5] M. Hong, M. Passlack, J. P. Mannaerts, J. Ktow, S. N. G. Chu, N. Moriya, S. Y. Hou, and V. J. Fratello, J. Vac. Sci. Technol. B **14**, 2297 (1996).

[6] B. D. Schrag, A. Anguelouch, G. Xiao, P. Trouilloud, Y. Lu, W. J. Gallagher, and S. S. P. Parkin, J. Appl. Phys. **87**, 4682 (2000).

[7] G. Hollinger, R. Skheyta-Kabbani, and M. Gendry, Phys. Rev. B. **49**, 11159 (1994).

[8] S. Tanuma, C. J. Powell, and D. R. Penn, Surf. Interface Anal. **11**, 577 (1988).

[9] L. Binet, D. Gourier, and C. Minot, J. Solid State Chem. **113**, 420 (1994).

[10] C. J. Hill, Ph.D. thesis, California Institute of Technology, 2001.

[11] http://www.veeco.com/learning/learning_vaporelements.asp, Veeco Instruments, May 4, 2004.

[12] *CRC Handbook of Chemistry and Physics*, edited by D. R. Lide (CRC Press LLC, Boca Raton, Fla., 1994).

[13] M. Hong, A. R. Kortan, J. Kwo, J. P. Mannaerts, J. J. Krajewski, Z. H. Lu, K. C. Hsieh, and K. Y. Cheng, J. Vac. Sci. Technol. B **18**, 1688 (2000).

[14] N. C. Oldham, C. J. Hill, C. M. Garland, and T. C. McGill, J. Vac. Sci. Technol. A **20**, 809 (2002).

[15] M. F. Al-Kuhaili, S. M. A. Durrani, and E. E. Khawaja, Appl. Phys. Lett. **8**, 4533 (2003).

[16] J. J. Robbins, C. Fry, and C. A. Wolden, J. Cryst. Growth **263**, 283 (2004).

[17] P. Van Dorpe, V. F. Motsnyi, M. Nijboer, E. Goovaerts, V. I. Safarov, J. Das, W. Van Roy, G. Borghs, and J. De Boeck, Jpn. J. Appl. Phys. 2 **42**, L502 (2003).

Appendix A

Regression Analysis of Activity Data in the Co-Cr System

The definition of activity arises from the formalism for the free energy of mixtures. The change of the free energy per mole of a binary system upon mixing elements A and B is

$$\Delta\overline{G}^{\text{mix}} = x_{\text{A}}\Delta\overline{G}_{\text{A}}^{\text{mix}} + x_{\text{B}}\Delta\overline{G}_{\text{B}}^{\text{mix}}$$

The activity is defined as $a_{\text{A}} = \exp(\Delta\overline{G}_{\text{A}}^{\text{mix}}/RT)$, where R is the ideal gas constant and T the system temperature. Since for an ideal solution

$$\Delta\overline{G}_{\text{A}}^{\text{mix,ideal}} = -T\Delta\overline{S}_{\text{A}}^{\text{mix}} \tag{A.1}$$

$$\Delta\overline{S}_{\text{A}}^{\text{mix}} = -R\ln x_{\text{A}} \tag{A.2}$$

The activity coefficient $\gamma_{\text{A}} = a_{\text{A}}/x_{\text{A}}$ is introduced to quantify the nonideality of the mixture. It follows that the enthalpy of mixing $\overline{H}_{\text{A}}^{\text{mix}} = RT\ln\gamma_{\text{A}}$ since $G \equiv H - TS$. An activity coefficient of unity implies an ideal solution.

The model developed in Sec. 3.4.1 requires a means to compute the activity coefficients of Co and Cr at a given temperature and composition. The approach used here is to obtain the activity coefficient data over the anticipated parameter range and apply regression analysis to obtain simple continuous functions useful in root-finding

programs.

The phase diagram in Fig. A.1 was obtained from the Kaufman binary alloys database in the THERMO-CALC CLASSIC version N software package. The diagram shows the eutectoid reaction believed to occur $\sim 200°$C where $\sigma \leftrightarrow (\epsilon\text{Co}) + (\alpha\text{Cr})$ due to the effect of ferromagnetism on the mixture.

Activity coefficients were calculated using THERMO-CALC for the parameter ranges 1300 K $\leq T \leq$ 1430 K and $0 \leq x_{\text{Cr}} \leq 0.3$ which were initially believed to be the relevant parameter range. Plots were generated for 1300 K, 1330 K, 1360 K, 1380 K, and 1430 K. These plots were carefully digitized (at least twenty points per plot) in order to create numeric data.

The equation used to fit the activity coefficient data for element i was chosen to have the following form since at a given temperature the activity coefficient appear parabolic:

$$\gamma_i(T, x_{\text{Cr}}) = (A_{i,1} + A_{i,2}x_{\text{Cr}} + A_{i,3}x_{\text{Cr}}^2)(A_{i,4} + A_{i,5}T + A_{i,6}T^2 + A_{i,7}T^3) \qquad \text{(A.3)}$$

Fits were determined with ORIGINPRO and are given in Table A.1.

	γ_{Co}	γ_{Cr}
A_1	3.9776×10^{-8}	3.6334×10^{-8}
A_2	1.046×10^{-8}	-1.0211×10^{-8}
A_3	-1.8676×10^{-8}	2.2717×10^{-8}
A_4	-3.2443×10^{8}	-2.7249×10^{8}
A_5	744251	718626
A_6	-528.23	-549.79
A_7	0.12495	0.13749
R^2	0.92311	0.99396

Table A.1: Parameters for regression fit of activity coefficient data of Co and Cr to Eq. A.3.

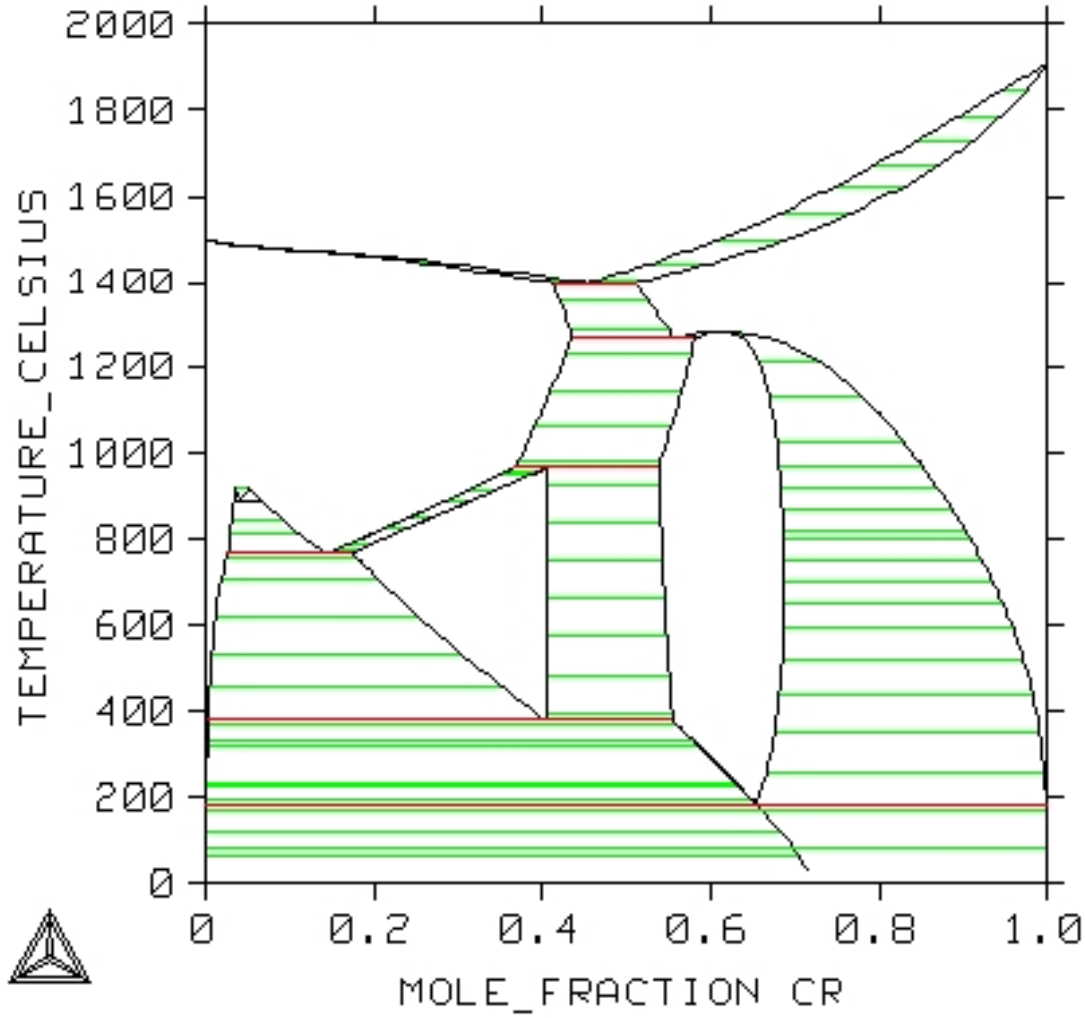

Figure A.1: Phase diagram of Co-Cr computed by THERMO-CALC. See Ref. [1] for phase labels.

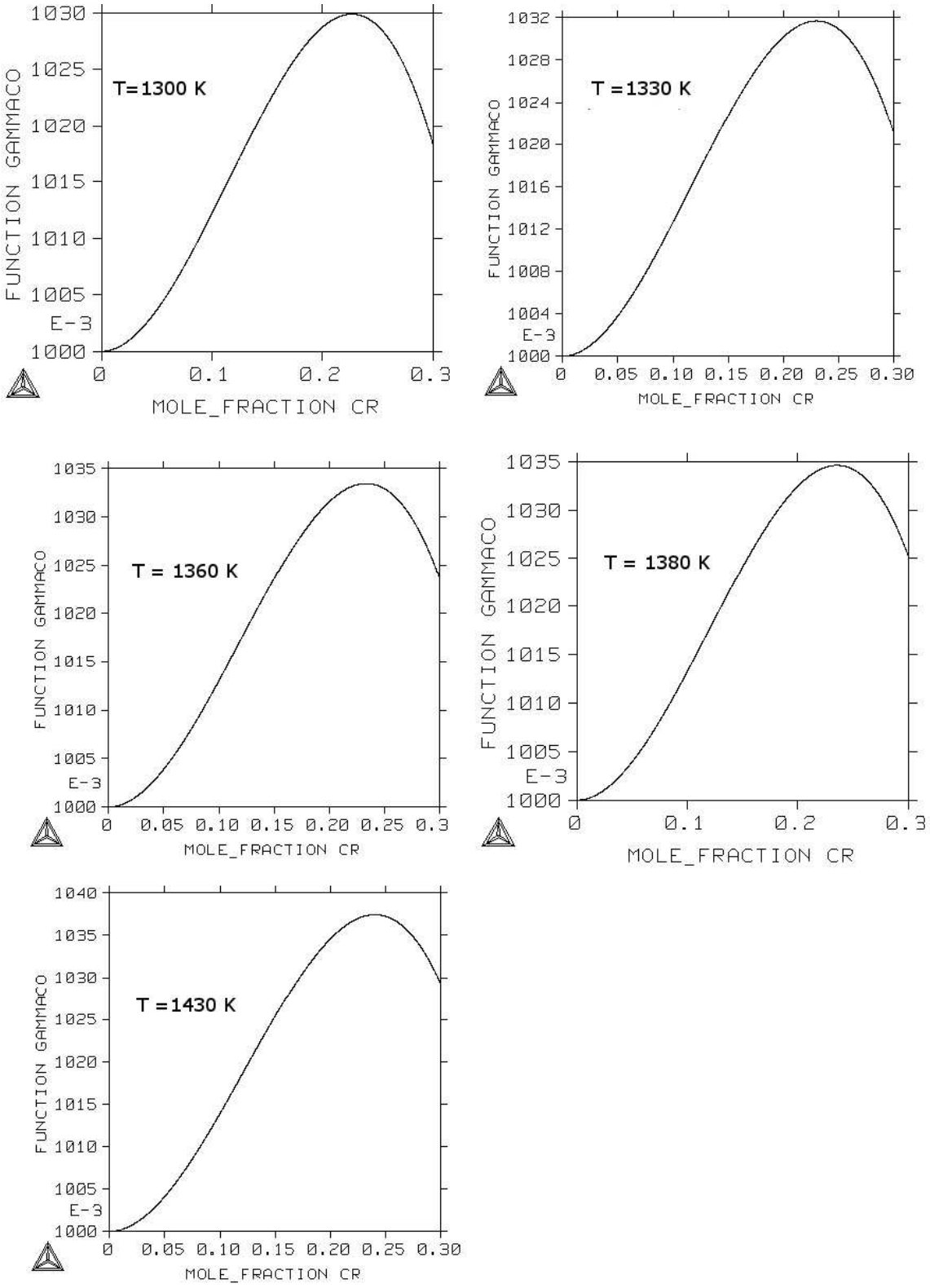

Figure A.2: Activity coefficient of Co in mixture with Cr

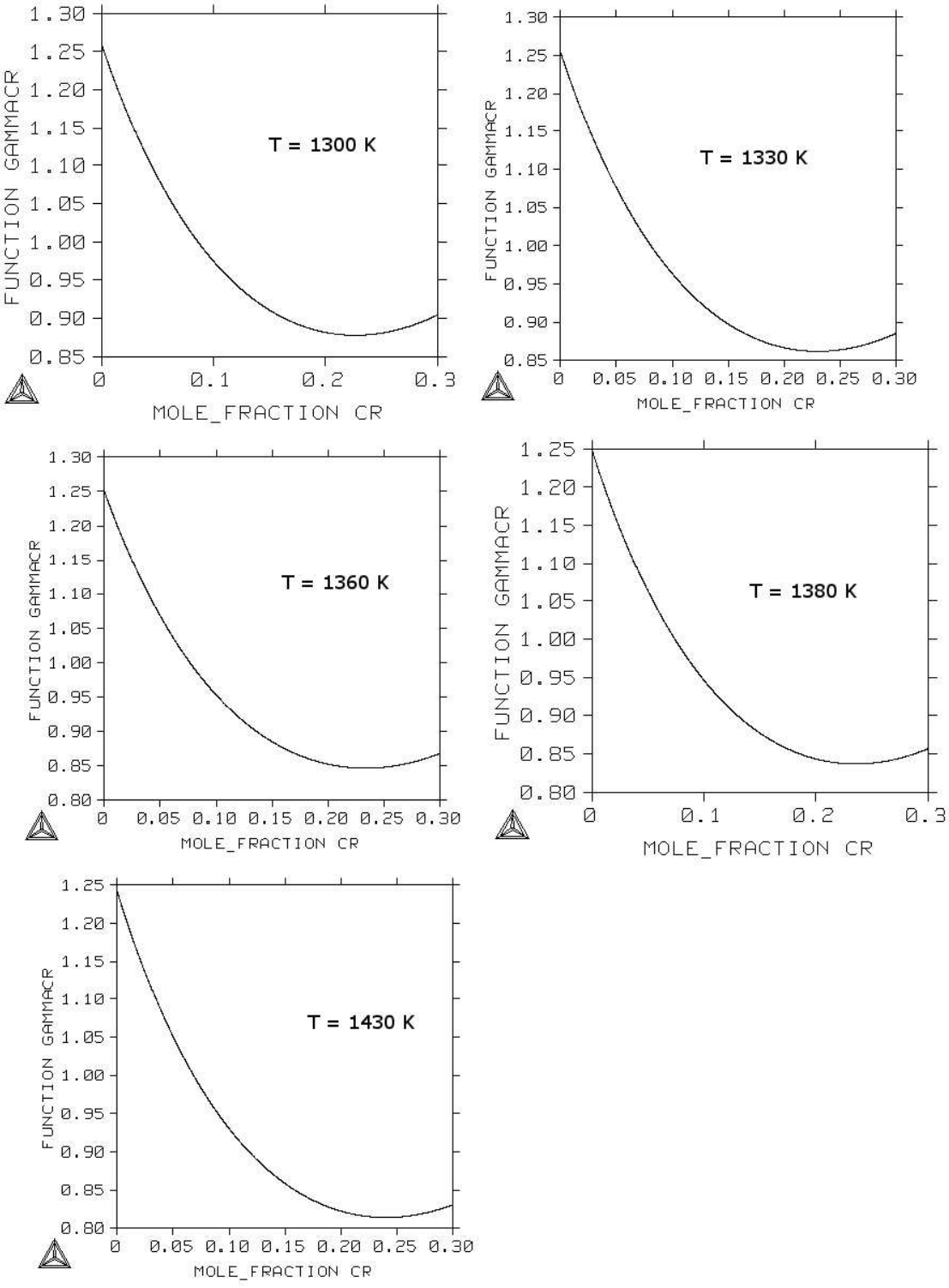

Figure A.3: Activity coefficient of Cr in mixture with Co

Bibliography

[1] *Binary Phase Alloy Diagrams*, edited by T. B. Massalski (ASM International, Materials Park, Ohio, 1990), Vol. 2, p. 1180.